CHEMICAL REVIEWS

pubs.acs.org/CR

Review

Theory of Anisotropic Metal Nanostructures

Kristen A. Fichthorn

Cite This: https://doi.org/10.1021/acs.chemrev.2c00831

Read Online

ACCESS | Metrics & More | Article Recommendations

ABSTRACT: A significant challenge in the development of functional materials is understanding the growth and transformations of anisotropic colloidal metal nanocrystals. Theory and simulations can aid in the development and understanding of anisotropic nanocrystal syntheses. The focus of this review is on how results from first-principles calculations and classical techniques, such as Monte Carlo and molecular dynamics simulations, have been integrated into multiscale theoretical predictions useful in understanding shape-selective nanocrystal syntheses. Also, examples are discussed in which machine learning has been useful in this field. There are many areas at the frontier in condensed matter theory and simulation that are or could be beneficial in this area and these prospects for future progress are discussed.

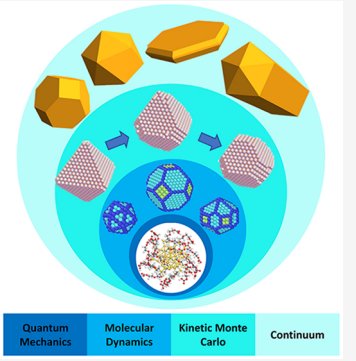

CONTENTS

1. INTRODUCTION

A significant challenge in the development of functional materials is understanding the growth and transformations of colloidal metal nanocrystals. From a practical perspective, a knowledge of how to selectively synthesize metal nanocrystal with selective sizes and shapes would benefit numerous applications in energy, electronics, photonics, and health. For example, catalyst nanocrystal synthesis science is playing an increasingly prominent role in electrocatalysis for fuel-cell applications[1−16] and the sustainable production of fuels and chemicals.[17−20] The role of nanocrystal shape has been emphasized in heterogeneous catalysis,[10,21−30] to meet the need for increasing efficiency and in photocatalysis for the production of solar fuels.[15,31−42]

The benefits of nanocatalysts with specific sizes and shapes have been demonstrated in many studies.[16,17,27−31,42−53] For example, Choi et al. conducted a systematic study of formic acid oxidation on a variety of Pd nanocrystal electrocatalysts with different shapes.[43] The left panel of Figure 1 shows transmission electron microscope (TEM) images of the various shapes they studied, which were cubes, right bipyramids, octahedra, tetrahedra, decahedra (Dh), and icosahedra (Ih), all of approximately of the same size. As shown in the right panel of Figure 1, they found that Pd nanocrystals expressing {100} facets, such as cubes and right bipyramids, had higher activities than those enclosed by {111} facets, such as tetrahedra and octahedra. Nanocrystals with twin planes: right bipyramids, Dh, and Ih, had higher activities than single crystals with the same facets.

Ma and colleagues studied the effect of Pt nanocrystal size on the efficiency of the photocatalytic nonoxidative conversion of methane to ethane.[42] They studied Pt particle sizes ranging

Special Issue: Anisotropic Nanomaterials

Received: November 26, 2022

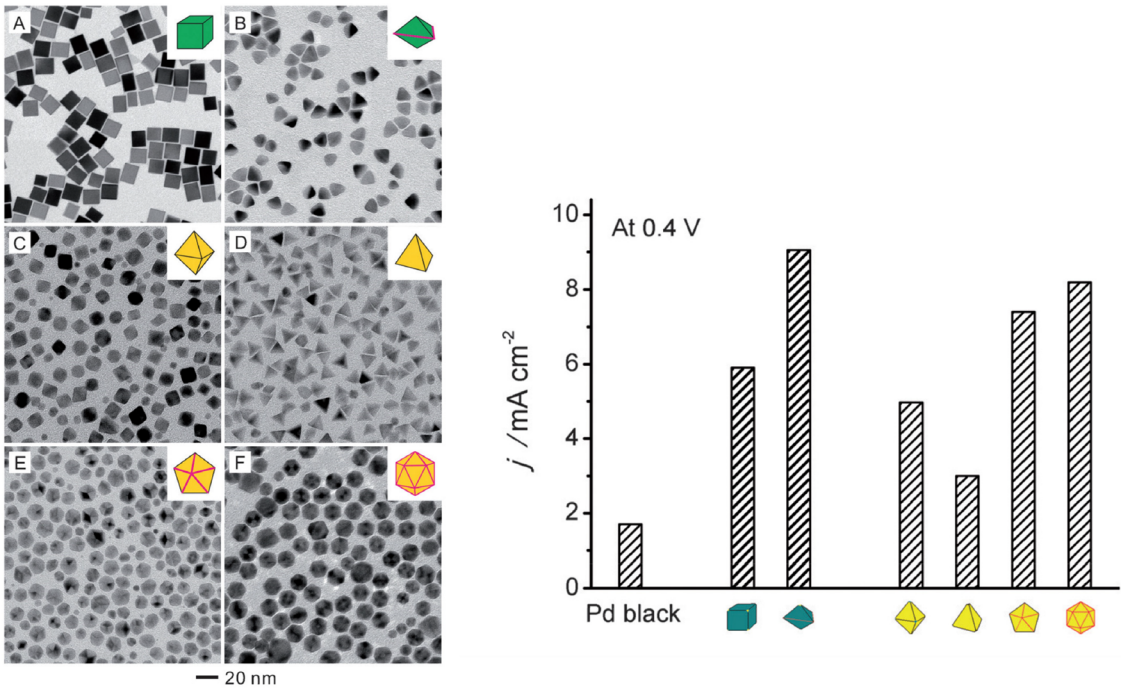

Figure 1. (left) TEM images of various types of Pd nanocrystals used in the study of Choi et al.:[43] (A) cubes, (B) right bipyramids, (C) octahedra, (D) tetrahedra, (E) decahedra, and (F) icosahedra. Nanocrystals shown in green possess {100} facets, and those shown in yellow possess {111} facets. Twin planes are shown with red lines. The scale bar is 20 nm. (right) Comparison of the specific activities for formic acid oxidation for the various shapes shown in the left panel, along with commercial Pd black, at a potential of 0.4 V. Reproduced from ref 43. Copyright 2015 Wiley-VCH.

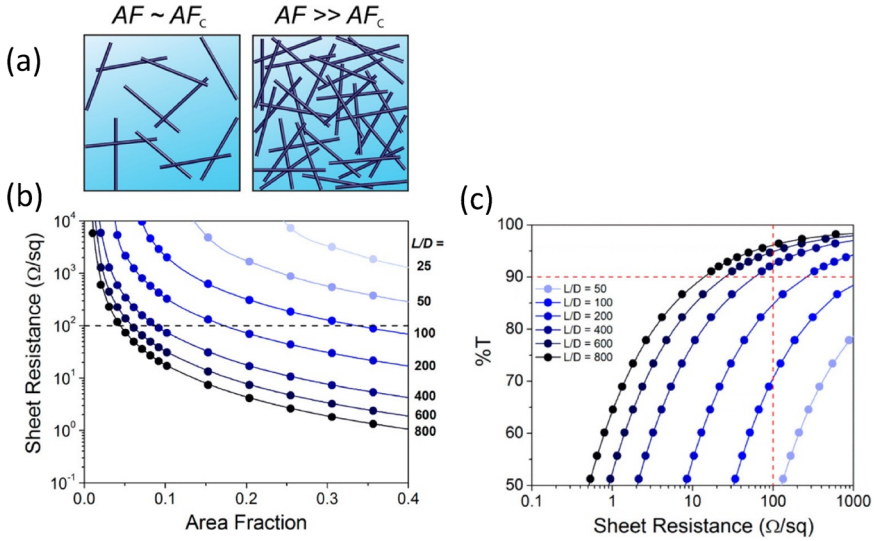

Figure 2. (a) Illustration of two percolated nanowire networks with area fractions (AF) near to or exceeding the critical area fraction for percolation (AF_c). (b) Simulated sheet resistance as a function of nanowire area fraction for various nanowire aspect ratios (L/D). The dashed line indicates the maximum viable sheet resistance for high performance applications. (c) Calculated transmittance ($\%T$) vs sheet resistance for Ag nanowire films. Dashed lines indicate the maximum sheet resistance and minimum transmittance for high performance applications. Reproduced with permission from ref 90. Copyright 2013 American Chemical Society.

from 1.5 to 2.7 nm on a Ga_2O_3 support and observed a maximum in the CH_4 conversion rate as a function of particle size. Xiao et al. studied the copper-catalyzed deoxygenation reaction of aromatic epoxides catalyzed by various Cu nanomaterials.[50] They showed that Cu cubes and wires (with mostly {100} facets) gave olefin products with a different cis/trans selectivity than plates with mostly {111} facets. These examples demonstrate how nanocrystals with different shapes and sizes can exhibit distinctly different activities and selectivities as catalysts.

Metal nanocrystals figure prominently in solar-cell technologies, for example, as nanometallic plasmonic structures to enhance the light absorption and efficiency of photovoltaics.[54−64] There are numerous applications for nanowire-based transparent conducting films,[65−72] including wearable triboelectric generators[73−77] heaters,[78−81] electromagnetic

https://doi.org/10.1021/acs.chemrev.2c00831
Chem. Rev. XXXX, XXX, XXX−XXX

interference shielding,[82−85] wearable health monitoring devices,[67] electronic skin,[86] wearable electronics,[87] electrochromic windows,[88] and touch screens.[89]

Mutiso and colleagues have a nice discussion of how the lengths (L), diameters (D), and area fractions (AF) of metal nanowires affect the sheet resistance and optical transmittance of nanowire-based transparent conducting films.[90] For nanowire thin films to exhibit significant conductivity, the nanowire area fraction needs to exceed the percolation threshold AF_c, at which nanowire overlaps begin to occur, as shown in Figure 2a. Mutiso et al. calculated the sheet resistance as a function of the nanowire area fraction for thin films containing nanowires of various aspect ratios (L/D), assuming all the resistance occurred in nanowire−nanowire contacts, as shown in Figure 2b. To be considered viable for high performance applications, nanowire thin films need to have a sheet resistance of less than 100 Ω/sq, as indicated by the dashed line in Figure 2b. We see that nanowires with higher aspect ratios fulfill this criterion to a greater extent than those with low aspect ratios. Figure 2c depicts the calculated transmittance (%T) as a function of sheet resistance for nanowires of various aspect ratios. The dashed lines indicate criteria for high performance applications: sheet resistance of less than 100 Ω/sq and transmittance of greater than 90%. Only nanowires with the highest aspect ratios can meet these criteria. They also discussed that transmittance decreases with increasing area fraction. As shown in Figure 2b, only nanowires with the highest aspect ratios meet the sheet resistance criteria at low area fractions, consistent with Figure 2c. These results are fully consistent with experiment.

Metal nanocrystals are also featured in emerging applications targeting energy efficiency, such as photothermic desalination based on plasmonic nanocrystals,[91−97] energy storage devices,[98−100] electrochromic smart windows,[88,101,102] and life-inspired nanosystems.[103,104] For these and many other applications, the science of shape-selective nanocrystal synthesis has been advancing at an increasingly rapid pace, with numerous recent reports on the synthesis of various beneficial nanocrystal morphologies.[105−118] Such studies indicate that nanocrystal synthesis science will play an important role in achieving a sustainable energy future, as well as in enhancing our quality of life.

Despite ample demonstrations that it can be highly beneficial to tune nanocrystal morphologies for specific applications and despite the tremendous strides made in nanocrystal synthesis science, it is still difficult to achieve high, selective yields in most synthesis protocols. Many fundamental aspects of these complex syntheses remain poorly understood. Theory and simulations can aid in the development and understanding of anisotropic nanocrystal syntheses, and the goal of this review is to discuss how theory and simulations have been and can be beneficial in this area.

At the outset, it is beneficial to define the scope and format of this review. Anisotropic nanocrystals are defined as crystals with nonspherical shapes. Such shapes could have uniform aspect ratios, such as truncated octahedra (TO), Ih, and Dh, the so-called zero-dimensional nanomaterials. They could possess one-dimensional shapes, such as nanowires, or two-dimensional shapes, such as nanoplates. The focus of this review is on monometallic nanocrystals with sizes of one nanometer or larger. I note there is a large body of work focusing on subnanometer metal particles, as discussed in the recent review by Baletto[119] and in a recent perspective.[120] I also omit a truly fascinating body of work devoted to understanding the shapes and composition profiles of multimetallic nanocrystals. The focus of this review, on multiscale atomistic techniques based on quantum mechanics, distinguishes it from prior reviews of the theory of nanocrystal growth and shapes.[121] I omit the discussion of aggregative particle growth mechanisms and of the shapes of supported metal nanocrystals, as both have been the subjects of recent reviews.[122,123]

In this review, I will discuss selected studies in which theory was used to gain insight into the thermodynamics and kinetics of nanocrystal shapes. As such, this review is not a "deep dive" into the theoretical methods themselves, but more what could be learned from these methods. I will not discuss workhorse methods in quantum mechanics, such as density functional theory (DFT), or in statistical mechanics, such as molecular dynamics (MD), but I will review select techniques that employ these methods, so the reader can appreciate what is involved in these calculations.

It is also helpful to outline the experimental context for this review. I consider a typical solution-phase synthesis, as depicted in Figure 3. Key components in such a synthesis

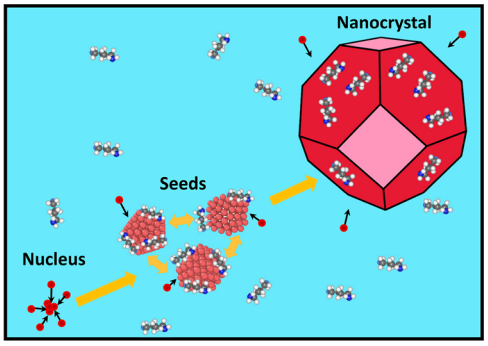

Figure 3. Overview of a typical solution-phase synthesis, which consists of metal salt that is reduced to metal atoms, which aggregate to form nuclei. The nuclei grow to form seeds, which grow and transition among various structures until they reach their final nanocrystal shape.

are solvent, metal salt, capping agents, and other additives.[124] The metal salt dissociates, and the metal ions are reduced, perhaps by solvent, capping agent, or other additives. Metal atoms and ions aggregate to form nuclei, which grow to form seeds. Seeds are intermediate structures along the growth trajectory between subnanometer nuclei and the nanocrystal product.

Seeds play a critical role in nanostructure formation, as the shape of the seed is believed to determine the shape of the nanocrystal product.[124] Figure 4 shows various possible seeds along with their associated nanocrystal morphologies.[125] Single-crystal (fcc) seeds can lead to shapes such as cubes, TO, cuboctahedra (CO), and rods. Seeds containing a single stacking fault have been linked to nanocrystals containing single stacking faults, while multiply twinned seeds, such as Dh and Ih, are believed to lead to nanowires and larger multiply twinned structures. Seeds with multiple, parallel stacking faults or twin planes produce plates.

Evidence from experimental TEM studies indicates that relatively small seeds (<5 nm in diameter) are highly fluxional and can rapidly transition between various structures,[100−102] as shown in Figure 3. The time scale for structural transitions is

https://doi.org/10.1021/acs.chemrev.2c00831
Chem. Rev. XXXX, XXX, XXX−XXX

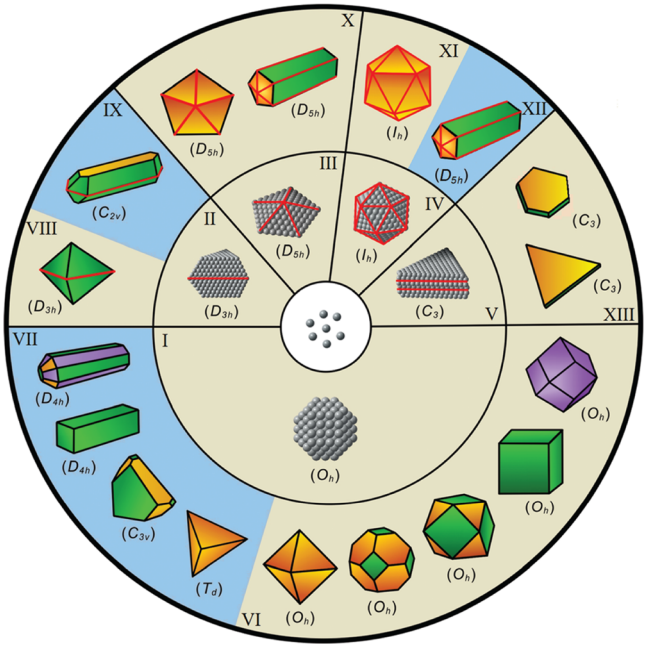

Figure 4. Various possible fcc metal nanocrystals with low-index facets (outer circle) and their associated seeds (middle circle) that evolve from nuclei (inner circle). Red lines indicate twin planes or stacking faults, {111} facets are orange, {100} facets are green, and {110} facets are purple. Used with permission of The Royal Society of Chemistry, from ref 125; permission conveyed through Copyright Clearance Center, Inc.

believed to become increasingly slow as the seed size increases, and structural transitions effectively cease once a critical seed size is reached, possibly resulting in a metastable shape.[103−105] An interesting interplay between structural transitions, deposition/reduction, and possibly etching, which helps to reshape seeds, can lead to a myriad of metastable morphologies.

As implied by the above discussion, the outer circle in Figure 4 indicates final nanocrystals that are believed to grow and likely assume kinetic shapes from the seeds in the middle circle. Various kinetic mechanisms involving capping agents, surface diffusion, deposition, and etching are believed to conspire to produce such nanocrystals. In addition to the low-index nanocrystals in Figure 4, a variety of nanocrystals with high-index facets, such as those depicted in Figure 5, have been synthesized and are believed to arise from a combination of kinetic mechanisms, as discussed by Zhang, Jin, and Xia.[86]

Finally, regarding the experimental picture, although this review is focused on understanding nanocrystal growth in solution, the role of experiments and theory in the vacuum or gas phase is important, so vacuum results will also be discussed. Early insights to the process of metal nanocrystal growth and restructuring came from TEM studies in a vacuum environment.[126,127] Modern studies in vacuum employ aberration-corrected scanning TEM, or ACSTEM, with a high angle annular dark field (HAADF) detector.[128−132] Such studies are valuable for understanding solution-phase metal crystal growth, as HAADF-ACSTEM can probe smaller nanoparticles with higher resolution and less uncertainty than liquid-phase techniques, such as liquid-phase TEM (LPTEM), also known as environmental TEM. The high resolution of ACSTEM is particularly beneficial for efforts to develop accurate theoretical methods to describe the energetics and kinetics of metal nanoparticle systems.

Figure 6 depicts various theoretical techniques applied to understand nanocrystal shapes, the approximate numbers of atoms that can be directly probed with these techniques, and the time scales they address. Nanocrystals below the 2 nm size range can be directly addressed via quantum mechanics. Quantum mechanical techniques are the best suited to describe chemical bonding and the effects of adsorbed species on nanocrystal shape. Since the times that can be probed by quantum techniques, such as *ab initio* molecular dynamics (AIMD), lie in the ps−ns regime, virtually all the direct quantum mechanical studies of nanocrystals rely on structural

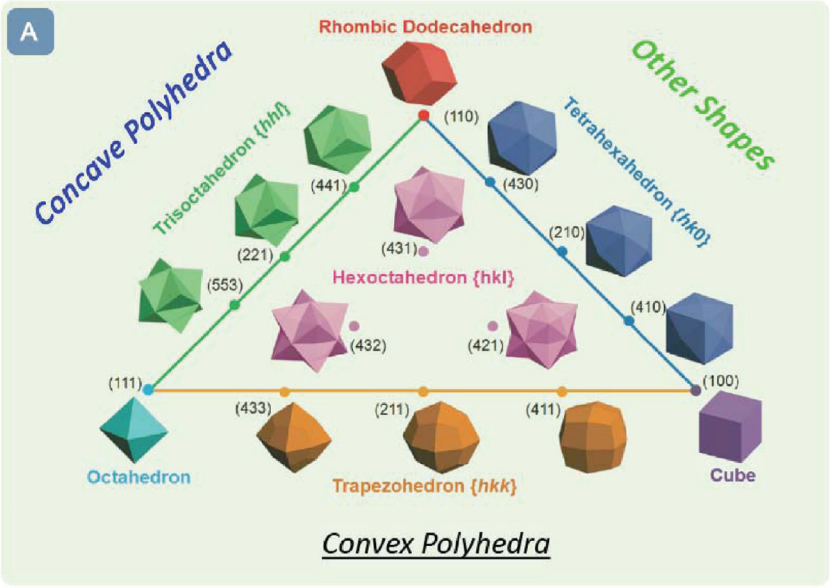

Figure 5. Various high-index nanocrystal shapes enclosed by different types of crystalline facets. Reproduced with permission from ref 106. Copyright 2013 American Chemical Society.

https://doi.org/10.1021/acs.chemrev.2c00831
Chem. Rev. XXXX, XXX, XXX−XXX

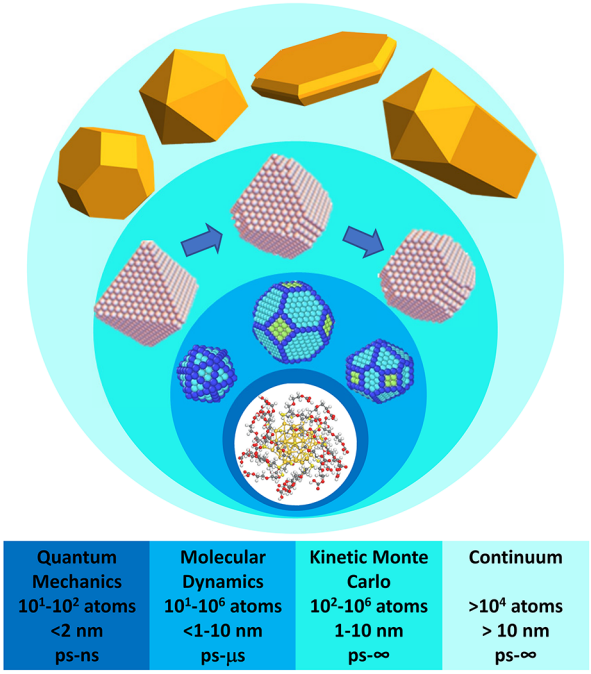

Figure 6. Various theoretical techniques applied to understanding nanocrystal structures and the approximate number of atoms they probe. Quantum calculations can address the smallest length and time scales and are the most accurate means of describing chemical bonding, as shown in the smallest circle. Reproduced with permission from ref 133. Copyright 2019 American Chemical Society. At the next level of resolution is classical MD, which can probe hundreds to millions of atoms at times up to microseconds. kMC simulations can probe large-scale and long-time structural evolution. Reproduced with permission from ref 134. Copyright 2021 American Chemical Society. At the continuum scale, we have Wulff constructions, which address the shapes of the largest nanocrystals.

optimization methods, which describe minimum-energy crystal structures. Quantum methods, such as DFT, inform force field development and allow for classical MD, kinetic Monte Carlo (kMC), and continuum descriptions, all of which can probe significantly larger length and time scales. While it is difficult to accurately probe the influence of adsorbed molecules or a solution environment in quantum calculations, this influence can be included in classical MD simulations, which can probe larger nanocrystals and the effect of a solution environment.

MD simulations can reach microsecond times, which limits the capability of direct MD simulations to simulate nanocrystal kinetics. However, as we will discuss below, various theoretical methods incorporate MD simulations to reach longer times than direct MD. In kMC, we obtain the solution to a set of rate equations, whose rates can be obtained from quantum mechanical calculations, MD, experiment, or even the hypothesis of an investigator. Lattice-based kMC simulations can reach macroscopic times and, depending on how the rate constants were obtained, they can be as accurate as *ab initio* MD, if such a simulation could reach long times. At the continuum level, we can estimate Wulff shapes, which address the largest nanocrystals. As I will discuss below, such calculations are typically based on quantum mechanics or lower-level calculations. Machine learning has been beneficial to this field in several different ways and a portion of this review will be devoted to such studies.

2. THERMODYNAMICS OF NANOCRYSTAL STRUCTURE

The potential energy E of a cluster as a function of the number of its atoms N is often given the form[135,136]

$$E(N) = A + BN^{1/3} + CN^{2/3} + DN \quad (1)$$

where A is a contribution from vertices, $BN^{1/3}$ arises from the edges, $CN^{2/3}$ is the contribution from the facets, and DN is the bulk contribution. When the system is sufficiently small, all terms are important, although the bulk and surface energy terms become dominant for crystals with sizes greater than ∼1 nm.[136,137] Equation 1 has been used to understand the major structural motifs of fcc metal nanocrystals, shown in Figure 7.

The Ih, shown in Figure 7a, consists of 20 fcc tetrahedral units which meet in twin planes, as shown in the large shape. In the small inset, we see large gaps when 20 regular tetrahedra are packed around a common vertex.[138] To close the gaps, the tetrahedra need to be distorted, which causes strain. The surface of the Ih consists of {111} facets, the lowest-energy facet in fcc metals. Equation 1 has been used to rationalize the preponderance of Ih as the minimum-energy shapes of nanocrystals with small sizes, as the low energy of the {111} facets can compensate for the bulk strain in small nanocrystals.[136]

Two variants of the Dh are shown in Figure 7b,c. As shown for the small inset, the tetrahedral units comprising a Dh are not space filling, and there is a gap of 7.36° for regular tetrahedra.[138] Closure of this gap creates bulk strain in a Dh, although this strain is less than that of the Ih. The Ino Dh, shown in Figure 7b, has a pentagonal shape with ten {111} "end" facets and five {100} "side" facets.[139] By lengthening the {100} side facets of the Ino Dh, we obtain the shape commonly associated with penta-twinned nanorods and nanowires, shown in Figures 4 and 6. The Marks Dh in Figure 7c, is an energetic improvement on the Ino Dh, as it adds {111} "notches" to the {100}−{100} edges, to increase the area of the {111} facets and release some of the strain.[140] Again, eq 1 has been used to understand the progression of minimum-energy nanocrystal shapes from Ih to Dh as the nanocrystal size increases.[136,141]

A common single-crystal structure is the TO, shown in Figure 7d. Again, eq 1 has been used to understand why this (or related structures) is the minimum-energy structure for the largest nanocrystals, as the single-crystal structure has no bulk strain. In single-crystal structures, the shape arises from surface-energy considerations only. As I will discuss below, such single-crystal shapes can be predicted by the Wulff construction.[142]

It is important to mention that the nanocrystals in Figure 7 and related shapes have "magic" sizes, where the number of atoms in the nanocrystal is such that a perfect shape can occur.[143] Magic-sized clusters are often referred to as having filled shells, a notion that comes from building clusters by placing atoms around a central magic unit until a larger cluster emerges with the same shape.[144] Although nanocrystal shapes can be complex and other "new" magic sizes have been identified,[145−147] the shapes in Figure 7 are nonetheless the major structural motifs observed for fcc metal nanocrystals. All of these structures have been observed in solution-phase syntheses.[116,117,148−155]

https://doi.org/10.1021/acs.chemrev.2c00831
Chem. Rev. XXXX, XXX, XXX−XXX

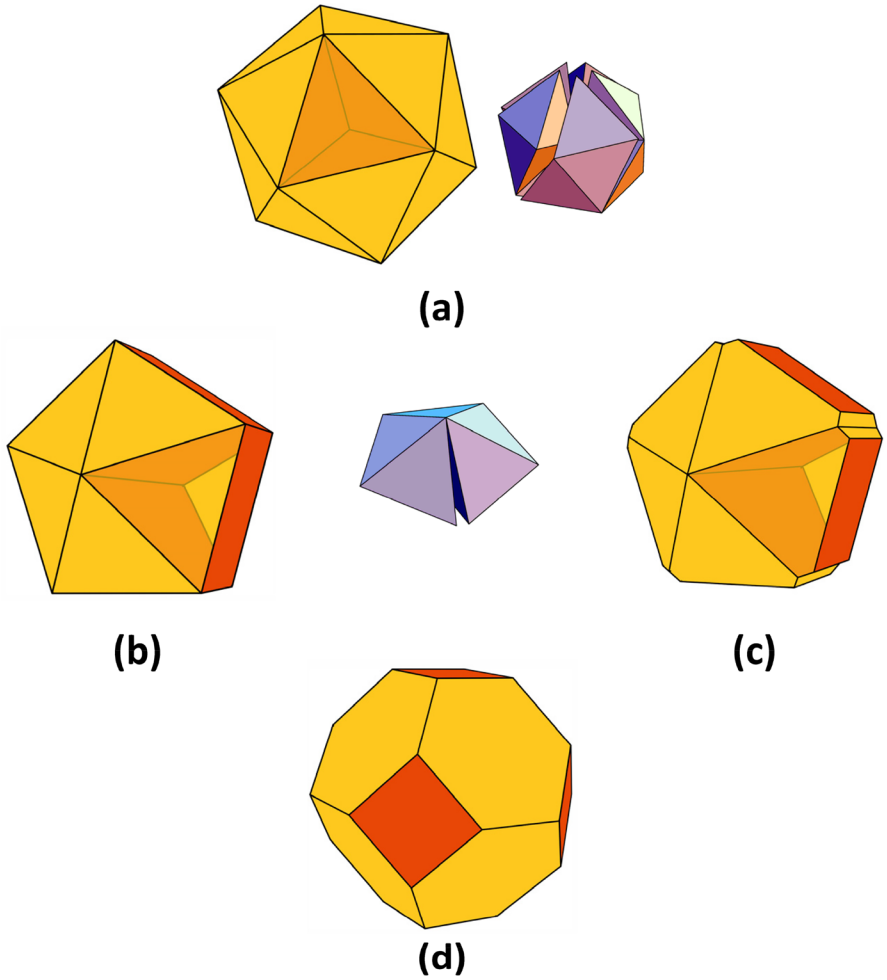

Figure 7. Major structural motifs for fcc metal nanocrystals: (a) Mackay icosahedron (Ih), (b) Ino decahedron (Dh), (c) Marks Dh, and (d) single-crystal truncated octahedron (TO). {111} facets are shown in orange, {100} facets are shown in red, and example twin planes are shown through semitransparent {111} facets. The small insets to the Ih and the Dh illustrate that regular tetrahedra are not space-filling for these geometries, so the red-orange shapes are strained. Used with permission of The Royal Society of Chemistry, from ref 138; permission conveyed through Copyright Clearance Center, Inc.

2.1. Atomistic Studies of Nanocrystal Structure

Atomic-scale studies of nanocrystal structure have been based on both quantum methods and empirical force fields. Many of these studies focus on finding minima in potential energy, where the potential energy is obtained from quantum total-energy calculations at zero K or from empirical force fields. Baletto and Ferrando wrote a comprehensive review of early theoretical studies of nanocrystal shapes.[156] In these early studies, quantum methods were mostly applied to subnanometer sized clusters, although a notable exception and an instructive example of such calculations is the 1997 study of Jennison, Schultz, and Sears.[157] They used DFT with the local density approximation (LDA)[158] to probe the relative energies of Ih and single-crystal Ru (fcc), Pd, and Ag nanocrystals with 55, 135, and 140 atoms.

With 55 atoms, both the CO and the Ih illustrated in Figure 8a,b are at magic sizes, while 135, although not a magic size, allows for relatively compact and symmetric structures to occur with single-crystal and Ih-like clusters, shown in Figure 8c,d. Clusters with 140 atoms, while also not magic sizes, possess compact and symmetric shapes with structures close to the Ih and fcc octahedron, as we see in Figure 8e for a nearly perfect octahedron. The procedure in Jennison's study was to create the various clusters in Figure 8, optimize the structure of each cluster by adjusting the atomic coordinates until the DFT force on each atom is suitably low, and then compare the total DFT energies of clusters with the same size and element but different shapes. In comparisons between Ih and fcc geometries for clusters with both 55 and 135 atoms, they found the Ih geometry was preferred (with a lower potential energy) for all metals, consistent with the arguments behind eq 1. For clusters with 140 atoms, the fcc cluster was preferred over the Ih for Ru and Pd, but not for Ag. In addition to being a landmark study in the use of quantum methods for the study of cluster structures, the approach in this work is also typical of that applied in many studies, both quantum and classical.[132,136,141,146,159−167]

Illustrative early studies using classical force fields are those of Cleveland and Landman[137] and Baletto et al.[136] Cleveland and Landman used an embedded-atom method (EAM) potential to study the structures of Ni clusters containing 142 to more than 5000 atoms. The EAM potential is a semiempirical, many-body force field that has been widely used for metals.[168,169] This potential consists of two major terms: a many-body embedding function, which yields the energy to embed an atom into the local electron density provided by the

https://doi.org/10.1021/acs.chemrev.2c00831
Chem. Rev. XXXX, XXX, XXX−XXX

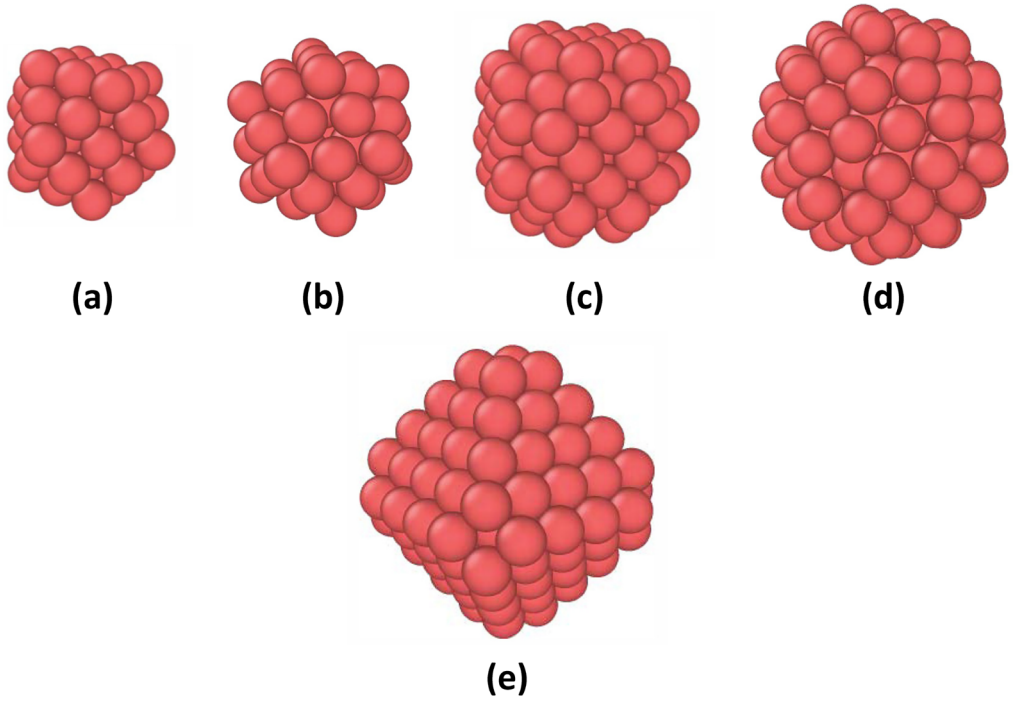

Figure 8. Cluster geometries probed in the study by Jennison, Schultz, and Sears:[157] (a) 55-atom CO, (b) 55-atom Ih, (c) 135-atom CO with single-atom corners truncated, (d) 135-atom Ih with single-atom corners truncated, and (e) 140-atom octahedron with the single-atom corners truncated.

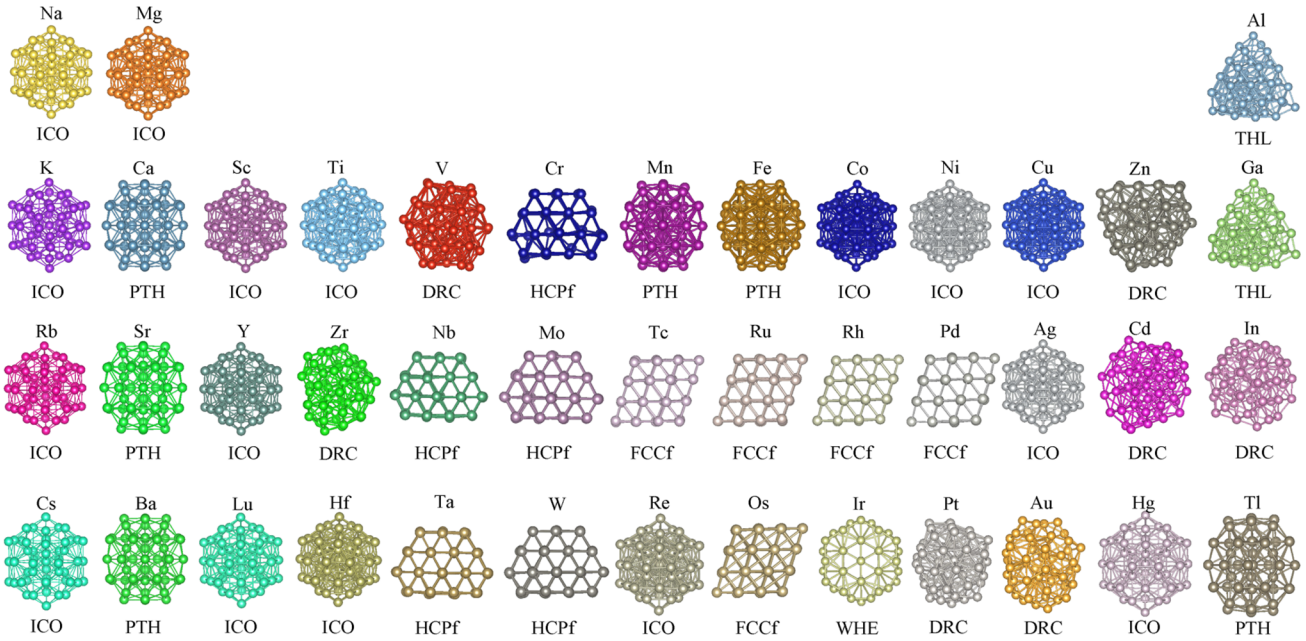

Figure 9. Putative global minimum configurations obtained for various 55-atom metal nanoclusters in the study of Piotrowski et al.[161] The structure for each element is indicated below the cluster, and the names are icosahedron (ICO), polytetrahedron (PTH), disordered reduced-core (DRC), hexagonal close-packed fragment (HCPf), face-centered cubic fragment (FCCf), tetrahedral-like (THL), and hexagonal close-packed wheel-type (WHE) structures. Reproduced with permission from ref 106. Copyright 2016 American Chemical Society.

other atoms in the system, and a short-range, two-body potential that provides core−core repulsion. Evaluation of the potential energy in an EAM calculation is considerably faster than in a quantum calculation, so much larger clusters can be studied. Cleveland and Landman considered various possible single-crystal truncated cubes and TO. They also studied multiply twinned structures such as Ih and various types of Dh, like the Ino and Marks Dh shown in Figures 7b,c. In line with the notions discussed above, they found that Ih clusters are favored for the smallest cluster sizes and that the Marks Dh is favored for intermediate sizes, larger than about 2300 atoms. They predicted that clusters larger than about 17 000 atoms are fcc.

Baletto and colleagues used EAM and simpler Rosato, Guillope, and Legrand (RGL)[170] potentials to study structural trends in Ag, Cu, Au, Pd, and Pt.[136] They considered three

https://doi.org/10.1021/acs.chemrev.2c00831
Chem. Rev. XXXX, XXX, XXX−XXX

different structural motifs, Ih, Dh, and TO, with cluster sizes up to 40 000 atoms. For all the systems considered, they found Ih are favored at small sizes, Dh at intermediate sizes, and TO at large sizes. However, the crossover sizes depended strongly on the material, and they concluded that the ratio of the bulk modulus to the cohesive energy per atom could account for differences in the crossover sizes of different metals.

Moving forward from this early work, more recent studies show new trends in the cluster size−shape relationship that do not always support the early studies. For example, Piotrowski et al. used quantum DFT to investigate the structures of 42 different metal clusters, all consisting of 55 atoms.[161] They investigated the effects of van der Waals (vdW) interactions, spin−orbit coupling, and the role of *d*-state localization on the cluster shapes. To identify putative global minima for these clusters, they searched 25−40 structural candidates for each element. Figure 9 shows the global minimum they identified for each element. Although 55 is a magic size for the Ih, more than half the clusters they studied did not prefer Ih shapes.

In perhaps the most extensive atomistic study of metal nanocluster geometries to date, Rahm and Erhart developed an algorithm, based on atomistic simulations in a constrained thermodynamic ensemble, to predict equilibrium shapes of nanoparticles described by EAM potentials.[141] They applied their algorithm to Cu, Ag, Au, and Pd particles containing up to 10 000 atoms. Similar to the early studies discussed above,[136,137] they examined the relative stabilities of Ih, Dh, and TO. Figure 10 shows their results for the most stable

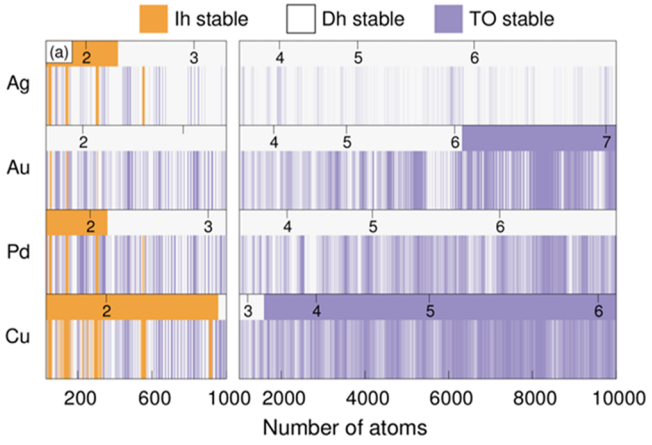

Figure 10. Relative stability of the three different motifs for Ag, Au, Pd, and Cu. Orange, white, and blue stripes indicate Ih, Dh, or TO motifs that are energetically the most stable. The bars in the upper part of each subpanel indicate the regions of stability that would be predicted from eq 1. The intervals are split into 40−1000 atoms to the left and 1000−10 000 to the right for clarity. Approximate diameters in nm are indicated at the top of each subpanel. Reproduced with permission from ref 141. Copyright 2017 American Chemical Society.

structure as a function of size, along with results predicted by their parametrized version of eq 1. Similar to the early predictions,[136,137] they found Ih are the most favored shape for the smallest cluster sizes. However, Ih are not exclusively favored, as both Dh and TO appear as energetically favored shapes for the smallest sizes. Moreover, the TO is not a predominant cluster for Ag, even in the 10 000-atom size range, and the TO is not exclusively preferred for the largest size of any element.

As is indicated in the work of Piotrowski[161] summarized in Figure 9 above, some metals are not predicted to form closed-shell structures at magic sizes and Au is an excellent example. There have been many theoretical studies of Au_{55}.[132,161,171−177] Although studies indicate Au possesses local minima with closed-shell structures at magic sizes, these are not always predicted to be the global minimum. Early studies with the many-body Gupta potential,[178] also known as the RGL potential, and quantum DFT probed Au clusters with 38, 55, and 75 atoms and showed amorphous structures have lower energies than highly ordered ones.[171,172] This finding is consistent with experimental ACSTEM experiments[179] and UV photoelectron spectroscopy[176] for Au_{55}.

In subsequent years, Bao et al. also performed global optimization studies (using the RGL potential) with the minimum hopping method to search for the minimum-energy structures of a series of Au nanocrystals, including Au_{55}.[174] They found that a single-crystal fcc cluster had the lowest energy and, interestingly, that the minimum-energy structure could change drastically with the addition of a single atom. They made the important points that experimental studies can neither control nor measure the cluster size to single-atom resolution and that experimental clusters can be kinetic structures or consist of isomers lying close in energy. Additionally, clusters are typically imaged on a substrate, which can affect the structure, and if the substrate has not affected the structure, the electron beam (e.g., in ACSTEM experiments) can.

In a more recent theoretical study, Schebarchov et al. used the Gupta (RGL) potential to characterize minima of Au_{55} using basin hopping.[180] They reoptimized selected minima using DFT with the commonly used Perdew−Burke−Ernzerhof (PBE)[181] generalized gradient approximation (GGA) exchange-correlation functional. This study was a *tour de force*, implementing many theoretical methods relevant for characterizing structure and dynamics of condensed-matter systems. They obtained the probability of observing a given minima at a fixed temperature T using the harmonic superposition method (HSM).[182] In the HSM, the canonical partition function can be written as

$$Z(T) = \sum_m g_m \, e^{-E_m/k_B T} \tag{2}$$

where the sum runs over all minima (or as many minima as can be identified), E_m is the potential energy of minimum m, and k_B is the Boltzmann constant. The degeneracy g_m for minimum m is given by

$$g_m = \frac{2N!}{o_m}\left(\frac{k_B T}{h\bar{\nu}_m}\right)^{3N-6} \tag{3}$$

where N is the number of atoms, o_m is the point group order, h is Planck's constant, and $\bar{\nu}_m$ is the geometric mean normal-mode vibrational frequency. It should be noted that other similar studies employ different forms for the partition function.[160,183] Thus, the occupation probability for minimum m at a temperature T, $p_m(T)$ is given by

$$p_m(T) = \frac{g_m \, e^{-E_m/k_B T}}{Z(T)} \tag{4}$$

In addition to identifying large numbers of energy minima and performing HSM analysis, they identified minimum-energy

https://doi.org/10.1021/acs.chemrev.2c00831
Chem. Rev. XXXX, XXX, XXX−XXX

pathways and transition states between pairs of neighboring minima using the doubly nudged elastic band method.[184,185] As I will elaborate below, this is kinetic information used to characterize mechanisms and rates for transitioning from one minimum-energy state to another.

Schebarchov and colleagues also characterized the structures of the clusters using common neighbor analysis (CNA). Nice descriptions of CNA are given by Faken and Jönsson,[186] as well as by Cleveland, Luedkte, and Landman.[164] In CNA, each pair of atoms is assigned a set of three integers $\{i, j, k\}$ that indicate the coordination of the atom pair: i, the number of shared (common) nearest-neighbors, j, the number of bonds between these common neighbors, and k, the number of bonds in the longest continuous chain formed by the j bonds between common neighbors. Based on all of its pair indices, an atom is assigned an identity, as discussed elsewhere.[164,186] Using CNA, they characterized individual atoms as Ih (ICO), hexagonal close packed (hcp), fcc, or ambiguous. Then entire cluster morphologies were classified as either ICO, Dh (DEC), fcc, twinned (TWI), hcp, or ambiguous (AMB), depending on the relative numbers of atom types they possessed.

Figure 11 shows a color-coded disconnectivity graph for the 500 lowest-energy minima that they found for Au_{55}. A

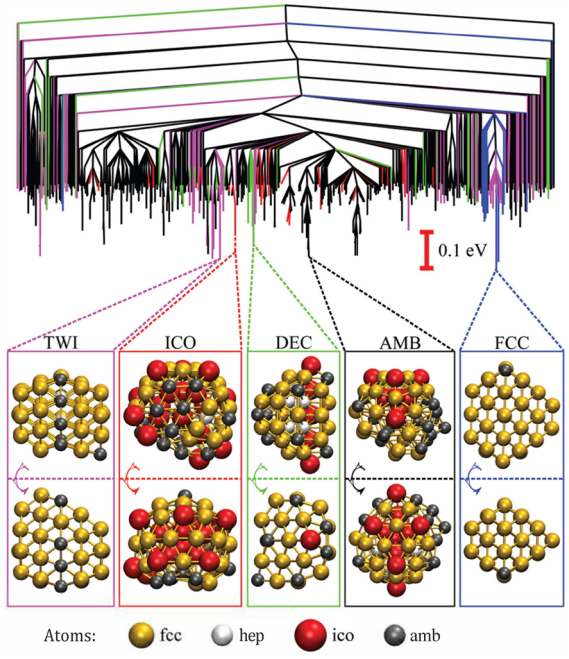

Figure 11. Color-coded disconnectivity graph for the 500 lowest-lying minima of Au_{55}. Branches leading to ICO minima are shown in red, DEC in green, FCC in blue, TWI in magenta, and AMB in black. Two different views are shown of the lowest-lying minimum for each motif, with atoms color-coded by the local environment: fcc in gold, hcp in white, ico in red, and amb in gray. Reproduced with permission from ref 180. Copyright 2018 Royal Society of Chemistry.

disconnectivity graph depicts the energies of various minima, as terminal points, along with the energies of the transition states between adjacent minima, depicted as branching points.[187] The lowest- and second-lowest energy minimum identified in this study were both fcc, and the lowest-energy minimum was the same as that found by Bao, as discussed above.[174] The disordered structure found in the earlier studies with the Gupta potential[171,172] ranked as the fifth lowest. From the occupation probabilities for the various structural motifs, they found that the fcc isomer is only highly probable at temperatures below 70 K, and after that, the disordered isomers were the most probable. Their result was consistent with experiment.[179]

Interestingly, when Schebarchov et al. reoptimized the lowest-energy isomers of the Gupta potential using DFT, there was a significant reordering of the energies, with minor structural changes. The lowest-energy isomer predicted with the Gupta potential did not even fall in the lowest 10 isomers at the DFT level. The lowest DFT isomer was amorphous and had subsurface voids. In a more recent study, Thorn et al. developed a neural network potential and used it to investigate the structures of a variety of small Au clusters.[177] For Au_{55}, they found similar amorphous cage structures to Schebarchov et al.[180] It should be noted that hollow structures have been observed in theoretical[175,188−192] and experimental[193] studies of other small Au clusters as well.

Studies have probed Au clusters with more than 55 atoms, especially at magic sizes for the Ih. Several studies have focused on Au_{147}, the next magic size after 55 for an Ih.[160,165,180,194,195] Li et al. examined the relative stabilities of Au nanoclusters with (near) Ih, Ino-Dh (see Figure 7b), and CO structures using a combination of an effective-medium-theory potential (similar to EAM) and high-level DFT calculations, based on the Tao−Perdew−Staroverov−Scuseria (TPSS)[196] meta-GGA exchange-correlation functional.[165] For Au_{147}, they found that a reconstructed Ih cluster with a distorted surface, shown in Figure 12a, had the lowest energy, lower than the energy of a perfect Ih. Interestingly, the TPSS meta-GGA and the commonly used PBE GGA yielded the same energetic trends for all the structures they investigated.

In the same study discussed above for Au_{55}, Schebarchov et al. also investigated Au_{147} using the Gupta potential. They found 10^4 minima and the lowest-energy structures were Dh and fcc with twins.[180] In a combined experimental X-ray absorption fine structure and DFT study, Duan et al. concluded that Au_{147} nanoparticles were Ih.[195] It should be noted, however, that their calculations were based on only two trial structures: Ih and CO.

More recent studies of the larger Au clusters also highlight the development of potentials with higher fidelity to DFT than the often-used EAM or EAM-like potentials. Using efficient empirical potentials, it is possible to perform more robust optimizations and to examine the statistical mechanics of the clusters in a more robust way than with DFT. For example, Jindal, Chiriki, and Bulusu developed an artificial neural network potential for Au[160] and deployed their potential to study Au_{147}. They employed a basin-hopping algorithm to search for the global minimum structure of Au_{147}, and they ran MD simulations at various temperatures to obtain thermal statistics. Their search for the global minimum revealed a relatively amorphous structure, shown in Figure 13b. DFT calculations with the PBE exchange-correlation functional confirmed the global minimum and indicated its energy was almost 4 eV lower than that of the Ih.

In their search for the global minimum, Jindal, Chiriki, and Bulusu uncovered 60 different isomers that possessed energies within 0.5 eV of the global minimum, all of which had lower energies than the Ih.[160] They calculated the rotational and vibrational partition function for each of the 60 isomers to obtain the probabilities of observing the various isomers as a function of temperature, in a method similar to the HSM

https://doi.org/10.1021/acs.chemrev.2c00831
Chem. Rev. XXXX, XXX, XXX−XXX

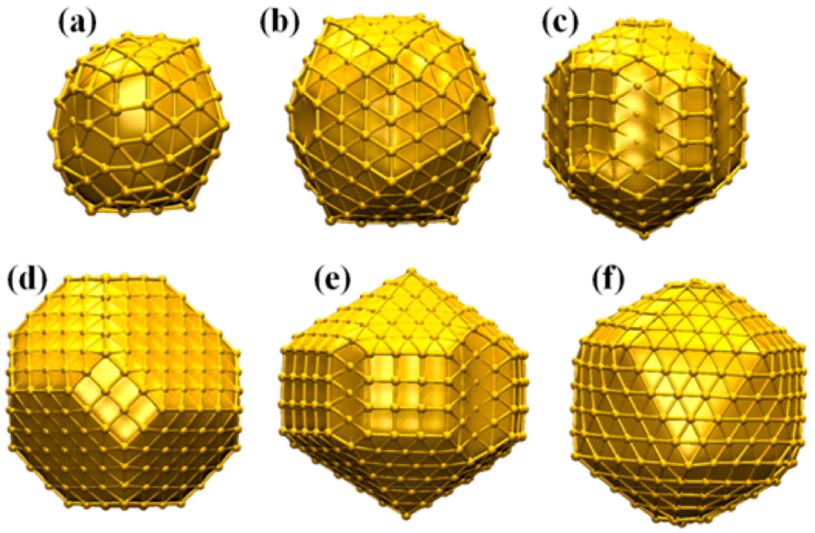

Figure 12. Structures of some of the clusters investigated in the study of Li:[165] (a) a reconstructed Ih for Au_{147}, (b) a reconstructed Ih for Au_{309}, (c) a reconstructed Dh for Au_{309}, (d) fcc Au_{549}, (e) Dh Au_{559}, and (f) a reconstructed Ih for Au_{564}. Reproduced with permission from ref 165. Copyright 2015 American Chemical Society.

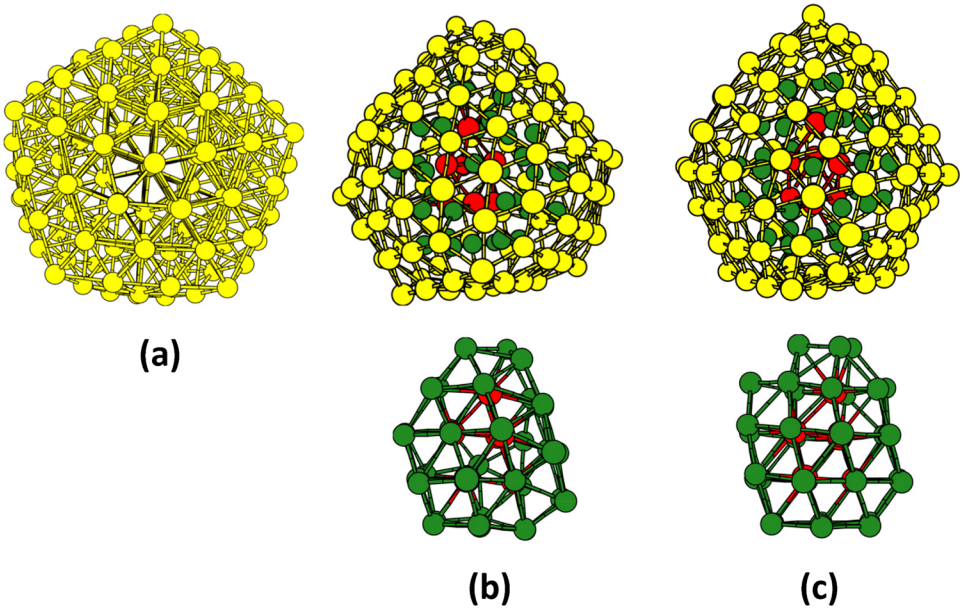

Figure 13. Various possible structures for Au_{147}: (a) Ih, which is a magic size at 147 atoms, (b) surface (yellow) and core (red and green) atoms of a relatively amorphous structure predicted by the anisotropic neural network potential of Jindal, Chiriki, and Bulusu,[160] that is 4 eV lower in energy than the Ih, and (c) surface and core atoms of the most probable structure at 300, 500, and 800 K. Reproduced with permission from ref 160. Copyright 2017 AIP Publishing.

described above. Interestingly, the most probable isomer over temperatures ranging from 300 to 800 K, shown in Figure 13c, was not the global minimum. They attributed this to the higher symmetry of the most probable cluster. From MD simulations, they also observed that both the core and surface atoms of Au_{147} are highly mobile, giving it fluxionality and possibly unique properties for catalysis.

Almost concurrently with the above study of Jindal et al.,[160] Tarrat, Rapacioli, and Spiegelman[194] used a density functional based tight binding (DFTB) approach combined with parallel tempering MD (PTMD) to probe various structures of Au_{147}. As discussed, for example, by Earl and Deem,[197] PTMD is a technique designed to sample temperature-dependent free-energy minima. PTMD involves running canonical-ensemble MD simulations in parallel on a set of replica systems, each at a different temperature. At the end of a fixed time interval, an attempt is made to exchange the configurations of a pair of neighboring replicas via a Monte Carlo (MC) trial, and the exchange is accepted with a probability satisfying detailed balance. The process is repeated until convergence of the sampling is achieved. At the highest temperatures, the replicas can rapidly cross high free-energy barriers in the system. Because configurations sampled at high temperatures can exchange with the low-temperature replicas, the low-temperature systems are able to cross high free-energy barriers to access various minima. Compared to the HSM, discussed above, PTMD is more accurate at determining the probabilities of various isomers because it is not limited to the harmonic

https://doi.org/10.1021/acs.chemrev.2c00831
Chem. Rev. XXXX, XXX, XXX−XXX

approximation, and it is not necessary to enumerate various isomers using structural optimization.

Using PTMD, Tarrat et al. generated various isomers of Au_{147}, and they optimized resultant structures from their PTMD calculations using DFT with various exchange-correlation functionals. Similar to Li et al.[165] and Jindal et al.,[160] they found the lowest-energy isomer from DFTB has an amorphous structure that is significantly lower in energy (by 13.1 eV) than the Ih. While optimizations with all the DFT functionals yielded similar isomers, these structures were different from those found with DFTB. Moreover, they found that no functional had the same energetic ranking as DFTB and that the energetic ranking of the isomers depended on the exchange-correlation functional. Interestingly, the LDA, PBEsol, and optB86b-vdw exchange-correlation functionals all predict the Ih to be the lowest-energy configuration, while the PBE, rPBE, and PW91 functionals indicated the lowest-energy isomers are amorphous.

Recently Settem et al. used PTMD, combined with energy minimization (similar to Tarrat et al.[183]) to study the equilibrium structures of Au clusters containing 90, 147, and 201 atoms.[183] As in some of the other studies discussed above, this study employed the RGL potential[170] to describe Au interactions. They compared results from PTMD to results using the HSM, discussed above (although they called this the harmonic superposition approximation, HSA). This study also featured CNA to characterize structural features of the clusters. Using the CNA signature, Settem et al. classified atoms into five different types, and from the relative proportions of these atom types, they deduced the nanoparticle structures at various temperatures.

Figure 14 shows a phase diagram of the fraction of shapes observed by Settem et al. for Au_{147} as a function of temperature. In addition to the well-known structures, they classify "twin" structures as structures having hcp atoms, "mix" structures as having combinations of various structural motifs, and "amorphous" as having greater than 60% of the atoms without a well-defined CNA signature. Consistent with Schebarchov et al.,[180] but in contrast to the DFTB and anisotropic neural network potentials, they found that a Dh is the global minimum for Au_{147}, and it is the most probable structure over a wide temperature range.

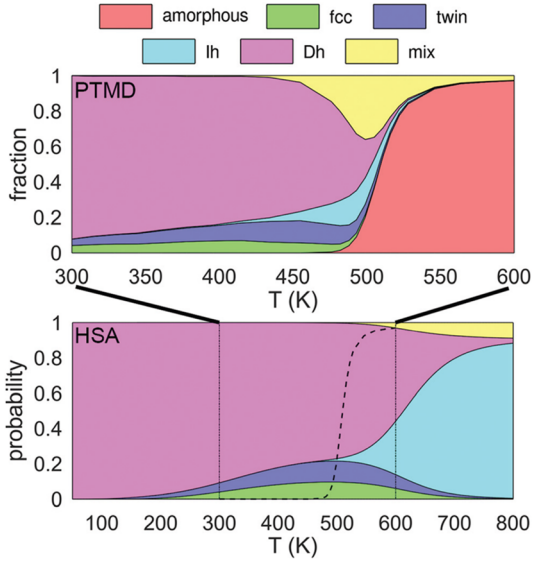

Figure 14. Frequency of various structures of Au_{147} nanoclusters as a function of temperature obtained from PTMD simulations (upper panel) and from the HSA (lower panel). Used with permission of The Royal Society of Chemistry, from ref 183; permission conveyed through Copyright Clearance Center, Inc.

Settem et al. emphasized differences between PTMD and the HSA (HSM) in the lower panel of Figure 14. Here, we see that there is reasonable (but not perfect) agreement between the HSA and PTMD at lower temperatures, but the agreement declines at high temperatures, where the PTMD simulations are more accurate. As the temperatures become sufficiently low, it is difficult to achieve good sampling of various nanocrystal structures because the fluctuation in potential energy is proportional to the temperature in the canonical ensemble. When the fluctuation is small (at low temperatures), MC trials used to swap different replicas will not succeed unless the replicas are placed at very closely spaced temperatures, which is computationally inefficient. Thus, they advocated using both the HSA and PTMD to sample nanocrystal structures from 0 K to melting and above.

We can infer the RGL melting temperature for Au_{147} from Figure 14, and this is around 500 K. It should be noted that recent studies of Zeni et al. indicate the RGL potential greatly underestimates the melting temperature of Au nanoclusters.[198] Nevertheless, PTMD can be a powerful tool to study minimum free energy shapes of small clusters, and this technique could be enlightening in future studies.

Atomistic studies have probed the structures of Au clusters with more than 147 atoms.[132,146,147,159,165,174,183,199−201] Several of these studies focused on magic sizes for the Ih and CO, 309, 561, and 923, and I will focus on these below. In the study of Li et al.,[165] discussed above and summarized in Figure 12, they considered the relative energies of clusters with structures close to Ih, Ino Dh, and CO at magic sizes and near-magic sizes. For Au_{309}, they found that the reconstructed Ih cluster with a distorted surface, as seen in Figure 12b, had a lower energy than a perfect Ih. The lowest energy structure they found for Au_{309}, with a slightly lower energy than the distorted Ih, was the reconstructed Ino Dh. As we see in Figure 12c, the reconstructed Ino Dh resembles a Marks Dh (see Figure 7c). This finding was consistent with experimental HAADF-STEM studies of Au clusters soft-landed on a carbon film,[202] as well as with earlier experimental and theoretical studies.[201] For clusters larger than Au_{549}, the fcc structures (CO and variants) became energetically the most favorable, although the energies of all clusters were close, partly supporting the experimental investigation by Foster, Ferrando, and Palmer, who found that the energies of the Dh and fcc cluster were close for Au_{561} soft-landed on amorphous silicon nitride.[131] At the largest size of Au_{923}, they found small energy differences among the high-symmetry Ih, Dh, and CO isomers, somewhat at odds with experimental studies of Au_{923} clusters, which indicated the energetic ordering fcc < Dh ≪ Ih.[128]

Jindal and Bulusu used their anisotropic neural network potential to probe the structures of Au_{309}, Au_{561}, and Au_{923}, all magic numbers for the Ih and CO.[147] They found that these clusters possess a distorted symmetric core covered by an amorphous shell. These core−shell structures were energetically preferred over perfect Ih and appear to be significantly more disordered than the reconstructed Ih and Dh clusters identified by Li et al.[165] (see Figure 12). Noting that these disordered structures have not been observed experimentally,[131,201,202] Jindal et al. calculated the probabilities of

https://doi.org/10.1021/acs.chemrev.2c00831
Chem. Rev. XXXX, XXX, XXX−XXX

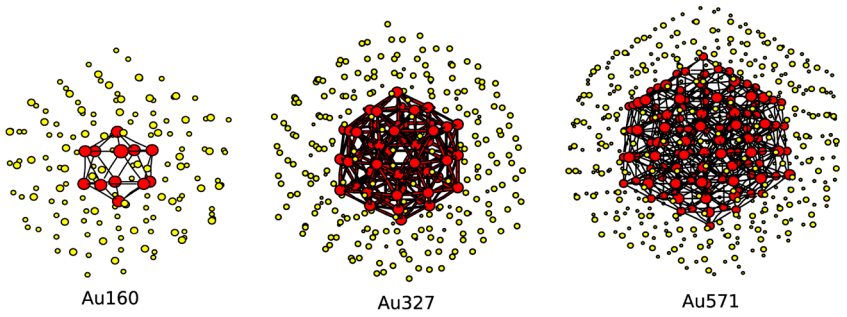

Figure 15. New magic-sized Au clusters proposed by Jindal and Bulusu: Au_{160}, with a 12-atom ordered core, Au_{327}, with a 54-atom ordered core, and Au_{571}, with a 146-atom ordered core. Core atoms are shown in red with bonds and amorphous shell atoms are shown in yellow. Reproduced with permission from ref 147. Copyright 2020 AIP Publishing.

observing various isomers of (magic sized) Au_{309}, similar to the HSM discussed above. This analysis revealed that the symmetric isomers, particularly the Ih, were greatly favored over the lower-energy disordered structure because of their larger vibrational partition functions, partially explaining their apparent discrepancy with experiment.

Jindal and Bulusu also identified cluster sizes that contained symmetric Ih cores. As shown in Figure 15, these were Au_{160}, which possesses an ordered core of 12 atoms (13 is a magic size for an Ih) Au_{327}, with an ordered core of 54 atoms (55 is a magic size for an Ih), and Au_{571}, with a core of 146 atoms (one less than the magic size for an Ih). They noted that in each of these structures, the symmetric Ih core is missing the central atom and covered by two amorphous layers. As discussed above, hollow core Au clusters have been observed in other studies.[175,188−192] They proposed that these are new magic sizes for Au clusters.

Considering the wide and varied array of results, we see there are large discrepancies, even in quantum DFT calculations, when it comes to describing the structures of Au clusters, and there is room for new theoretical developments. It is desirable to have a theoretical description that combines the accuracy of high-level DFT calculations with the inherent ability of PTMD to sample cluster free energies at various temperatures. Interestingly, calculations considering cluster free energies (or partition functions) indicate that the clusters with the minimum energies are not always probable, even at moderate temperatures.

To complicate matters, experiments have raised the issue of whether the shapes of even moderate-sized clusters are equilibrium shapes. For example, Wells et al. used HAADF-ACSTEM to characterize the shape distributions of size-selected Au clusters containing 561, 742, and 923 atoms grown in vacuum and deposited on a substrate.[130] They found that these Au clusters had nearly identical shape distributions dominated by Dh. This led them to conclude that the shapes were determined by solidification from the liquid state early in their growth, followed by nonequilibrium growth of a small template. Later experiments by Foster, Ferrando, and Palmer were able to resolve a temperature range over which they believed they could achieve equilibrium structures of Au_{561} soft-landed on a substrate.[131] These experiments showed the most energetically stable shape for Au_{561} was fcc, which was only slightly preferred over the Dh.[128] The above theoretical studies do not address the gap between thermodynamics and kinetics, although being able to predict thermodynamics is an important prerequisite for understanding kinetics.

Although the above discussion was heavily focused on Au nanocrystals, with good reason, as many cutting-edge theoretical studies have focused on Au, the nanocrystalline structures of other metals are not without interest.[159,162,163,203−208] I will highlight some of these studies below. Also, the studies discussed above all addressed clusters in vacuum. Going from vacuum to a solution environment requires many extra features in a theoretical description than those contained in the studies discussed above. The experimental studies outlined in Figure 3 occur in a liquid environment away from zero K, where intuitively solvent and additive adsorption on nanocrystal surfaces can determine the structures of metal nanocrystals.

Very few studies have considered the influence of a solution environment in atomic-scale studies of cluster shape beyond the single-nanometer size range. DFT studies have attempted to model the influence of a solution environment on nanocrystal structure by including one or more solvent layers or capping molecules around a nanoparticle surface. For example, Guedes-Sobrinho et al. used DFT to study the influence of PH_3 and SH_2 ligand adsorption on the structures of Pt_{55} and Au_{55} nanoclusters.[209] Similar to the study of Piotrowski et al.,[161] discussed above and summarized in Figure 9, they found these clusters had a disordered-reduced core (DRC) structure (and not an Ih, as the magic number would suggest) in the absence of ligand binding. However, the stability of the Ih structure increased as the number of adsorbed ligands increased from 1 to 18 and the DRC and Ih were nearly degenerate with 18 adsorbed ligands. They explained this trend in terms of the clusters possessing a cationic core with an anionic shell. The attractive core−surface Coulomb interactions lead to compression of the core, which is relieved by reducing the number of atoms in the core region and forming the DRC structure. The addition of surface ligands decreases the core−shell polarization of the clusters, which reduces the core−shell Coulomb interaction, mitigates the strain on the core, and stabilizes the Ih structure.

Chan and colleagues used DFT to quantify how adsorbed water influences the shapes of small Au nanocrystals.[210] They found that nanoclusters with mostly {100} facets that were (meta)stable in vacuum, Au_{55} and Au_{147} with Ino-Dh shapes, became unstable and transformed into {111} faceted shapes when they contained a layer of adsorbed water. This group also investigated how the adsorption of hydrated polyethylene glycol (PEG) ligands affects the shapes of Au nanoparticles.[133] Interestingly, they found that PEG adsorption stabilizes nanostar Dh Au_{54} more than compact Ih Au_{55} or TO Au_{79}.

https://doi.org/10.1021/acs.chemrev.2c00831
Chem. Rev. XXXX, XXX, XXX−XXX

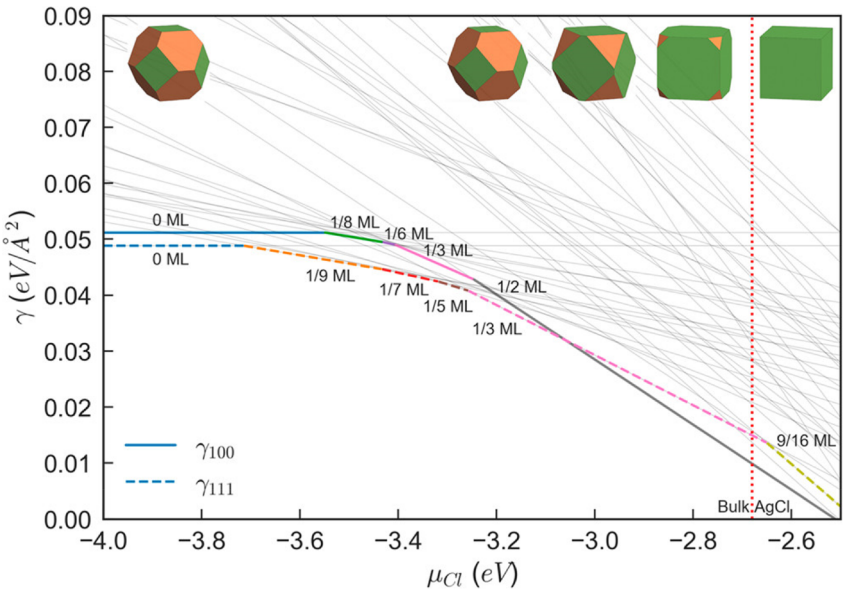

Figure 16. Surface energies γ of Ag(100) and Ag(111) for different surface coverages of Cl as a function of the solution-phase Cl chemical potential μ_{Cl}. Each line represents one of the Cl surface configurations considered. Colored regions of the plot represent the minimum γ on each surface: minimum surface energies on Ag(100) are shown with solid lines and those for Ag(111) are shown with dashed lines. Wulff shapes are shown for several values of μ_{Cl}, with {111} facets in orange and {100} facets in green. The vertical red line at $\mu_{Cl} = -2.68$ eV denotes where the formation of bulk AgCl is thermodynamically favored over chlorine-adsorbed Ag surfaces. Reproduced with permission from ref 212. Copyright 2019 American Chemical Society.

2.2. Surface Energies and Wulff Shapes

2.2.1. Surface Energies in DFT Calculations. Outside of full atomistic studies, several investigators have used DFT calculations to infer the influence of ligands or a solution environment on the Wulff shape of a metal nanocrystal.[152,211−217] The Wulff shape of a sufficiently large nanocrystal is one that minimizes the surface energy.[142,218−221] Facets in the Wulff shape have the property that

$$\frac{\gamma_i}{h_i} = \lambda \tag{5}$$

where γ_i is the surface energy of facet i, h_i is the length of the normal vector from the crystal center to facet i, and λ is a constant. Equation 5 is valid for all facets in the Wulff shape and indicates that the length of h_i for facet i is proportional to γ_i. More elaborate formulations exist to calculate thermodynamic nanocrystal shapes. For example, Marks and colleagues,[111,161] and Barnard[222] have developed modified Wulff constructions that can also predict twinned nanocrystals as thermodynamic shapes.

It is evident from eq 5 that to obtain the Wulff shape, one must calculate the surface energies of all relevant facets. This can be done via first-principles DFT calculations or by classical MD simulations. In DFT calculations where the surface is represented by a periodic slab, the surface energy γ is given by

$$\gamma(\{\mu_i\}) = \frac{G_{slab} - \sum_i N_i\mu_i}{2A} \tag{6}$$

Here, G_{slab} is the free energy of a surface slab containing adsorbed species. G_{slab} is often taken as the total energy in a DFT calculation at zero K. $\sum_i N_i\mu_i$ is the sum of the product of the number N_i and the chemical potential μ_i of species i and A is the surface area of the slab. The factor of 2 presumes a symmetric slab is used, with equal compositions and configurations of adsorbed species on both sides of the slab. However, species are adsorbed to only one side of the slab in many such calculations, in which case the factor of 2 is absent from the denominator and the surface energy of a bare slab with the bulk metal termination needs to be subtracted from eq 6. The use of first-principles total energies to construct thermodynamic quantities, such as the surface energy, is termed *ab initio* thermodynamics.[223,224]

As an example of the above procedure, Chen et al. conducted a joint experimental and theoretical study of the influence of solution-phase chloride on the Wulff shapes of Ag nanocrystals.[212] They used DFT to calculate the surface energy of chloride-covered facet i [i = Ag(100) or Ag(111)] γ_i using

$$\gamma_i = (E_{i+Cl} - N_{Ag}\mu_{Ag} - N_{Cl}\mu_{Cl})/A - \gamma_{bulk,i} \tag{7}$$

where E_{i+Cl} is the total energy of a {100} or {111} slab containing Cl in which the atomic positions of the atoms and adsorbates on one side of the slab are relaxed until the force on each atom is suitably low, while Ag atoms on the other side of the slab are frozen at the bulk coordinates. N_{Ag} is the number of Ag atoms in the slab, μ_{Ag} is the energy per atom of bulk Ag, N_{Cl} is the number of adsorbed Cl atoms, and μ_{Cl} is the chemical potential of solution-phase Cl. μ_{Cl} was taken as the independent variable in this surface-energy calculation. Because Cl was adsorbed to only one side of the slab in this study, $\gamma_{bulk,\,i}$ was given by

$$\gamma_{bulk,i} = \frac{E_i - N_{Ag}\mu_{Ag}}{2A} \tag{8}$$

Here, E_i is the energy of a two-sided slab of facet i in which all the atomic positions are fixed at bulk values.

To assess possible Wulff shapes, Chen and colleagues calculated the total energies of various slabs containing Cl.[212] They considered 21 different Cl coverages/configurations on Ag(100) and 23 on Ag(111). The various configurations included Cl adsorbed on top of the surfaces as well as

https://doi.org/10.1021/acs.chemrev.2c00831
Chem. Rev. XXXX, XXX, XXX−XXX

substitutional configurations, in which Cl mixed into the Ag surfaces. For each of the 44 total configurations, they plotted the surface energy as a function of μ_{Cl}. Figure 16 shows the results of these calculations. It can be seen that Cl-covered Ag(111) surfaces have the lowest energies for the lowest values of the chemical potential. As the chemical potential increases, there is a crossover after which Ag(100) surfaces have the lowest energies.

The inset figures indicate the Wulff shapes implied by the lowest surface energies in Figure 16. For the lowest chemical potential values, where Ag is bare, a TO is predicted to be the Wulff shape. As μ_{Cl} increases, the Wulff shape becomes a CO, then a truncated cube. Finally, when μ_{Cl} surpasses the value at which AgCl is formed, a cube is predicted. Incidentally, there was good agreement between theoretical predictions and the experimentally synthesized shapes as a function of solution-phase chloride concentration for this work.

The surface energy can be related to the binding energy of an adsorbate. The binding energy E_{bind} of an adsorbate a on a surface slab containing N_a adsorbates is given by

$$E_{bind} = \frac{E_{slab+a} - E_{slab} - N_a\mu_a}{N_a} \quad (9)$$

where E_{slab+a} is the total energy of a metal surface slab containing N_a adsorbates, E_{slab} is the energy of the bare slab, and the chemical potential of a μ_a is often taken as the total energy of a in vacuum. Comparing eq 9 to eq 6 and equating the free energy of the slab to the total energy from DFT, we have

$$\gamma = \frac{E_{slab+a} - N_M\mu_M - N_a\mu_a}{2A} \quad (10)$$

where N_M and μ_M are the number of metal (M) atoms and the energy per atom of a bulk metal atom, respectively. The surface energy of a bare slab with no adsorbates γ^0 is given by

$$\gamma^0 = \frac{E_{slab} - N_M\mu_M}{2A} \quad (11)$$

Thus, we have

$$\gamma = \gamma^0 + \frac{E_{slab+a} - E_{slab} - N_a\mu_a}{2A} \quad (12)$$

Defining the adsorbate coverage per unit area as

$$\theta = \frac{N_a}{2A} \quad (13)$$

we have

$$\gamma = \gamma^0 + \theta E_{bind}(\theta) \quad (14)$$

In this way, we see how the binding of adsorbed solution-phase species, such as capping molecules and other additives, can affect the surface energy.

With insight from eq 14, a line of investigation in several groups has been to use DFT to calculate the binding energy of capping agents on various crystal facets to discern their likely effect on crystal shape.[215,225−233] For example, Kilin, Prezhdo, and Xia used DFT calculations to understand how citric acid as a capping agent promotes the formation of {111}-faceted nanocrystals in solution.[225] They found that the approximate 3-fold symmetry of citric acid matches that of Ag(111) and results in four silver−oxygen bonds, while citric acid forms only two bonds with Ag(100) because of geometry mismatch. Moreover, citric acid changed its structure when binding to Ag(111) to facilitate even stronger binding to Ag(111) than to Ag(100), by greater than 10 kcal/mol. Such a difference agreed with experiment.

Chiu et al. presented an approach for designing organic molecules with predictable binding selectivity to metal surfaces.[233] They found that geometric matching of an aromatic ring molecule with a {100} or {111} surface, along with its electrostatic potential, can determine its binding selectivity to Pt and Pd surfaces. An attractive aspect of this study was the agreement of the theoretical quantum calculations with experimental synthesis and characterization.

Also considering the binding-energy formalism, Chen and Fichthorn used DFT to study the binding of various alkylamine isomers to Cu(100) and Cu(111).[231] Their DFT calculations, as well as earlier ones,[215,230] indicated that alkylamines bind to these Cu surfaces via their N atoms and, specifically, with the N atoms directly above Cu surface atoms. Thus, a large component in finding suitable capping molecules was identifying molecules whose geometries matched with underlying Cu surfaces. Figure 17 shows two candidate capping molecules with selective binding to Cu(100): pentane-1,1,5,5-tetramine (PTA), and Cu(111): 1,3,5-triazinane (TZ). In addition to geometry matching with the surface, they discussed that factors such as capping-molecule density and interactions between adsorbed capping molecules can also play a role in capping molecule efficacy.

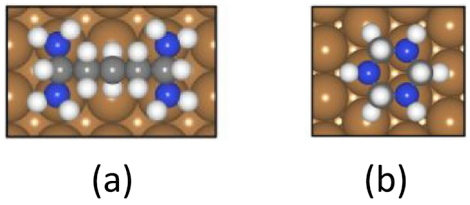

Figure 17. Top-down views of the optimal configurations of PTA on Cu(100) (a) and TZ on Cu(111) (b). Nitrogen is blue, carbon is gray, hydrogen is white, and Cu is brown. Used with permission of The Royal Society of Chemistry, from ref 231; permission conveyed through Copyright Clearance Center, Inc.

Solvent is important in solution-phase syntheses, and there are various ways to include its effects in calculations of the surface energy. Figure 18, taken from the review of Ringe et al.,[234] nicely depicts various theoretical approaches for describing solvent in calculations of liquid−solid interfaces. Although their review focused on electrochemistry, the basic principles are also relevant to the solution-phase growth of metal nanocrystals.

The most accurate way to describe the solid−liquid interfacial free energy is with a fully quantum description of all the surface and solution species, embodied in the left-most panel of Figure 18. To my knowledge, this approach has not yet been applied to nanometer-sized metal particles in solution. Moving to the center-left panel in Figure 18, we reach a second approach, which involves including solvent through empirical force fields. In the review of Ringe et al., a combined classical-quantum approach is presented, in which the solvent is described by a force field and the surface plus adsorbed species of interest are described quantum mechanically.[234] However, in metal nanocrystal growth, entirely classical, force-field based approaches have been employed and I will discuss these below.

https://doi.org/10.1021/acs.chemrev.2c00831
Chem. Rev. XXXX, XXX, XXX−XXX

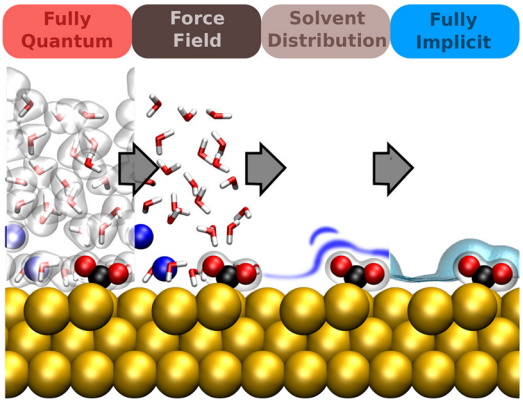

Figure 18. Hierarchy of coarse-graining approaches for liquid–solid interfaces. The sketch depicts an aqueous electrolyte with salt ions (blue spheres) and dissolved CO_2 (red and black molecules) at a crystalline surface. Starting from a fully explicit quantum mechanical description (far left, indicated by electron density iso-surfaces), one can coarse-grain away electronic degrees of freedom to arrive at a force field description (center left). From that one can gradually remove nuclear solvent degrees of freedom to represent solvent molecules, e.g., only through their spatial distributions or correlation functions (center right). Finally, replacing this with simply a polarizable continuum, one arrives at fully implicit models (far right). Reproduced with permission from ref 234. Copyright 2022 American Chemical Society.

The accuracy of classical force-field approaches depends on the quality of the force field.

The most common way to include solvent in DFT calculations is contained in the right-most panel of Figure 18. Here, solvent is described via fully implicit schemes, which ignore solvent structure and treat it as a polarizable continuum. As discussed by Ringe et al.,[234] many modern DFT codes contain options for including implicit solvent and the approach for calculating surface energies is the same as that outlined in eqs 6–14. Implicit solvent has been included in a few studies of metal nanocrystal Wulff shapes.[212,216] For example, Löfgren and colleagues demonstrated that including implicit solvent–surface interactions led to qualitative changes in the predicted Wulff shapes of halide-covered Au and Pd nanocrystals.[216]

2.2.2. Surface Energies in Classical Force-Field Calculations. Solvent can be included in surface-energy calculations by using classical force fields. In these calculations, the solid surface is treated as a slab and the liquid phase is simulated explicitly, at the desired thermodynamic conditions (e.g., density and temperature in the canonical ensemble). As implied by its position in Figure 18, this approach can be highly accurate in that the structure of the liquid phase near to and far from the solid surface is given precisely. If the force field is sufficiently accurate and due diligence is given to calculating the required ensemble averages, then the classical force-field approach can be useful.

Like the DFT approach, the solid–liquid interfacial free energy γ_{sl} is the free-energy change when creating a unit area interface between a solid and a liquid from the individual bulk phases. A variety approaches have been proposed to compute γ_{sl},[235−243] and Qi and Fichthorn developed a method applied to nanocrystal shapes in solution.[235,244] As shown in Figure 19, this method involves creating a six-step, reversible process by which a liquid–solid interfacial system is transformed into bulk liquid and solid.

In step 1 of Qi and Fichthorn's method, four Gaussian walls, repulsive to both the liquid and the solid, are gradually switched on at both liquid–solid interfaces in the periodic system. Step 2, which commences after the walls are fully implemented, involves gradually reducing the magnitude of the liquid–solid interaction until it is zero. When the liquid–solid interaction is zero, there are two systems: a liquid system confined by the Gaussian walls with vacuum where the solid used to reside and a solid system confined by Gaussian walls with vacuum where the liquid used to reside, as shown in step 2b. In steps 3 and 4, the vacuum is gradually removed from the liquid–vacuum system and then the walls are removed, to recover bulk liquid. In steps 5 and 6, the vacuum region is gradually repopulated by solid, the walls are removed, and the solid system with twice the volume of the original system is replaced by a periodic solid with the volume of the original solid region. After steps 5 and 6, a bulk solid is achieved.

For all steps in Figure 19 except step 3, the free-energy change ΔF_i for step i is obtained using thermodynamic integration (TI) and is given by

$$\Delta F_i = \int \left\langle \frac{dU}{d\lambda} \right\rangle d\lambda \tag{15}$$

where U is the potential energy and λ is a parameter that varies between 0 and 1 and couples to the relevant interactions in Step i. The free-energy change for step 3 is given by

$$\Delta F_3 = \int f_p \, dl \tag{16}$$

where f_p is the force from the periodic images, which grows as the vacuum spacing is reduced and the liquid becomes a bulk. The interfacial energy per unit area is then given by

$$\gamma_{sl} = -\left(\frac{\sum_{i=1}^{6} \Delta F_i}{2A} \right) \tag{17}$$

Qi and Fichthorn applied their method to understand the thermodynamic influence of polyvinylpyrrolidone (PVP) on the Wulff shapes of Ag nanocrystals in ethylene glycol (EG) solvent. They employed the metal–organic many-body (MOMB) force field comprised of the CHARMM force field for liquid-phase interactions among the organic species,[245−248] an EAM force field for Ag,[249] and a force field fit to DFT forces and binding energies of EG and PVP to surfaces of Ag.[250] They considered Ag nanocrystals consisting of two different facets {111} and {100}. From eq 5, Wulff shapes with these two types of facets can have the range of shapes depicted in Figure 20, depending on the ratio of their surface energies. For various nanocrystal environments, ranging from vacuum to EG solution only, to EG+PVP solutions, they found the preferred Wulff shape was always a TO. This was because the molecule–surface interactions were not sufficiently strong to overcome the metal contribution to the surface energy. This work addressed experimental studies by the Xia group,[251−254] in which Ag nanocubes were grown from cubic Ag seeds in EG solution with PVP as a capping agent. Their conclusion was that the experimental structures were likely kinetic structures and not thermodynamic ones. A similar conclusion was reached in the experimental study of Chen et al.[255]

https://doi.org/10.1021/acs.chemrev.2c00831
Chem. Rev. XXXX, XXX, XXX−XXX

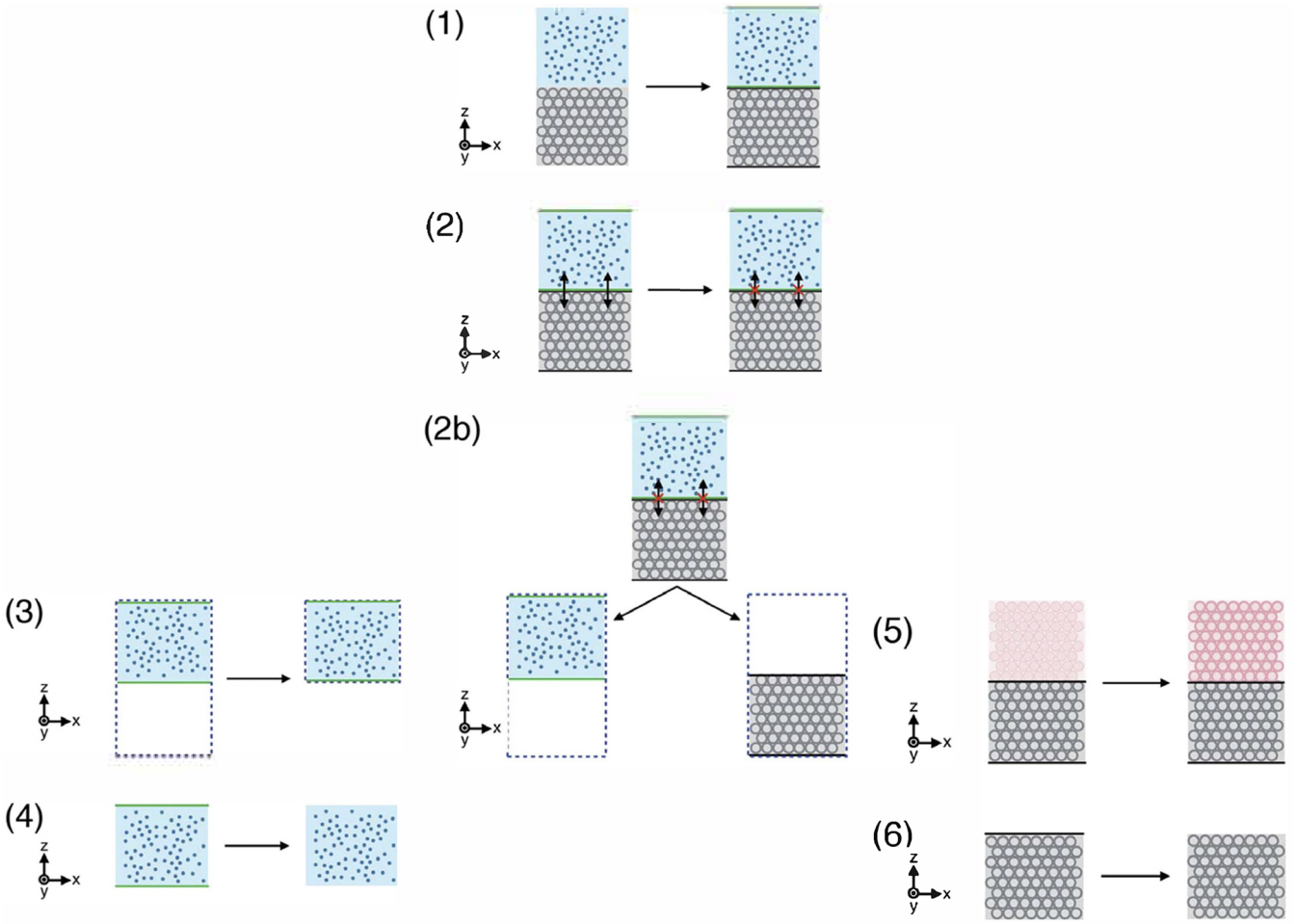

Figure 19. Stepwise illustration of the multischeme TI method. The solid and liquid phases are shown in gray and blue, respectively. Pink particles in step 5 represent an additional frozen solid bulk that helps to recover the periodic boundary conditions in the z direction for the solid. A description of each step is given in the text. Reproduced with permission from ref 235. Copyright 2016 AIP Publishing.

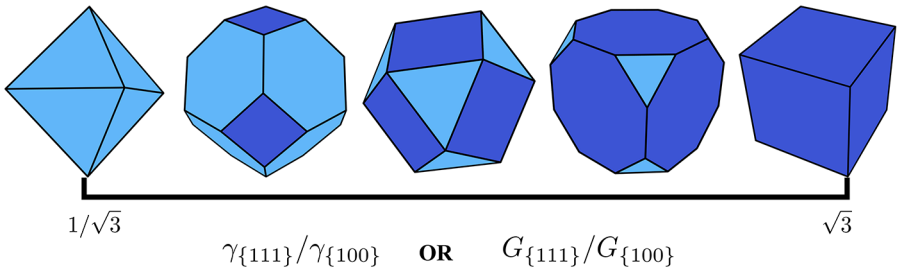

Figure 20. Thermodynamic ($\gamma_{\{111\}}/\gamma_{\{100\}}$) or kinetic ($G_{\{111\}}/G_{\{100\}}$) Wulff shapes for an fcc crystal containing two different types of facets: {111} and {100}, {111} facets are light blue, and {100} facets are dark blue. Reproduced with permission from ref 214. Copyright 2021 American Chemical Society.

3. KINETICS OF NANOCRYSTAL STRUCTURE

Although many theoretical studies of nanocrystal structures have focused on thermodynamics, as discussed above, it is evident the shapes of nanocrystals with sizes as small as 3 nm can be kinetic in origin. For example, Wells et al. reached this conclusion in their studies of Au clusters containing 561, 742, and 923 atoms.[130] Another compelling experimental study is by Wang and colleagues.[256]

Wang et al. demonstrated that the twin structure of a Pd nanocrystal correlates with the initial reduction rate in the synthesis.[256] They studied the growth of Pd nanocrystals from the reduction of Na_2PdCl_4 by EG, diethylene glycol (DEG), and triethylene glycol (TEG) in the presence of PVP. They found that the twin structure of the synthesized nanocrystals depended on the reductant and the temperature. Using UV–vis spectroscopy, they determined pseudo first-order, Arrhenius rate constants for the reduction of $PdCl_4^{2-}$ for various temperatures and in various concentrations of EG, DEG, and TEG. They found the activation energy depended on the size of the polyol. Using their kinetic data, they calculated the initial reduction rate of $PdCl_4^{2-}$ and they were able to correlate this with the synthesized nanostructure, as shown in Figure 21.

https://doi.org/10.1021/acs.chemrev.2c00831
Chem. Rev. XXXX, XXX, XXX−XXX

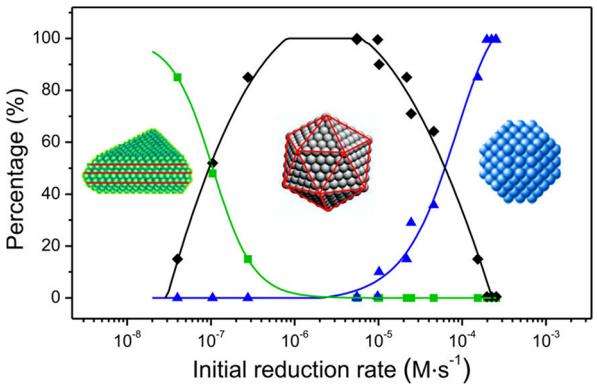

Figure 21. Relative distribution of the twin structure of Pd nanocrystals as a function of the initial reduction rate. The percentages of single-crystal, multiply twinned, and staking-fault-lined structures are shown in blue, black, and green, respectively. Reproduced with permission from ref 256. Copyright 2015 American Chemical Society.

These results indicated that the reduction rate is a quantitative knob for obtaining a desired nanostructure, with near 100% stacking-fault lined nanostructures at sufficiently low reduction rates and single-crystal fcc structures at the highest reduction rates. Their studies demonstrated the importance of the reduction rate in influencing the formation of various types of nanocrystal seeds.

Thus, the above experiments and many others, some of which will be discussed below, indicate kinetics can play an important role, perhaps the dominant role, in determining the structures of metal nanocrystals in solution-phase syntheses. Like the thermodynamic studies discussed above, theoretical kinetic studies of nanocrystal shapes range from the atomistic to the continuum level, in a multiscale way. Below, I discuss various kinetic studies of nanocrystal growth, beginning with those on the atomic scale.

3.1. Atomistic Studies of Nanocrystal Kinetics with Molecular Dynamics

The most detailed studies of nanocrystal growth and transformation kinetics are based on MD simulations. Although direct MD simulations have been limited to $\sim\mu$s times and often fall short of experimental time scales, such simulations can still provide insight into experiments. MD simulations can also be run with various acceleration techniques and combined with macroscopic theories so they can provide insight into mechanisms underlying nanocrystal shape transformations. Below, I provide examples of all these categories of study.

One of the earliest studies of metal nanocrystal transformation kinetics was performed by Wales and Munro.[257] They investigated the minimum-energy shapes and shape transformations of Ag, Ni, and Au nanocrystals with 55 and 147 atoms (magic sizes for Ih and CO) using the Sutton-Chen[258] and the Murrell and Mottram[259] potentials. They used an eigenvector following technique to quantify minima for these potentials, as well as transition states, or first-order saddle points on the potential-energy surface. The difference between the potential energy at a minimum and the transition state between a nearest-neighbor minimum is the energy barrier E_b for a transition between the minima. This transition has a rate r of the approximate form

$$r = A \exp\left(-\frac{E_b}{k_B T}\right) \tag{18}$$

where A is the pre-exponential factor. They rigorously distinguished the minima and transition states by quantifying the eigenvalues of the Hessian matrix of second derivatives of the potential energy with respect to the Cartesian coordinates of the atoms comprising the clusters. They also obtained the preexponential factor A from the eigenvalues of the Hessian matrix, and I will elaborate on this procedure below. They found that cluster transformations occurred via concerted diamond−square−diamond (DSD) mechanisms, first identified to characterize transitions in boranes and carboranes.[260]

In her recent review,[119] Baletto pointed out that a DSD mechanism also applies to concerted transitions between Ih and Dh. Figure 22, from Baletto's review,[119] depicts and

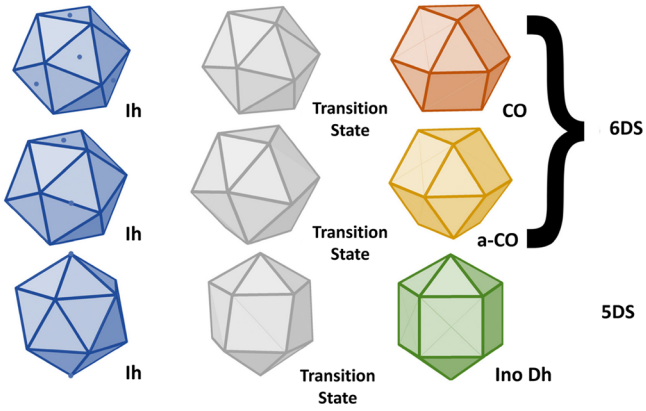

Figure 22. Three main half diamond−square mechanisms. In all cases, the initial state is an Ih (blue), and there are three different transition states (gray) for the final states of CO, anti-CO (a-CO), and Ino Dh. The small blue circles on the Ih delineate the rotation axes. Reproduced with permission from ref 119. Copyright 2019 IOP Publishing.

elaborates upon the initial, transition, and final states for DS transitions. In the 6DS mechanism, which applies to concerted transitions between Ih and CO, all the square facets of a CO distort into diamonds and fold along their shortest diagonal, generating two equilateral triangles and resulting in an Ih. The 5DS, which is the mechanism for the concerted transformation between Dh and Ih, involves the rotation of one of the two pentagonal caps on a Dh to distort the square sides into rhombi. Each rhombus then splits into pairs of equilateral triangles, generating an Ih. Baletto also introduced a new 6DS mechanism, in which an anti-CO converts to an Ih, depicted in the middle panel of Figure 22, and pointed out that DSD refers to the initial and final states being Ih. Thus, the conversion of an Ih to a CO or an anti-CO is a 6DS mechanism and the conversion of an Ih to a Dh is a 5DS mechanism.

Since the initial study of Wales and Munro, there were several studies of the Dh → Ih transition in fcc metal nanocrystals.[120,261−266] For example, Fichthorn and Yan used the climbing-image nudged elastic band method (CI-NEB)[185] to characterize concerted 6DS and 5DS mechanisms for Ag (described by an EAM potential[249]), Ih, CO, and Dh of different magic sizes.[120] As shown for the CO-IH transformation in Figure 23, they found that the energy barrier for this mechanism becomes prohibitively large for clusters with

https://doi.org/10.1021/acs.chemrev.2c00831
Chem. Rev. XXXX, XXX, XXX−XXX

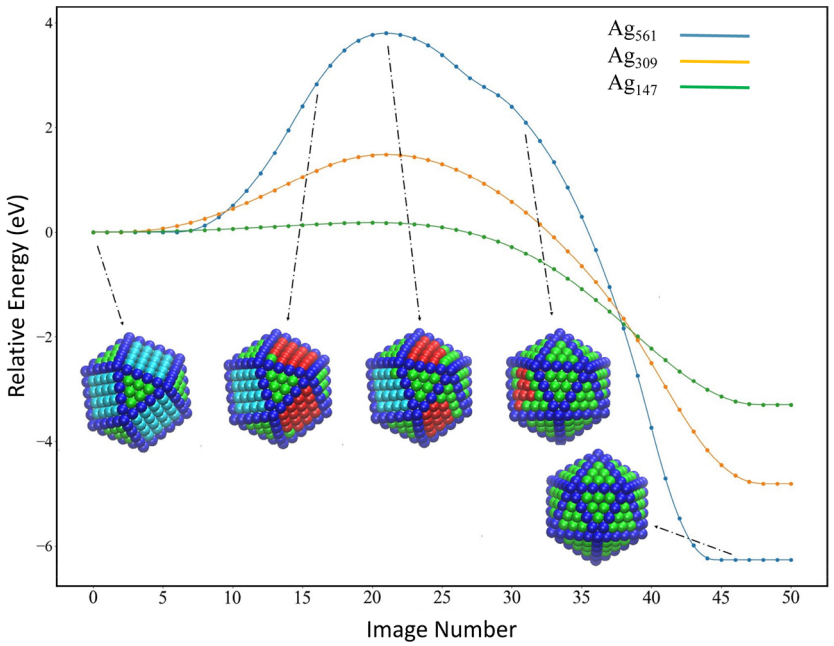

Figure 23. Minimum-energy pathways for Ag CO of three different sizes (561, 309, and 147 atoms) to transform to Ih via the DSD mechanism. Representative shapes are shown at various points along the pathway for Ag_{561}. Atoms in {111} facets are green, {100} are aqua, edge and corner atoms are dark blue, and strained surface atoms are red. The energy barriers for the transformation are 3.80, 1.48, and 0.18 eV for Ag_{561}, Ag_{309}, and Ag_{147}, respectively. Reproduced with permission from ref 120. Copyright 2021 American Chemical Society.

more than 147 atoms at typical experimental temperatures. Figure 23 also illustrates more details of the mechanism as well as aspects of CI-NEB calculations.

Regarding NEB calculations, one begins with a series of images of initial guesses of nanocrystal configurations along the pathway from the initial state (a minimum in potential energy) to the final state, another potential-energy minimum. Various algorithms can be used to converge this initial guess pathway to the final pathway—the minimum-energy pathway (MEP), which satisfies the condition

$$-\{\nabla E(\hat{R}_i) - [\nabla E(\hat{R}_i)\cdot\hat{\tau}_i]\hat{\tau}_i\} + \hat{F}_i^s = 0 \tag{19}$$

Here, $\nabla E(\hat{R}_i)$ is the gradient in the potential energy for image i with Cartesian coordinates $\hat{R}_i$, $\hat{\tau}_i$ is a unit vector that is tangent to the pathway at image i, and $\hat{F}_i^s$ is a spring force, that keeps the images evenly distributed along the pathway. The spring force has the form

$$\hat{F}_i^s = k(|\hat{R}_{i+1} - \hat{R}_i| - |\hat{R}_i - \hat{R}_{i-1}|)\hat{\tau}_i \tag{20}$$

where k is a constant. Thus, when the images are evenly spaced, the spring force becomes zero. When eqs 19 and 20 are satisfied for each image along a pathway between an initial and final state, the potential energy is minimized orthogonal to the pathway, but not along it. In the climbing-image form of the NEB method, the CI-NEB method,[185] an extra criterion is added to ensure that the image with the maximum potential energy, with coordinates of $\hat{R}_{max}$, is located at a transition state. The transition state is a first-order saddle point where the gradient in potential energy (the force) is zero and the potential energy is minimized along all directions except along the MEP (the Hessian matrix has one negative eigenvalue). This maximum-energy image is moved "uphill" along the MEP until its force $\hat{F}_{max}$ satisfies the criterion

$$\hat{F}_{max} = -\nabla E(\hat{R}_{max}) + 2[\nabla E(\hat{R}_{max})\cdot\hat{\tau}_{max}]\hat{\tau}_{max} = 0 \tag{21}$$

Then, the energy barrier for the transition [E_b in eq 18] can be obtained from the difference between the potential energies of the transition state (maximum-energy image along the minimum-energy pathway) and the initial minimum. All the minimum-energy pathways shown in Figure 23 satisfy eq 19 for each image (each point on the curve), while the transition state also satisfies eq 21. The MEP provides a caricature of the kinetic mechanism of a rate process. From the sequence of images shown in Figure 23, we see that atoms on the {100} facets of CO become strained as these facets twist to become {111} facets.

Rossi and colleagues used meta-dynamics[267] to characterize the DSD transitions of Cu, Ag, Au, Ni, Pd, and Pt described by the RGL potential.[170] They found that DSD transitions occur below a material dependent critical size, and they did not achieve successful transitions above this size. Plessow used MD simulations with umbrella integration[268] based on the Gupta potential,[178] as well as DFT calculations with the CI-NEB method to characterize DSD transitions of Ag, Au, Cu, Ni, Pd, Pt, Rh, and Ir. They found that Cu, Ag, Au, and Ni clusters with sizes of up to 309 atoms possess low barriers for concerted transitions. In contrast, Pd, Pt, Rh, and Ir possess higher transition barriers, even at a size of 147 atoms. They found the material-dependence of the transition can be correlated with the melting point of the bulk metals.

While there has been significant emphasis on structural transformations via DS transition processes, it should be noted that other types of transitions can occur. For example, Huang et al. used massively parallel accelerated MD simulations based on the ParSplice[269] version of parallel replica dynamics[270] to study the structural transformations of Pt, Ag, Cu, and Ag nanoclusters described by EAM potentials.[249,271,272] They studied nanocrystals ranging from 146 to 231 atoms in size at

https://doi.org/10.1021/acs.chemrev.2c00831
Chem. Rev. XXXX, XXX, XXX−XXX

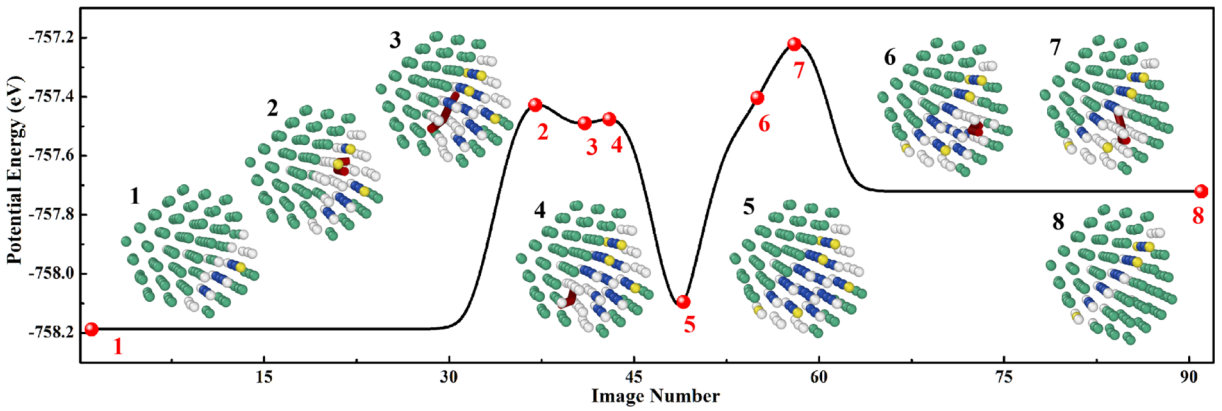

Figure 24. Minimum energy pathway for the creation of a twin boundary through nucleation and propagation of two 1/6⟨211⟩ partial dislocations. A stacking fault is initially present close to one of the surfaces of the nanocluster (image 1). A second fault then forms on a neighboring {111} plane, through the nucleation and propagation of a 1/6⟨211⟩ partial dislocations (shown in red), creating an extended {111} faulted region (seen in snapshots 1−5). The dislocation-mediated slip process then repeats along the original stacking fault, creating a centered twin boundary (seen in snapshots 5−8). Colors denote atomic types determined by the CNA analysis: green, fcc atoms; blue, hexagonal close-packed (hcp) atoms; yellow, icosahedral atoms; white, other. Reproduced with permission from ref 273. Copyright 2018 by the American Physical Society.

temperatures below melting. From trajectories of up to millisecond times, they observed a variety of direct transformations between fcc, Dh, and Ih structures that followed either slip-mediated twinning or surface-reconstruction mechanisms. Many of these transformations required tens of microseconds. One example transformation is shown in Figure 24. Beginning with a sequence of snapshots from one of the trajectories, they used the CI-NEB method to quantify a mechanism for obtaining a singly twinned structure from an initial structure containing a stacking fault.

Studies have also probed the influence of deposition on the structural transitions of monometallic clusters.[262,274−278] One of the earliest such studies was performed by Baletto, Mottet, and Ferrando.[274] They used MD simulations based on the RGL potential[170] to study the growth of small Ag seed crystals containing up to 150 atoms. For such small clusters, they could reach simulation times in the μs range, a range comparable to experimental studies of cluster growth in an inert gas aggregation source.[279−281] When the seed sizes were less than 100 atoms, they always achieved a minimum-energy shape (either an Ih or a Dh) as growth proceeded. However, for seeds with 150 atoms, the growth morphology was dependent on the deposition rate and temperature. For a fixed deposition rate, they obtained Ih at low and high temperatures, but they achieved Dh at intermediate temperatures. Although the Dh were metastable, they persisted for long enough times that they could be observed in experiment. These results agreed with experiments[279−281] and indicated that small nanocrystals with sizes in the 1−2 nm range could be kinetic structures.

Tal, Münger, and Abrikosov used direct MD simulations to investigate the mechanism of the Dh → Ih transition in Cu_{147} nanocrystals described using an EAM potential.[169] They showed that inhomogeneous deposition of atoms, due to fluctuations, leads to island formation on certain crystal facets of an Ih and distortion of the nanocrystal. This distortion shifts the energy balance between Ih and Dh phases in favor of the Dh, when the perfect Ih is thermodynamically more stable. Consistent with this explanation, they showed that fast diffusion suppressed the morphology transition and favored homogeneous growth of the nanoclusters. They also quantified the mechanism of the transition to be a concerted DS mechanism.

Recently, Xia et al. used MD simulations to probe the experimentally observed transition of Pt octahedra to tetrahedra as atoms are deposited on an initial Pt seed in a vacuum environment.[278] They proposed a complex mechanism for this transformation, shown in Figure 25. Figure 25a provides an overview of the mechanism, in which a TO (white atoms) becomes an octahedron after growth on all {100} facets to complete six vertices (blue atoms). Adding atoms to four {111} facets, a tetrahedron is obtained with four tips colored yellow, green, cyan and orange. Figure 25b−g shows a sequence of snapshots from a growth simulation at 400 K with a deposition rate of 0.1 atom/ns. The simulation commences from a truncated octahedron of 201 atoms (white atoms). Figure 25b shows a snapshot of when the octahedral vertices are completed. Figure 25c depicts non-neighboring growing (G, in yellow and green) facets, separated by nongrowing facets (NG) that initiate when the size has increased to 360 atoms. Also highlighted in black rectangles are small tetrahedral edges that form. In Figure 25d, we see that a stacking fault (F, in dark gray) forms at the corner between G and NG facets, creating {100}-like four-fold sites (enclosed in the pink rectangle). Deposited atoms adsorb on these sites, as shown in Figure 25e, and facilitate the growth of the tetrahedral tips by a self-replicating process, seen in Figure 25f, which finally leads to a tetrahedral nanoparticle at 560 atoms (Figure 25g), that continues to grow as a tetrahedron. This complex mechanism agreed with experiment.

Konuk and Durukanoglu used direct MD simulations to probe the shape evolution of truncated Ag nanocubes with Ag atoms deposited directly on the truncated facets.[276] As shown in Figure 26, they could achieve a variety of shapes over the MD time scale by varying the deposition time interval ϕ. These include an octopod (Figure 26a) with a deposition time interval of ϕ = 30 ps, a concave cube (Figure 26b) with ϕ = 100 ps, (c) a truncated cube (Figure 26c) with ϕ = 150 ps, and a cuboctahedron (Figure 26d) with ϕ = 500 ps, which is regarded to be a thermodynamic shape. These simulations indicate possible growth mechanisms for branched nanocrystals, such as those in Figure 5.

Studies have considered the role of a solution environment in promoting certain growth shapes and perhaps the first such study was conducted by Grochola, Snook, and Russo.[282] They

https://doi.org/10.1021/acs.chemrev.2c00831
Chem. Rev. XXXX, XXX, XXX−XXX

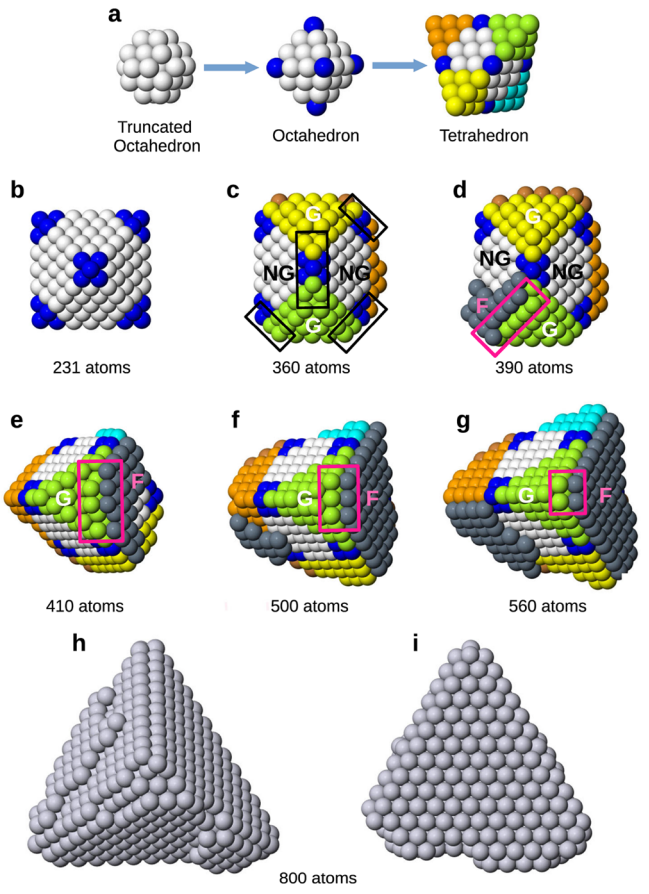

Figure 25. (a) Overview of the mechanism for conversion of a TO to a tetrahedron from the work of Xia et al.[278] (b–g) Shapes at various stages of growth (indicated by the size in number of atoms) as the octahedron transforms to a tetrahedron. The mechanism in b–g is discussed in the text. Reproduced with permission from ref 278. Creative Commons license https://creativecommons.org/licenses/by/4.0/.

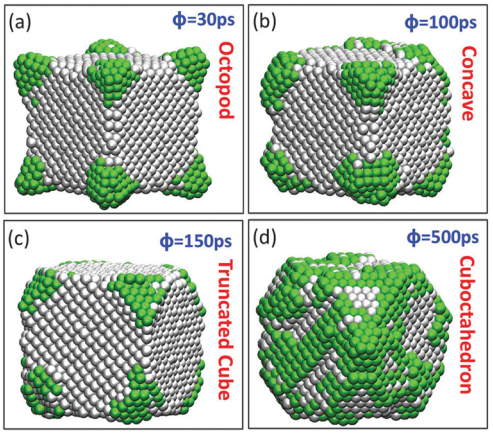

Figure 26. Four specific growth modes of the Ag nanocluster from simulations at 500, discussed in the text. The gray atoms are those in the initial Ag cube, while the deposited atoms are shown in green. Reproduced from ref 276 with permission from the PCCP Owner Societies.

used MD simulations based on their EAM potential[272] for Au to study the growth of gold nanorod morphologies from initial spherical seeds in the presence of model surfactant. Solvent molecules were not included in this model. A key feature for the growth of Au nanorods was their model surfactant, which contained interactions with Au based on an EAM-like term that allowed for facet-selective binding on the more open facets of Au (e.g., {110} and {100} were favored over {111}). Another important feature was attractive interactions between surfactants, which allowed for dense surfactant grouping on preferred facets. Their model reproduced the growth of nearly all known experimental nanorod morphologies when starting from an initial fcc or Dh seed, and it also reproduced the experimentally observed failure of nanorod growth from initial nanoparticles that were Ih or singly twinned.

Meena and Sulpizi conducted a series of MD investigations of the cetyltrimethylammonium bromide (CTAB)-mediated growth of Au nanorods.[283−285] Their studies went further than the study of Grochola et al.,[282] in that they employed all-atom models for CTAB and aqueous solvent, as shown in Figure 27a. They simulated the growth of penta-twinned Au seeds in the nanometer size range and found a dramatic symmetry breaking occurs as the CTAB surfactant layer preferentially covers the {100} and {110} side facets, leaving the {111} end facets unprotected, as shown in Figure 27b. This asymmetry of CTAB adsorption could then lead to the growth of Au nanorods.[283]

3.2. Atomistic Studies of Nanocrystal Kinetics with Kinetic Monte Carlo

The studies of nanocrystal growth discussed above rely on MD simulations, which are limited in the length and time scales they can probe. Moreover, no MD simulation to date has included the full solution-phase environment, with all relevant ions and reduction chemistry. With the realization that the solution-phase environment in nanocrystal synthesis is exceedingly complex, too complex for a fully quantum description or an accurate description with classical MD simulations, several studies have relied on kinetic Monte Carlo (kMC) methods to predict the influence of various kinetic phenomena on nanocrystal shapes. In kMC simulations,[286] a nanocrystal is represented as a lattice of sites and all the kinetic processes deemed relevant for nanocrystal evolution are defined. At step n, the system is in state A_n, where the state is defined by its configuration of atoms and the set of m transitions with transition rates $\{r_{i,n}\}$ to each of the neighboring states accessible in the $(n + 1)^{st}$ time step. The transition rates r_i typically have the form given in eq 18. A particular transition with a rate of r_i is chosen randomly based on a probability p_i given by

$$p_i = \frac{r_i}{\sum_j r_j} \tag{22}$$

where the sum in the denominator runs over all m possible transitions. The transition is executed by moving the appropriate atoms and updating time with an increment given by

$$\Delta t = -\frac{\ln(\text{rand})}{\sum_j r_j} \tag{23}$$

where *rand* is a uniform random number between 0 and 1. The list of transition rates is updated, and the above steps are repeated many times to simulate evolution of the system. The kMC description can be just as accurate as *ab initio* MD if a complete set of rate processes is included. However, solution-phase syntheses are sufficiently complicated that even first-

https://doi.org/10.1021/acs.chemrev.2c00831
Chem. Rev. XXXX, XXX, XXX−XXX

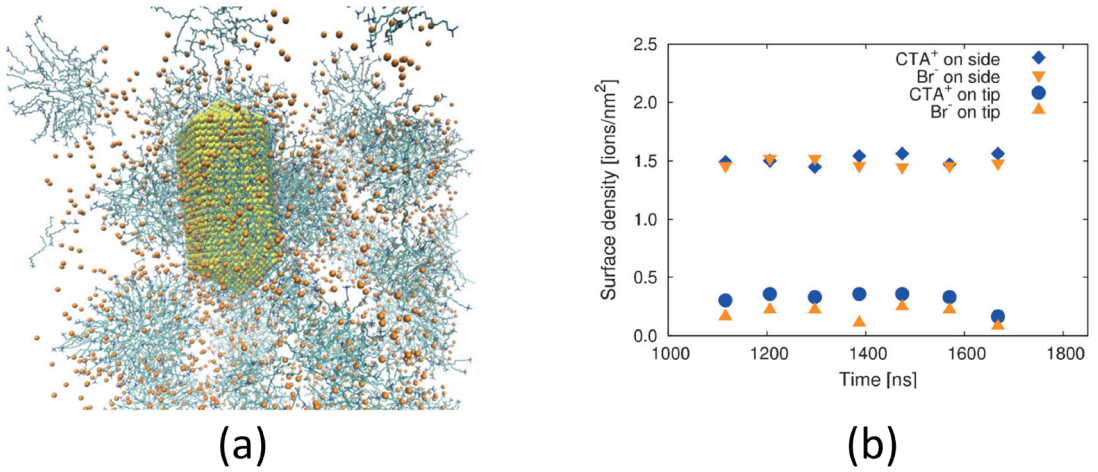

Figure 27. (a) Snapshot of a simulated penta-twinned nanorod (after 1668 ns) in CTAB solution (water molecules omitted for clarity). (b) Surface densities on the lateral sides and tips of the nanorod as a function of time. Reproduced with permission from ref 283. Copyright 2016 Wiley.

principles-based calculations cannot cover all aspects. Indeed, successes in most of the calculations discussed above and below are linked to the ability of a research team to identify the key phenomena in the synthesis. Strengths of kMC for simulating nanocrystal growth in the solution phase include the capability of such simulations to reach human time scales while retaining atomistic details and the capability to test hypotheses by constructing various growth scenarios.

Turner and colleagues used kMC simulations to model the growth of Au nanocrystals in a solution environment.[287] They parametrized rate constants in their model by fitting to experimental nanoparticle growth curves, and they were able to describe small deviations of the nanoparticle shapes from sphericity. He et al. used kMC simulations to investigate the melting of Au nanocrystals. They incorporated environment-dependent diffusion barriers in their simulations and obtained good agreement with experiment.[288] Li et al. used kMC simulations to model the structural evolution of metastable hollow nanocrystals of Au, Pt, and Pd to solid nanoparticles over time scales ranging from seconds to years.[289] For each metal, they fit the nearest-neighbor bond energy ε to DFT surface energies using the broken bond model,[290] namely

$$\gamma_{\{hkl\}} = -\frac{1}{2} N_{hkl} \varepsilon \tag{24}$$

where $\gamma_{\{hkl\}}$ is the surface energy of a unit-cell {hkl} surface and N_{hkl} is the number of missing nearest-neighbor bonds when cutting the surface from the bulk. They employed the nearest-neighbor bond energy to describe the dependence of the diffusion energy barrier (E_b in eq 18) on the number of nearest neighbors to a surface atom. They found that a cubic Pt cubic nanocage evolves to a chamfer nanobox to a nanoframe to a solid nanoparticle. Based on their observations, they gained insight into the rational design of stable hollow nanocrystals.

Another example of the fruitful use of kMC simulations is in a series of studies by Lai, Evans, and co-workers.[134,291,292] They developed a kMC model for the reshaping and sintering of Ag, Au, and Pd nanocrystals based on surface diffusion, with surface diffusion barriers calculated using CI-NEB calculations based on DFT calculations with the PBE exchange-correlation functional.[292] To account for the dependence of surface diffusion on the local atomic environment surrounding each surface atom, they adopted a variant of a model used by Fichthorn et al.[293,294] In this model, the diffusion energy barrier for an atom to transit from site i, where the energy has a value of E_i, to site j with E_j is given by

$$E_{b,i\to j} = E_{b,0} + \frac{1}{2}(E_j - E_i) \tag{25}$$

where $E_{b,0}$ is the energy barrier for an isolated atom to diffuse on a bare crystal surface. The values of E_i and E_j were given by $E_{i(j)} = n_{i(j)}\,\phi_{eff}$, where $n_{i(j)}$ is the number of nearest neighbors to site $i(j)$ and ϕ_{eff} is the effective nearest-neighbor interaction. This model satisfies the detailed balance criterion, necessary for kinetics to evolve the system to thermodynamic equilibrium. Their model was successful at matching experimental sintering time scales[291] and nanocube truncation morphologies.[292]

In the kMC studies discussed above, the values of the preexponential factors for the rates in eq 18 were assumed to be constant, with values in the typical range of 10^{12}–10^{13} s^{-1}. However, the preexponential factors can be calculated and a typical approximation used for condensed-phase systems is the harmonic approximation.[295] In the harmonic approximation, we find the eigenvalues $\{\lambda_i\}$ of the Hessian matrix at both the initial state and the transition state, and we can obtain the normal-mode frequencies $\{\upsilon_i\}$ from the eigenvalues. The preexponential factor is then given by

$$A = \frac{\prod_{i=1}^{3N-6} \nu_i}{\prod_{i=1}^{3N-7} \nu_i'} \tag{26}$$

where υ_i and ν_i' are the normal-mode frequencies at the minimum (initial state) and the saddle point (transition state), respectively, and N is the number of atoms. There are $3N-6$ vibrational degrees of freedom at the minimum (subtracting translation and rigid-body rotation) and $3N-7$ at the saddle point because one of the frequencies is imaginary. For example, Wales and Munro used the harmonic approximation to calculate rates for the DSD transition, discussed above.[257]

In a final, more empirical use of kMC simulations, Hauwiller and co-workers imaged the oxidative etching of nanocrystals with well-defined initial shapes and a controlled redox environment using LPTEM.[296] Their study demonstrated how the shapes of initial Au rhombic dodecahedra and nanocubes evolved via oxidative etching of high-energy, under-

https://doi.org/10.1021/acs.chemrev.2c00831
Chem. Rev. XXXX, XXX, XXX−XXX

coordinated Au surface atoms. Their complementary kMC simulations showed that the experimentally observed tetrahexahedral shapes (see Figure 5) resulting from etching could evolve by the successive removal of edge and step atoms.

3.3. Kinetic Wulff Shapes

In a kinetic analog of surface-energy calculations, from which Wulff shapes can be predicted, it is possible to predict kinetic Wulff shapes. The linear growth rate of facet i G_i, or the accumulation rate of atoms on facet i, is important in the kinetic Wulff construction,[297,298] which takes the form

$$\frac{G_i}{h_i} = \lambda \tag{27}$$

where h_i is the length of the normal vector from the crystal center to facet i, and λ is a constant. Equation 27 is completely analogous to eq 5, where the surface energy γ_i in eq 5 is replaced by G_i. Thus, in Figure 20, Wulff shapes are shown for various ratios $\gamma_{111}/\gamma_{100}$ and G_{111}/G_{100}. Several studies have focused on predicting kinetic Wulff shapes.

Qin, Balankura, and Fichthorn investigated the flux of Ag atoms through PVP-covered Ag(100) and Ag(111) surfaces in EG solvent[299−301] using all-atom MD simulations based on their metal−organic many-body force-field.[250,299] The flux is the atom deposition rate per unit area, and it is proportional to the linear facet growth rate (G) if the surface diffusion of atoms between facets is negligible—as we expect for a sufficiently large nanocrystal. They calculated the flux of solution-phase atoms to the two surfaces using direct MD simulations,[300] as well as with MD simulations using umbrella integration.[299,301] Umbrella integration[268] is a variant of the umbrella sampling technique.[302] In this method, the reaction coordinate ξ is initially defined from a "pulling simulation", in which the system is biased to assume successive configurations between the initial and final states. Figure 28 shows a trajectory from an initial pulling simulation for the Ag-PVP-EG system, in which an Ag atom is brought from a configuration in the solution phase far from the PVP surface layer to a configuration in which it is bound to the Ag surface.

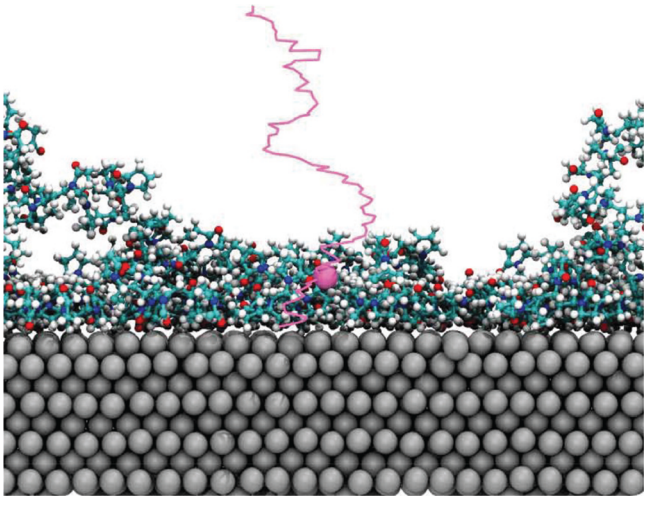

Figure 28. Trajectory of a solution-phase Ag atom (magenta) from an initial pulling simulation of the atom through the PVP layer covering an Ag facet. EG solvent molecules are not shown, for clarity. Used with permission of The Royal Society of Chemistry, from ref 299; permission conveyed through Copyright Clearance Center, Inc.

After obtaining an initial pulling trajectory, the reaction coordinate is divided into windows and the system is constrained to reside in each window with a bias potential. A typical form of the bias potential is the harmonic bias ω, given by

$$\omega(\xi) = \frac{K}{2}(\xi - \xi_0)^2 \tag{28}$$

where K is the force constant and ξ_0 is a reference point at the center of the window. A separate MD simulation is done for each window to sample the position of the reaction coordinate, and it is essential that there is overlap between the reaction-coordinate values sampled in successive windows. The potential of mean force (PMF) at ξ, $A(\xi)$, is related to the histogram of sampled values of ξ via

$$A(\xi) = -\frac{1}{\beta}\ln P_b(\xi) - \omega(\xi) + F \tag{29}$$

where $\beta = 1/k_BT$, $P_b(\xi)$ is the sampled probability distribution, and F is a lumped constant from terms that are independent of the reaction coordinate, although the value of F is unknown. In umbrella integration, the derivative of eq 29 is taken for each window i so the constant F vanishes and we have

$$\frac{dA_i}{d\xi} = \frac{1}{\beta}\frac{d\ln P_{b,i}(\xi)}{d\xi} - \frac{d\omega_i}{d\xi} \tag{30}$$

Substituting eq 28 for $\omega(\xi)$ and fitting $P_{b,i}(\xi)$ to a Gaussian distribution with a mean of $\bar{\xi}_{b,i}$ and a variance of ${\sigma_{b,i}}^2$, we have

$$\frac{dA_i}{d\xi} = \frac{1}{\beta}\frac{(\xi - \bar{\xi}_{b,i})}{\sigma^2_{b,i}} - K(\xi - \xi_{0,i}) \tag{31}$$

The values from different windows are combined to obtain $dA/d\xi$, which is then integrated to obtain the PMF. The mean first passage time t_m is obtained from the PMF via[303]

$$t_m(\xi, \xi_f) = \int_{\xi}^{\xi_f}\left\{\int_{\xi_0}^{\xi'}\exp[-\beta A(\xi'')]\,d\xi''\right\}\frac{\exp[\beta A(\xi')]}{D(\xi')}\,d\xi' \tag{32}$$

Here, $D(\xi')$ is the diffusion coefficient, which can be obtained in the same calculation used for the PMF.[304,305] If $\xi = \xi_0 = 0$, while A and D are constants independent of ξ, then eq 32 yields the one-dimensional Einstein equation $\xi_f^2 = 2Dt_m$.

The power of eq 32 is that it can account for features of the free-energy landscape that influence the deposition rate as a solution-phase species transits through a capping layer to the surface of a growing nanocrystal. For example, Figure 29 depicts the PMF associated with motion of an Ag atom through EG solvent and the PVP decamer layers on Ag(100) and Ag(111) depicted in Figure 28. There are several features of Figure 29 that are conducive to a more rapid flux of an Ag atom through the PVP layer on Ag(111) than on Ag(100). First, after maintaining a constant (zero value) far from the surfaces, the PMF begins to decrease, and it decreases for Ag(111) before it decreases for Ag(100). This reflects a more extensive and loosely bound PVP layer on Ag(111), which traps incoming Ag atoms more readily than Ag(100). After becoming ensnared in the PVP layer, the Ag atom moves toward the surface and becomes trapped in a free-energy minimum close to the surface. This minimum is deeper for Ag(100) and the barrier for the atom to advance from this minimum to the final minimum at the surface is larger. All

https://doi.org/10.1021/acs.chemrev.2c00831
Chem. Rev. XXXX, XXX, XXX−XXX

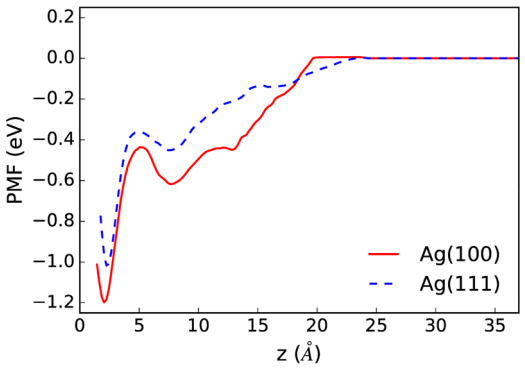

Figure 29. PMF for an Ag atom to diffuse from the EG solution phase through a layer of PVP decamers to Ag(100) (red, solid) and Ag(111) (blue, dashed). Reproduced with permission from ref 301. Copyright 2016 AIP Publishing.

these features lead to a shorter value of t_m for Ag(111) than Ag(100) and $G_{111} > G_{100}$. If surface diffusion between the facets is insignificant, $G_{\{111\}}/G_{\{100\}} = t_{m,\{100\}}/t_{m,\{111\}} = 3.47$ for PVP-covered Ag in EG solution. According to Figure 20, such shapes are cubes, consistent with experiment.[306,307]

Although the linear facet growth rate can be equated to the deposition rate if atom diffusion between facets or net nanocrystal rearrangement is negligible, this is not always the case. As was discussed above, wholescale nanocrystal transformations can occur over deposition time scales if the nanocrystal is sufficiently small. For larger nanocrystals, surface diffusion on the facets can occur on the time scale of deposition. Studies have considered this scenario.[308−311]

Qi and co-workers considered the growth of penta-twinned Ag nanowires mediated by surface diffusion.[308] They combined several different theoretical methods to predict growth morphologies of Ag nanowires from seeds. They used MD simulations based on an EAM potential for Ag[249] to obtain the detailed structure of a 28 nm decahedral Ag seed. As shown in Figure 30, the seed is a Marks Dh with {111} end facets and "notches", {100} side facets, and {110} facets between the "notches" and the ends.

From CI-NEB calculations of atom diffusion barriers on the various facets of the seed, they found diffusion was rapid in the {111} "notches", so the notches could rapidly channel atom transport from the {100} nanowire sides to the ends. They also found that strain could induce heterogeneous atom diffusion and aggregation on the {111} facets and lead to atom trapping at the nanowire ends. Figure 31 shows their calculated minimum-energy pathway for an Ag atom to diffuse from a {100} side to a {111} end via a {111} notch and intervening {110} facets.

Qi et al. included all their calculated diffusion rate constants into Mean First-Passage Time (MFPT) calculations based on the theory of absorbing Markov chains,[312−315] to obtain net interfacet diffusion times and their reciprocal interfacet diffusion rates $R_{100\rightarrow111}$ and $R_{111\rightarrow100}$. In the theory of absorbing Markov chains, time evolution is based on the Master equation, which is given by

$$\frac{d\vec{P}}{dt} = -\boldsymbol{A}\vec{P} \tag{33}$$

where $\vec{P} = \{P_i\}$ is the probability state i occurs at time t, and $\boldsymbol{A}$ is the transition-rate matrix, with

$$A_{ij} = \begin{cases} \sum_k r_{ik}, & \text{if } i = j \\ -r_{ji}, & \text{if } i \neq j \end{cases} \tag{34}$$

Here r_{ij} is the rate to transit from state i to j.

The theory of absorbing Markov chains can be applied to calculate the MFPT $\langle t_{i\rightarrow j}\rangle$, or the average time for an atom to transit from facet i to facet j. To calculate the MFPT, we convert the transition-rate matrix $\boldsymbol{A}$ into the Markov matrix $\boldsymbol{M}$ as follows. First, we define two types of states: transient states and absorbing states. In transient states, transitions can occur to other states, while absorbing states are final states, where no further transitions occur. There are N_A absorbing states and N_T transient states for a given nanocrystal geometry. Based on these two types of states, we define the Markov matrix $\boldsymbol{M}$ as

$$\boldsymbol{M} = \begin{pmatrix} \boldsymbol{I} & \boldsymbol{0} \\ \boldsymbol{R} & \boldsymbol{T} \end{pmatrix} \tag{35}$$

where $\boldsymbol{I}$ is an $N_A \times N_A$ identity matrix, $\boldsymbol{0}$ is an $N_A \times N_T$ null matrix, the reccurrent matrix $\boldsymbol{R}$ has dimensions of $N_T \times N_A$, and the transient matrix $\boldsymbol{T}$ has dimensions of $N_T \times N_T$. The recurrent matrix accounts for transitions between transient and absorbing states and the transient matrix contains the rates for transitons between transient states. The elements of the transient matrix are given by

$$T_{ij} = \begin{cases} 0, & \text{if } i = j \\ r_{ij}\tau_i, & \text{if } i \neq j \end{cases} \tag{36}$$

and the elements of the recurrent matrix are given by

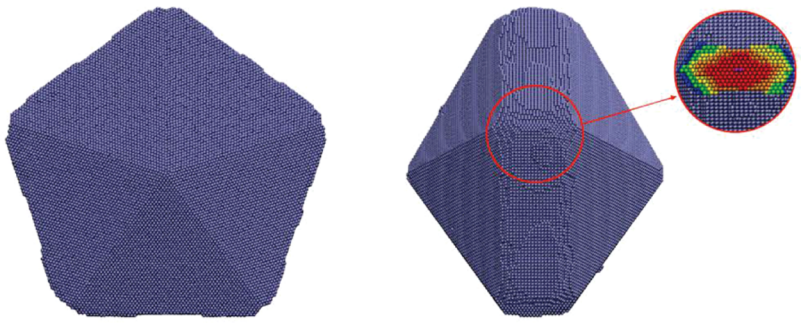

Figure 30. Front view (left) showing the five {111} facets of a penta-twinned Ag nanocrystal and side view (right) showing the {100} side facets, where {111} notches and {110} steps are shown in the magnified region such that atoms colored in red are the closest to the viewer and atoms in dark blue are the furthest away. Reproduced with permission from ref 308. Copyright 2019 American Chemical Society.

https://doi.org/10.1021/acs.chemrev.2c00831
Chem. Rev. XXXX, XXX, XXX−XXX

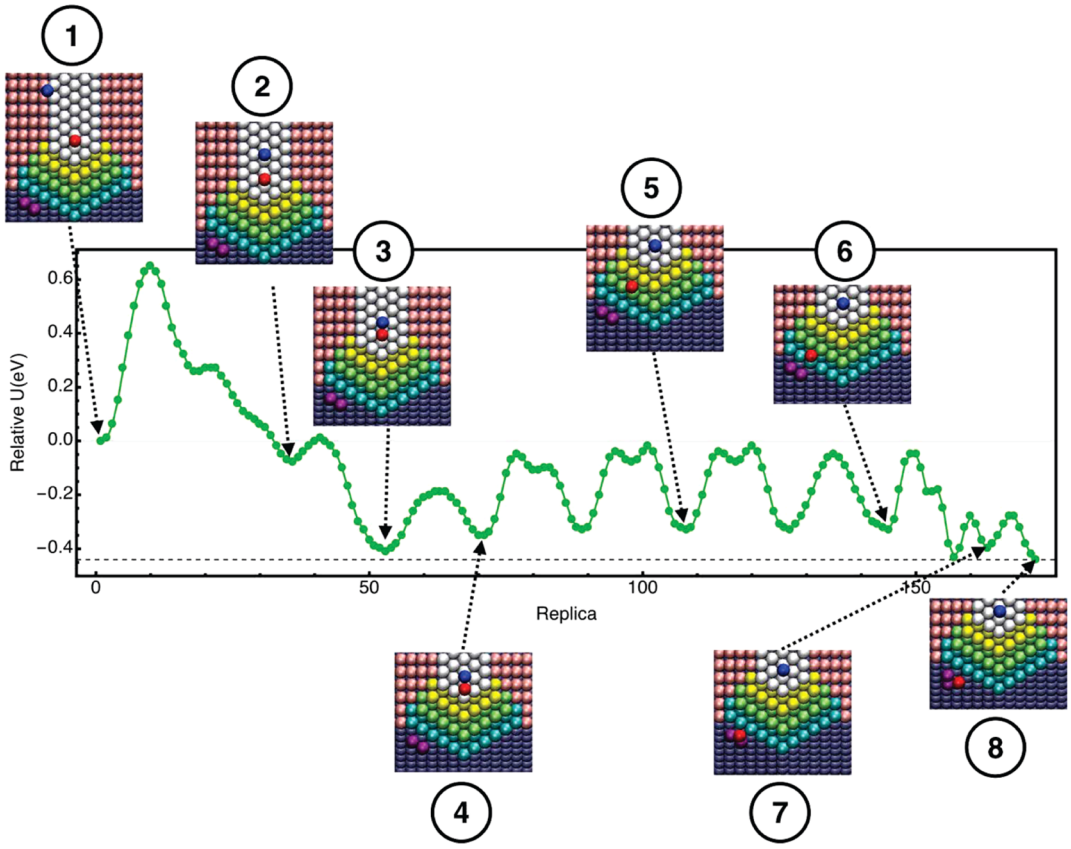

Figure 31. Minimum-energy pathway from CI-NEB calculations for diffusion of an Ag atom from the {100} side facet **1** to the {111} notch, where it joins another atom to form a dimer that diffuses in the notch to the edge of the {110} facet (**2**–**4**), dissociates from the dimer and diffuses on the {110} facet (**5**–**6**) to the {110}–{111} edge, where it joins a dimer on the {111} facet (**7**–**8**). Reproduced with permission from ref 308. Copyright 2019 American Chemical Society.

$$R_{ij} = r_{ij}\tau_i \tag{37}$$

where r_{ij} is an appropriate rate in $\boldsymbol{A}$ and $\tau_i = A_{ii}^{-1}$.

The MPFT and the exit probability distribution for various absorbing states $\vec{P}_{\text{exit}}$ can be obtained from

$$\left\langle t_{i\to j}\right\rangle = \vec{p}_0^{\,T}\cdot(\boldsymbol{I_T} - \boldsymbol{T})^{-1}\cdot\vec{\tau} \tag{38}$$

and

$$\vec{P}_{\text{exit}} = \vec{p}_0^{\,T}\cdot(\boldsymbol{I_T} - \boldsymbol{T})^{-1}\cdot\boldsymbol{R} \tag{39}$$

where $\vec{p}_0^{\,T}$ is the initial probability that the transient states are occupied and $\boldsymbol{I_T}$ is an identity matrix with the same dimensions as $\boldsymbol{T}$.

In the theory of absorbing Markov chains, it is necessary to enumerate every state of the system, along with all rates to transit from one state to another. This is possible in the dilute limit of a single atom diffusing on a facet because the number of states is equal to the number of atomic binding sites on the facet and is, thus, limited to tractable numbers for nano-objects. As the number of atoms on a facet increases, the number of possible configurations (states) increases dramatically, and this approach becomes intractable. As an aside, kMC simulations, discussed above, are also a numerical solution to the Master equation and they retain the advantage that not every state has to be enumerated to obtain an exact solution, although all the rates must be defined.

Using MFPTs from the theory of absorbing Markov chains, Qi et al. calculated linear facet growth rates using

$$G_{100} = \frac{\mathrm{d}N_{100}}{\mathrm{d}t} = R_{\text{dep},100} + R_{111\to100} - R_{100\to111} \tag{40}$$

and

$$G_{111} = \frac{\mathrm{d}N_{111}}{\mathrm{d}t} = R_{\text{dep},111} + R_{100\to111} - R_{111\to100} \tag{41}$$

where $R_{\text{dep},\,i}$ is the deposition rate on facet i and $R_{i\to j} = \langle t_{i\to j}\rangle^{-1}$. $R_{100\to111}$ is dependent on the length of the nanowire and decreases with increasing nanowire length, while $R_{111\to100}$ is a constant for a nanowire with a fixed diameter. From their calculations for a seed with a 28 nm diameter, they found for a range of nanowire lengths that

$$R_{100\to111} \geq R_{\text{dep}} \gg R_{111\to100} \tag{42}$$

where $R_{\text{dep}} = R_{\text{dep},100} + R_{\text{dep},111}$. This leads to the condition where $G_{100} \approx 0$ and $G_{111} = R_{\text{dep}}$. In other words, there is a range of nanowire lengths for which all the deposited atoms are channeled to the nanowire ends. This situation has been observed in experimental studies of the growth of capped Ag nanowires where Ag nanowires maintained a constant diameter for 35 min, while they grew to achieve an aspect ratio of around 1000.[316] Subsequently, the wire diameters increased. It should be noted that not all experimental studies report such a detailed analysis of growth trajectories. For the 28 nm diameter seed shown in Figure 30, Qi et al. predicted that nanowires could attain aspects ratios ranging from 70 to 340, consistent with experimental results for nanowire growth in the absence of capping agents.

https://doi.org/10.1021/acs.chemrev.2c00831
Chem. Rev. XXXX, XXX, XXX−XXX

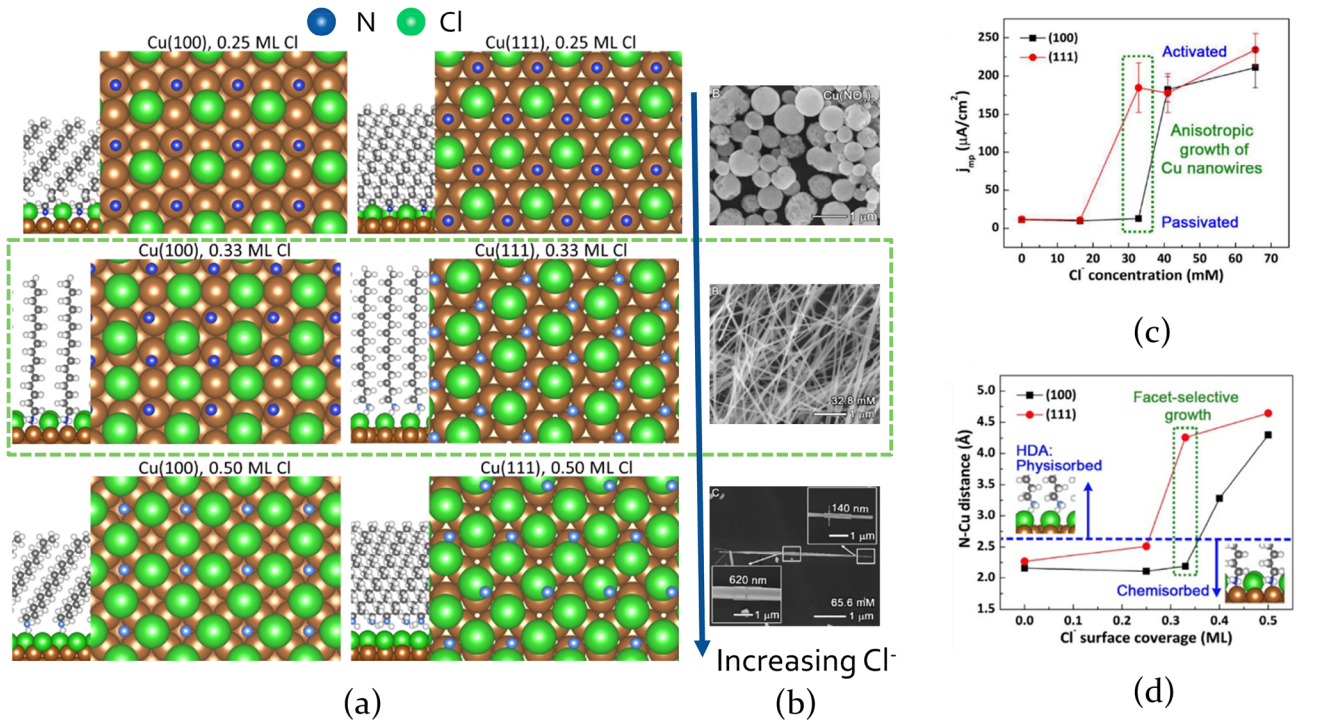

Figure 32. (a) Side and top-down views (showing only the N atom and Cl atoms) from DFT calculations of HDA and Cl adsorbed on Cu(100) and Cu(111) at three different coverages. (b) TEM micrographs of synthesized nanostructures with increasing chloride concentration. (c) Current density at the mixed potential as a function of solution-phase chloride concentration from electrochemical experiments. (d) Distance between the N in the amine and the Cu surface as a function of Cl surface coverage. Reproduced with permission from ref 321. Copyright 2018 American Chemical Society.

Kim and Fichthorn applied a similar approach to the growth of Cu microplates mediated by iodide.[310] Experimentally, Cu microplates were grown in water, using hexadecylamine (HDA) as a capping agent and with NaI as an additive.[152] The plates have large {111} facets with dimensions in the micrometer range and a mixture of {111}, {100}, and likely higher index side facets with dimensions of around 100 nm. *Ab initio* thermodynamics calculations indicated the plates contained only adsorbed iodine, with no adsorbed HDA under the experimental synthesis conditions.[152]

In the absence of a strong deposition bias onto the side facets, Kim and Fichthorn conducted a theoretical study to investigate if surface diffusion could explain the large dimensions of the basal {111} facets. They used DFT to quantify the binding and diffusion (via the CI-NEB method) of Cu atoms on I-covered Cu(111) and Cu(100) surfaces, as well as on I-covered interfacet slabs containing both {100} and {111} facets. Their calculations indicated that iodine adsorption leads to strong Cu atom binding and prohibitively slow diffusion of Cu atoms on Cu(100), a feature that promotes Cu atom accumulation on the {100} site facets of a growing 2D plate.

Using absorbing Markov chain calculations, they predicted plates can grow to achieve lateral dimensions in the 1−10 μm range, as observed in experiments, due to fast {111} surface diffusion. Their calculations confirmed that I adsorption promotes another necessary feature for plate growth: stacking faults. Studies have shown that plates can only form when fcc metals contain two or more stacking faults.[317−319] Their calculations showed that Cu atoms bind slightly more strongly to hcp hollow sites than fcc hollow sites on iodine-covered Cu(111). This feature promotes the formation of stacking faults, which, in turn, promote 2D growth.

DFT studies have been employed to infer the origins of kinetic shapes in experiments. For example, Liao et al. used liquid phase TEM to image the growth of platinum nanocubes capped with oleylamine.[320] From movies of evolving Pt particles, they tracked the growth rates of the {111}, {011}, and {100} facets as a function of time and noted that the growth of the {100} facets eventually ceased, leading to nanocube formation. To understand these results, they performed DFT calculations to resolve the binding of oleylamine capping molecule to Pt(100) and Pt(111). Their calculations indicated that the low mobility of oleylamine on Pt(100) relative to Pt(111) could impede the addition of solution-phase Pt species to the Pt(100) surface relative to Pt(111), leading to the growth of cubes.

Another notable example is in the synthesis of aqueous, penta-twinned Cu nanowires from $CuCl_2$ salt in the presence of HDA.[213,321] A combination of synthesis and electrochemical experiments showed disruption of alkylamine monolayers by chloride ions causes facet-selective Cu deposition that modulated the shape of the resulting Cu nanomaterials.[321] *Ab initio* thermodynamics calculations based on DFT[213,321] showed that at relatively low chloride solution-phase concentrations (chemical potentials), both {100} and {111} facets contained chemically adsorbed HDA self-assembled monolayers and spherical nanoparticles were synthesized experimentally, as shown in the top panels of Figure 32a,b.

As the chloride concentration increased, there was a regime where Cu(100) contained chemisorbed HDA, but Cu(111) had weakly physisorbed HDA, consistent with the synthesis of Cu nanowires, shown in the middle panels of parts a and b of

https://doi.org/10.1021/acs.chemrev.2c00831
Chem. Rev. XXXX, XXX, XXX−XXX

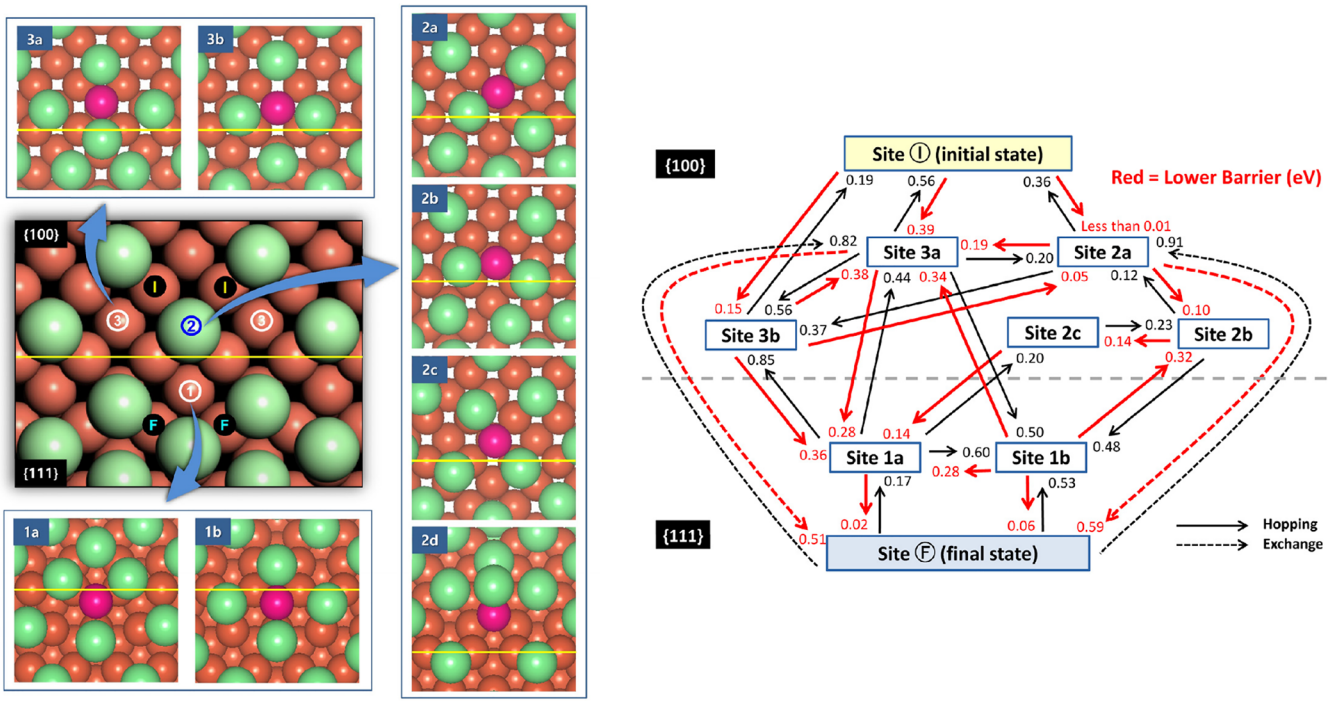

Figure 33. (left) Binding sites for Cu atoms near the {100}−{111} facet edge, where the Cu substrate is copper colored, Cl is green, and the Cu adatom is magenta. Cu atoms bound at the same location with respect to the underlying Cu surface can have various arrangements of Cl atoms surrounding them. (right) Kinetic network for adatom hopping from an initial site I on the {100} facet to a final state F on the {111} facet. CI-NEB energy barriers (in eV) are shown for the forward and reverse hops between various states. The direction with the lower energy barrier is shown in red. Solid arrows denote adatom hopping over the top of the surface and dashed arrows denote exchange of the Cu atom with Cu surface atoms. Reproduced with permission from ref 309. Copyright 2021 American Chemical Society.

Figure 32. At the highest solution-phase chloride concentrations, where experiments observed javelin-shaped structures, DFT calculations indicated both surfaces contained adsorbed chlorine with weakly physisorbed HDA, as seen in the bottom panels of a and b of Figure 32.

The DFT calculations were also consistent with electrochemical experiments (see Figure 32c), which showed the Cu reduction (deposition) rates were low on both Cu(100) and Cu(111) at low solution-phase chloride concentrations, where spherical particles form in the top panel of Figure 32b. As the concentration of solution-phase chloride increased, they found an intermediate concentration range, in which the electrochemically determined deposition rate was high on Cu(111) but low on Cu(100) and penta-twinned Cu nanowires were formed with high aspect ratios, as shown in the middle panel of Figure 32b. At still higher solution-phase concentrations of chloride, the deposition rate indicated by Figure 32c was high on both {100} and {111} facets and Cu wire-like structures were formed with javelin shapes in Figure 32b. The distance between the N in the amine group and the Cu surface is indicative of physisorption or chemisorption of HDA and is shown as a function of Cu surface coverage in Figure 32d. Here it can be seen that this distance correlates well with the electrochemical curves in Figure 32c.

Although DFT calculations and experiments presented a driving force for nanowire growth via deposition on the ends of the wires, the experimental studies indicated the ratio of deposition rates on the ends vs the sides was not sufficient to produce nanowires with the experimental aspect ratios.[321] Further DFT studies of the Cu−Cl−HDA system revealed that Cu atoms on chlorinated Cu(111) bind more strongly and diffuse more slowly than on chlorinated Cu(100), a reversal of the trend for bare Cu surfaces.[309] Additionally, these studies probed interfacet diffusion and showed this proceeds faster from Cu(100) to Cu(111) than the reverse.

Figure 33 depicts various binding configurations for Cu atoms near the edge of a Cu{100}-Cu{111} facet edge. Using the CI-NEB method, they calculated diffusion energy barriers for transitions between the various sites and obtained the kinetic network shown in the left panel of Figure 33. By adopting an approach like that of Qi et al.,[308] outlined above in eqs 33−41, they predicted nanowire aspect ratios of around 100, better than the aspect ratio predicted by deposition only but still below experiment. By including the combined effects of deposition and surface diffusion, they were able to predict nanowire aspect ratios between 10^2 and 10^5 in the range of experiments.[322−324]

In addition to facet-selective diffusion and deposition induced by capping agents, a joint experimental-theoretical study showed that facet-selective reduction kinetics could underlie the solution-phase growth of Pd nanocubes and penta-twinned nanowires induced by bromide and formic acid in solution.[311] Mastronardi et al. used DFT-based *ab initio* thermodynamics to show there is a synergy between the adsorption of Br and COOH, a decomposition product of formic acid on Pd(111) and Pd(100). The calculations predicted that {100} facets contained a mixture of Br and COOH, or just COOH, while {111} facets contained no COOH at high Br and formic acid concentrations, consistent with experimental conditions under which Pd cubes and penta-twinned nanowires formed.

Finally, Wang and co-workers designed "bent" capping molecules with unique binding affinities for nanocrystal corner, edge, and facet sites.[325] As shown in Figure 34, they employed

https://doi.org/10.1021/acs.chemrev.2c00831
Chem. Rev. XXXX, XXX, XXX−XXX

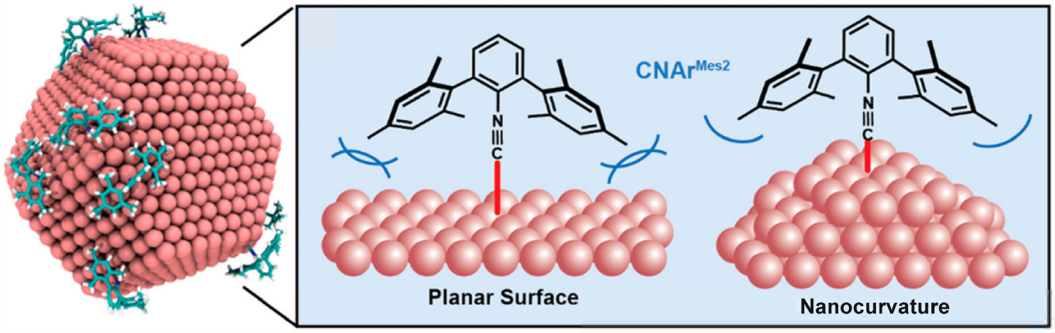

Figure 34. (left) Computational model of *m*-terphenyl isocyanide ligands binding to an Au nanocrystal, where Au(100) and Au(111) surface facets generate planar, edge, and corner sites. (right) Schematic of *m*-terphenyl isocyanide ($CNAr^{Mes2}$) selectivity for high-curvature surface binding sites due to the molecular topology of the ligand anchoring group. Reproduced with permission from ref 325. Copyright 2022 American Chemical Society.

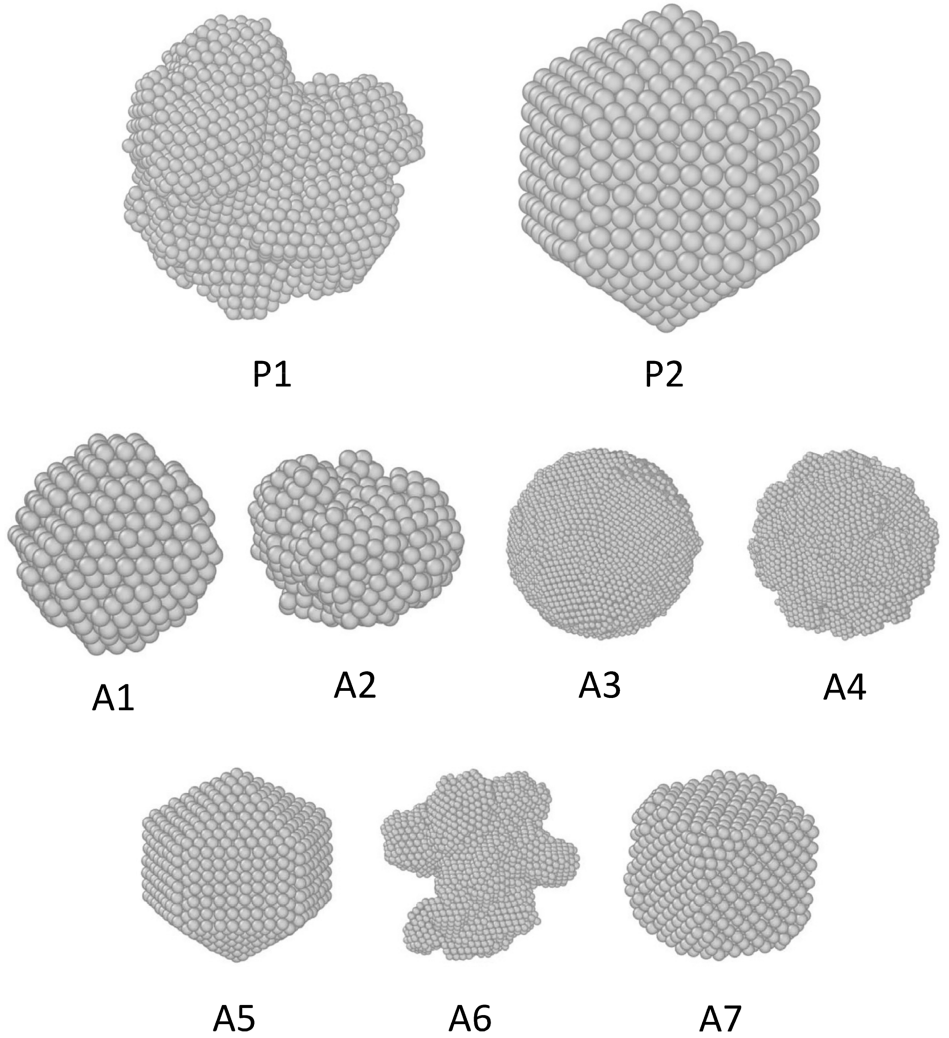

Figure 35. Best-matched nanoparticle shapes determined by ILS to prototype 1 (P1) and prototype 2 (P2), archetype 1 (A1), archetype 2 (A2), archetype 3 (A3), archetype 4 (A4), archetype 5 (A5), archetype 6 (A6), and archetype 7 (A7). Reproduced with permission from ref 331. Copyright 2021 Institute of Physics.

m-terphenyl isocyanide ligand $CNAr^{Mes2}$, which has a bent structure that conforms more easily to curved surfaces or edges than it does to perfect flat facets. In both experiments and theory, they demonstrated that these ligands bind selectively to regions of higher curvature, such as nanocrystal edges. Presumably, such ligands will provide protection of nanocrystal edges, so that novel kinetic shapes can be formed with deposition occurring on the more open facets. However, it remains to be seen whether these ligands can promote novel nanocrystal shapes.

https://doi.org/10.1021/acs.chemrev.2c00831
Chem. Rev. XXXX, XXX, XXX−XXX

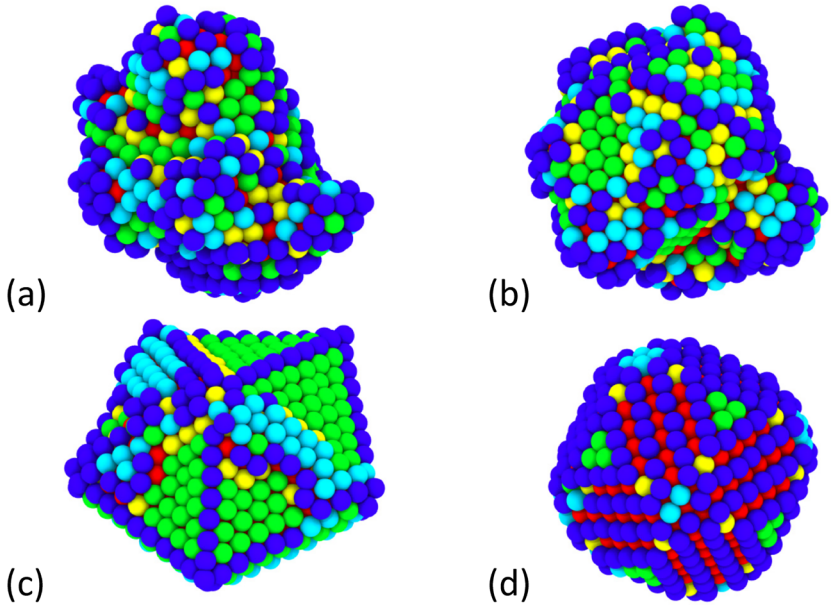

Figure 36. Example Pt nanoparticles in class 1 with high concentrations of (a) surface microstructures and (b) surface facets. Class 2 with high concentrations of (c) surface microstructures, and (d) surface facets. Dark-blue atoms have a coordination number of 7, light blue 8, green 9, yellow 10, and red 11. Reproduced with permission from ref 333. Copyright 2020 AIP Publishing.

4. MACHINE LEARNING

Machine learning has become pervasive in today's research climate, including in the theory of nanomaterials. Below, I will highlight three ways in which machine learning has been used in conjunction with predicting or classifying nanocrystal shapes.

Above, I discussed that predicting the shapes of nanomaterials can be a complex, multiscale enterprise. The use of empirical potentials, or force fields, can facilitate the understanding of nanomaterial shapes considerably. However, for an empirical potential to be effective, it needs to be accurate. Machine learning has been employed to develop the newest generation of force fields with high fidelity to quantum mechanics. Zeni and colleagues recently wrote a review of the application of machine learning to developing force fields to predict the structures of metal clusters.[326] A few groups have developed machine-learning-based force fields for Au. Perhaps one of the earliest applications of machine learning in this area was by Ouyang et al., who developed a neural network potential for Au trained by DFT.[327] They applied this potential to search for minima of Au nanoclusters using basin hopping, and they identified a new structure for Au_{58}. Like the Au clusters in the studies discussed above,[147,160,194] this was a core−shell structure.

Jindal and Bulusu applied artificial neural networks to fit empirical potentials for Au nanoparticles from DFT data.[160] As discussed above, they were able to predict Au nanoparticle shapes with high fidelity to DFT[147] and comparable to the structures predicted in DFTB simulations.[194] Thorn et al. developed a neural network potential for Au and compared it to Gupta and EAM potentials in their fidelity to DFT calculations with the PBE exchange-correlation functional.[177] They found that the neural network potential had the best agreement with DFT. Zeni et al. developed two machine learning force fields for Au nanoparticles based on DFT calculations with both the LDA and rPBE[328] exchange-correlation functionals. They used these two force fields in MD to simulate the size-dependent melting of Au nanocrystals and obtained good agreement with experiment. They also simulated melting using the RGL potential and found the simulated temperatures to be low compared to experiment.

Machine learning is also a promising tool to identify various nanocrystal structural motifs. The shapes of small fcc nanocrystals are typically quantified in terms of perfect crystals, as shown in Figure 7: TO, Ih, Dh, etc., but such shapes only arise for certain "magic numbers" of atoms that give the crystal a perfect shape. Methods in machine learning, such as *k*-means clustering, principal component analysis, and archetypal analysis are powerful tools to identify intrinsic patterns in materials science, including patterns that arise in geometrically imperfect shapes, as reviewed by Fernandez and Barnard.[329] These methods rely on structural descriptors, for example, Zhang and Barnard recently used machine learning to classify the structures of 4000 Au nanoparticles using two different sets of descriptors based on atomic and cluster information.[330] They employed more than 60 different atomic descriptors, including the fractions of bulk and surface atoms, the minimum and maximum nanoparticle radii, the fraction of atoms on various surfaces, the fraction of atoms with various coordination numbers, and more than 60 cluster descriptors, including various order parameters, bond lengths, and fraction of fcc atoms. They employed both unsupervised and supervised learning methods to classify the clusters into 11 groups using atomistic descriptors and 5 groups using cluster descriptors.

Parker and colleagues used iterative label spreading (ILS)[332] to determine two prototypes and seven different archetypes for a set of 1200 Pt clusters.[331] Important features in their classification were the standard deviation of the particle radius, the average coordination number of bulk atoms, the fraction of perfect fcc atoms in the particle, the fraction of perfect hcp atoms, the average coordination number of surface atoms, the fraction of surface atoms on a {111} facet, morphology category (branched, twinned, single crystal, sphere), and whether or not the surface is roughened. Figure 35 depicts

https://doi.org/10.1021/acs.chemrev.2c00831
Chem. Rev. XXXX, XXX, XXX−XXX

the best matched nanoparticles to prototype 1 (P1), a branched nanoparticle with 4115 atoms, and prototype 2 (P2), an Ino-Dh with 1660 atoms. Figure 35 also indicates the best matched nanoparticles to various archetypes A1−A7. A1 and A7 are a modified truncated octahedron and a truncated cube, respectively, with roughened surfaces. A3 and A4 are spheres; A3 with a relatively ordered surface and A4 with a roughened surface. A2 and A6 are branched particles, and A5 represents twinned particles. Collectively, these particles fall into the categories of single crystal, twinned, spherical, or branched, with or without surface roughening. A2, A3, A4, and A6 are members of P1, while A1, A5, and A7 are members of P2. These studies provide a theoretical basis for discussing structure−property relationships of nanoparticles that are not geometrically ideal.

A final application of machine learning to nanocrystals is in identifying structures with ideal properties for applications. To this end, Parker, Opletal, and Barnard used ILS to identify structure−property relationships of a set of 1300 Pt nanocrystals related to their efficacy as catalysts for the oxygen reduction reaction (ORR), the hydrogen evolution reaction (HER), and the hydrogen oxidation reaction (HOR).[333] From a list of 121 possible features, they identified two different classes of nanoparticles and within each class, they identified two different types based on their surface microstructure and surface facets. Figure 36 shows representative structures in each group. Particles in class 1 are shown in Figure 36a,b with high concentrations of surface microstructures and surface facets, respectively. Particles in class 2 are shown in Figure 36c,d with high concentrations of surface microstructures, and surface facets, respectively.

Each of the four different types of nanoparticles had a distinct set of associated features. For example, the five most important features associated with nanoparticles in class 1 surface microstructures (Figure 36a) relate to atom coordination numbers (number of nearest neighbors): (1) the average coordination number of all Pt atoms, (2) the concentration of Pt atoms with a coordination number of 10, (3) the concentration of Pt atoms with a coordination of 8, (4) the concentration of Pt atoms with a coordination of 11, and (5) the concentration of surface atoms with a coordination of 8. The five most important features associated with nanoparticles in class 1 surface facets [Figure 36b] relate to the size of the nanoparticles: (1) the average particle radius, (2) the total number of bulk atoms, (3) the total number of Pt−Pt bonds, (4) the total number of Pt atoms, and (5) the total volume of the nanoparticle. Each of the groups represented in Figure 36 were linked to HOR, HER, and ORR reactions and indicated that appropriate processing conditions could be selected to achieve nanoparticle morphologies suitable for catalyzing these reactions.

5. CONCLUSIONS AND OUTLOOK

As indicated in Figure 6, theoretical efforts to describe the morphologies of metal nanocrystals have encompassed a variety of theoretical techniques, each aimed at capturing different aspects. In reviewing theoretical efforts to characterize the thermodynamics of nanocrystal structure, a few themes emerge. First, although nanocrystal structures are typically characterized in terms of a few classic shapes, shown in Figure 7, these motifs are not sufficient to classify all nanocrystal structures. Figures 9 and 12−15 illustrate this point for equilibrium structures. Away from equilibrium, a variety of alternative structures occur and have been classified by machine learning, as we see in the discussion surrounding Figures 35 and 36. Indeed, the study by Parker, Opletal, and Barnard[333] (Figure 36 and related discussion) shows that such nonclassic shapes are desirable for applications in catalysis, further motivating the need for an extended nanocrystal classification scheme. While most studies focus on understanding nanocrystal shapes with minimum potential energy at zero K, there is a realization that such shapes may not persist at finite temperatures. Recent studies have implemented PTMD approaches (cf., Figures 14) to quantify nanocrystal shape distributions with minimum free energy.

It is evident that the solution-phase synthesis environment in the experimental realm is exceedingly complicated, involving liquid−solid interfaces, chemical reactions in solution and on surfaces, kinetic phenomena that can span several orders of magnitude in time, as well as multiple length scales. To capture the specificity of the chemical interactions involved in nanoparticle growth, it is desirable to integrate quantum-based approaches as much as possible. However, as we saw for the example of Au (Figures 11−15 and surrounding discussion), there is disagreement among various quantum methods and experiment for the structures of Au nanocrystals in vacuum, so Au would appear to be a good model system for benchmarking new theoretical developments and closing the gap with experiments. Toward achieving this aim, the role of machine learning in the development of new potentials with high fidelity to experiment will be important and, as discussed above and reviewed in ref 326, such new potentials are being developed.

The capability of theoretical studies to accurately describe liquid−solid interfaces is important in efforts to describe the solution-phase synthesis of metal nanocrystals. To date, this has been largely done using classical MD simulations based on force fields, as captured by the discussion surrounding Figures 19 and 27−29. A force field-based approach allows for sampling of the liquid-phase and is important for describing nanocrystal structures away from zero K. Approaches for describing nanocrystal Wulff shapes have integrated implicit solvent (Figure 16). As discussed above (Figure 18), Ringe et al. have recently reviewed various approaches for including solvent in first-principles-based calculations, and further developments along these lines will be important, not only in efforts to predict Wulff shapes (Figure 16), but also in efforts to predict capping molecules that promote the formation of specific nanocrystal shapes (Figures 17 and 34).

As was discussed above, the shapes of even small metal nanocrystals may be kinetic in origin. To this end, there has been effort in understanding shape-transformation mechanisms (Figures 22−24) and quantifying pathways for the shape evolution during the growth of small nanocrystals using MD simulations (Figures 25−27). However, in the interest of understanding and predicting morphologies for various applications, it is desirable to quantify when a small, fluxional nanocrystal becomes a locked into a seed shape (e.g., Figures 3 and 4) that will determine the kinetic shape of a larger nanocrystal. Accelerated MD simulations[269,270,334−339] that account for a liquid environment may be best suited for such studies.

Finally, there is a need to model the shapes and shape evolution nanocrystals that fall outside of the size range that can be captured in MD simulations. For such systems, a multiscale approach is needed and above, I discussed

https://doi.org/10.1021/acs.chemrev.2c00831
Chem. Rev. XXXX, XXX, XXX−XXX

calculation of kinetic Wulff shapes using classical (Figures 29−31) and quantum (Figures 32 and 33) methods that integrate the theory of absorbing Markov chains. To date, most of these calculations have not included solvent, as is desired for a proper kinetic description, and methods for including solvent need to be integrated. Advancing such methods one step further, kMC simulations are fully compatible with the theory of absorbing Markov chains[315,340] and can supplant Markov chain calculations for greater rigor. Though there have been few kMC simulations aimed at quantifying kinetic nanocrystal shapes, this technique seems promising to model shapes such as those in Figures 5 and 26, with greater credibility than MD simulations (Figure 26). Although kMC simulations can be quantitative if linked to quantum calculations for the rates of various processes, even empirical kMC simulations can provide valuable qualitative insight into the ramifications of facet- or location-selective deposition and etching, limited adsorbate mobility, and other phenomena on the evolution of nanocrystal morphology. All of the above features will benefit our efforts to understand structural evolution in nanocrystal syntheses.

AUTHOR INFORMATION

Author

Kristen A. Fichthorn − *Department of Chemical Engineering and Department of Physics, The Pennsylvania State University, University Park, Pennsylvania 16803, United States;* orcid.org/0000-0002-4256-714X

Complete contact information is available at: https://pubs.acs.org/10.1021/acs.chemrev.2c00831

Notes

The author declares no competing financial interest.

Biography

Kristen A. Fichthorn is the Merrell Fenske Professor of Chemical Engineering and a Professor of Physics at the Pennsylvania State University. She received a B.S. in Chemical Engineering from the University of Pennsylvania, a Ph.D. in Chemical Engineering from the University of Michigan, and spent one year as an IBM Postdoctoral Fellow at the University of California at Santa Barbara before joining Penn State. Professor Fichthorn's research is primarily in multiscale materials simulation, in which she develops and applies theoretical techniques ranging from quantum DFT to MD, Monte Carlo methods, and continuum theories to a diverse array of fundamental problems involving fluid−solid interfaces. Applications lie in nanoscale materials, thin-film and crystal growth, colloidal assembly, and wetting.

ACKNOWLEDGMENTS

This work is funded by the Department of Energy, Office of Basic Energy Sciences, Materials Science Division, grant DE FG02-07ER46414.

ABBREVIATIONS

ACSTEM = aberration-corrected scanning transmission microscopy
CI-NEB = climbing-image nudged elastic band
$CNAr^{Mes2}$ = terphenyl isocyanide ligand
CNA = common neighbor analysis
CO = cuboctahedron
CTAB = cetyltrimethylammonium bromide
Dh = decahedron
DFT = density-functional theory
DFTB = density functional tight binding
DEG = diethylene glycol
DS = diamond square
DSD = diamond-square-diamond
EAM = embedded atom method
EG = ethylene glycol
GGA = generalized gradient approximation
HAADF = high-angle annular dark field
HDA = hexadecylamine
HER = hydrogen evolution reaction
HOR = hydrogen oxidation reaction
HSA = harmonic superposition approximation
HSM = harmonic superposition method
Ih = icosahedron
ILS = iterative label spreading
kMC = kinetic Monte Carlo
LDA = local density approximation
LPTEM = liquid phase transmission electron microscopy
MD = molecular dynamics
MC = Monte Carlo
ORR = oxygen reduction reaction
PBE = Perdew, Burke, and Ernzerhof
PTMD = parallel tempering molecular dynamics
PMF = potential of mean force
PVP = polyvinylpyrrolidone
RGL = Rosato, Guillope, and Legrand
TEM = transmission electron microscopy
TEG = triethylene glycol
TO = truncated octahedron

REFERENCES

(1) An, K.; Somorjai, G. A. Size and Shape Control of Metal Nanoparticles for Reaction Selectivity in Catalysis. *ChemCatChem.* **2012**, *4*, 1512−1524.
(2) Seh, Z. W.; Kibsgaard, J.; Dickens, C. F.; Chorkendorff, I.; Norskov, J. K.; Jaramillo, T. F. Combining Theory and Experiment in Electrocatalysis: Insights into Materials Design. *Science* **2017**, *355*, eaad4998.
(3) Kim, M. J.; Cruz, M. A.; Yang, F.; Wiley, B. J. Accelerating Electrochemistry with Metal Nanowires. *Curr. Opin. Electrochem.* **2019**, *16*, 19−27.
(4) Hussain, S.; Erikson, H.; Kongi, N.; Sarapuu, A.; Solla-Gullon, J.; Maia, G.; Kannan, A. M.; Alonso-Vante, N.; Tammeveski, K. Oxygen Reduction Reaction on Nanostructured Pt-Based Electrocatalysts: A Review. *Int. J. Hydrogen Energy* **2020**, *45*, 31775−31797.
(5) Wang, Y. J.; Long, W. Y.; Wang, L. L.; Yuan, R. S.; Ignaszak, A.; Fang, B. Z.; Wilkinson, D. P. Unlocking the Door to Highly Active Orr Catalysts for Pemfc Applications: Polyhedron-Engineered Pt-Based Nanocrystals. *Energy Environ. Sci.* **2018**, *11*, 258−275.
(6) Chaudhari, N. K.; Joo, J.; Kim, B.; Ruqia, B.; Choi, S. I.; Lee, K. Recent Advances in Electrocatalysts toward the Oxygen Reduction Reaction: The Case of Ptni Octahedra. *Nanoscale* **2018**, *10*, 20073−20088.
(7) You, H.; Yang, S.; Ding, B.; Yang, H. Synthesis of Colloidal Metal and Metal Alloy Nanoparticles for Electrochemical Energy Applications. *Chem. Soc. Rev.* **2013**, *42*, 2880−2904.
(8) Strasser, P.; Gliech, M.; Kuehl, S.; Moeller, T. Electrochemical Processes on Solid Shaped Nanoparticles with Defined Facets. *Chem. Soc. Rev.* **2018**, *47*, 715−735.
(9) Li, Y. R.; Li, M. X.; Li, S. N.; Liu, Y. J.; Chen, J.; Wang, Y. A Review of Energy and Environment Electrocatalysis Based on High-Index Faceted Nanocrystals. *Rare Metals* **2021**, *40*, 3406−3441.

(10) Shi, Y.; Lyu, Z.; Zhao, M.; Chen, R.; Nguyen, Q. N.; Xia, Y. Noble-Metal Nanocrystals with Controlled Shapes for Catalytic and Electrocatalytic Applications. *Chem. Rev.* **2021**, *121*, 649−735.
(11) Luo, M.; Sun, Y.; Zhang, X.; Qin, Y.; Li, M.; Li, Y.; Li, C.; Yang, Y.; Wang, L.; Gao, P. Stable High-Index Faceted Pt Skin on Zigzag-Like Ptfe Nanowires Enhances Oxygen Reduction Catalysis. *Adv. Mater.* **2018**, *30*, 1705515.
(12) Iqbal, M.; Bando, Y.; Sun, Z.; Wu, K. C.; Rowan, A. E.; Na, J.; Guan, B. Y.; Yamauchi, Y. In Search of Excellence: Convex Versus Concave Noble Metal Nanostructures for Electrocatalytic Applications. *Adv. Mater.* **2021**, *33*, e2004554.
(13) Huang, L.; Zhang, X.; Wang, Q.; Han, Y.; Fang, Y.; Dong, S. Shape-Control of Pt-Ru Nanocrystals: Tuning Surface Structure for Enhanced Electrocatalytic Methanol Oxidation. *J. Am. Chem. Soc.* **2018**, *140*, 1142−1147.
(14) García-Cruz, L.; Montiel, V.; Solla-Gullón, J. Shape-Controlled Metal Nanoparticles for Electrocatalytic Applications. *Phys. Sci. Rev.* **2019**, *4*, 20170124.
(15) Li, S.; Miao, P.; Zhang, Y.; Wu, J.; Zhang, B.; Du, Y.; Han, X.; Sun, J.; Xu, P. Recent Advances in Plasmonic Nanostructures for Enhanced Photocatalysis and Electrocatalysis. *Adv. Mater.* **2021**, *33*, e2000086.
(16) Zhu, J.; Hu, L.; Zhao, P.; Lee, L. Y. S.; Wong, K. Y. Recent Advances in Electrocatalytic Hydrogen Evolution Using Nanoparticles. *Chem. Rev.* **2020**, *120*, 851−918.
(17) De Gregorio, G. L.; Burdyny, T.; Loiudice, A.; Iyengar, P.; Smith, W. A.; Buonsanti, R. Facet-Dependent Selectivity of Cu Catalysts in Electrochemical Co(2) Reduction at Commercially Viable Current Densities. *ACS Catal.* **2020**, *10*, 4854−4862.
(18) Franco, F.; Rettenmaier, C.; Jeon, H. S.; Roldan Cuenya, B. Transition Metal-Based Catalysts for the Electrochemical Co2 Reduction: From Atoms and Molecules to Nanostructured Materials. *Chem. Soc. Rev.* **2020**, *49*, 6884−6946.
(19) Wang, Y. X.; Niu, C. L.; Zhu, Y. C.; He, D.; Huang, W. X. Tunable Syngas Formation from Electrochemical Co2 Reduction on Copper Nanowire Arrays. *ACS Appl. Energy Mater.* **2020**, *3*, 9841−9847.
(20) Xie, C.; Niu, Z.; Kim, D.; Li, M.; Yang, P. Surface and Interface Control in Nanoparticle Catalysis. *Chem. Rev.* **2020**, *120*, 1184−1249.
(21) Li, Z.; Ji, S.; Liu, Y.; Cao, X.; Tian, S.; Chen, Y.; Niu, Z.; Li, Y. Well-Defined Materials for Heterogeneous Catalysis: From Nanoparticles to Isolated Single-Atom Sites. *Chem. Rev.* **2020**, *120*, 623−682.
(22) Rodrigues, T. S.; da Silva, A. G. M.; Camargo, P. H. C. Nanocatalysis by Noble Metal Nanoparticles: Controlled Synthesis for the Optimization and Understanding of Activities. *J. Mater. Chem. A* **2019**, *7*, 5857−5874.
(23) Cargnello, M. Colloidal Nanocrystals as Building Blocks for Well-Defined Heterogeneous Catalysts. *Chem. Mater.* **2019**, *31*, 576−596.
(24) Liu, L.; Corma, A. Metal Catalysts for Heterogeneous Catalysis: From Single Atoms to Nanoclusters and Nanoparticles. *Chem. Rev.* **2018**, *118*, 4981−5079.
(25) Ruditskiy, A.; Peng, H. C.; Xia, Y. Shape-Controlled Metal Nanocrystals for Heterogeneous Catalysis. *Annu. Rev. Chem. Biomol. Eng.* **2016**, *7*, 327−348.
(26) Fan, F. R.; Wang, R.; Zhang, H.; Wu, W. Emerging Beyond-Graphene Elemental 2d Materials for Energy and Catalysis Applications. *Chem. Soc. Rev.* **2021**, *50*, 10983−11031.
(27) Losch, P.; Huang, W. X.; Goodman, E. D.; Wrasman, C. J.; Holm, A.; Riscoe, A. R.; Schwalbe, J. A.; Cargnello, M. Colloidal Nanocrystals for Heterogeneous Catalysis. *Nano Today* **2019**, *24*, 15−47.
(28) Mitchell, S.; Qin, R.; Zheng, N.; Perez-Ramirez, J. Nanoscale Engineering of Catalytic Materials for Sustainable Technologies. *Nat. Nanotechnol.* **2021**, *16*, 129−139.
(29) Ruditskiy, A.; Choi, S. I.; Peng, H. C.; Xia, Y. N. Shape-Controlled Metal Nanocrystals for Catalytic Applications. *MRS Bull.* **2014**, *39*, 727−737.
(30) Navlani-García, M.; Salinas-Torres, D.; Mori, K.; Kuwahara, Y.; Yamashita, H. Tailoring the Size and Shape of Colloidal Noble Metal Nanocrystals as a Valuable Tool in Catalysis. *Catal. Surv. from Asia* **2019**, *23*, 127−148.
(31) Xin, Y.; Yu, K.; Zhang, L.; Yang, Y.; Yuan, H.; Li, H.; Wang, L.; Zeng, J. Copper-Based Plasmonic Catalysis: Recent Advances and Future Perspectives. *Adv. Mater.* **2021**, *33*, e2008145.
(32) da Silva, A. G. M.; Rodrigues, T. S.; Wang, J.; Camargo, P. H. C. Plasmonic Catalysis with Designer Nanoparticles. *Chem. Commun.* **2022**, *58*, 2055−2074.
(33) Kang, H.; Buchman, J. T.; Rodriguez, R. S.; Ring, H. L.; He, J.; Bantz, K. C.; Haynes, C. L. Stabilization of Silver and Gold Nanoparticles: Preservation and Improvement of Plasmonic Functionalities. *Chem. Rev.* **2019**, *119*, 664−699.
(34) Kazuma, E.; Kim, Y. Mechanistic Studies of Plasmon Chemistry on Metal Catalysts. *Angew. Chem., Int. Ed.* **2019**, *58*, 4800−4808.
(35) Zhang, Z.; Zhang, C.; Zheng, H.; Xu, H. Plasmon-Driven Catalysis on Molecules and Nanomaterials. *Acc. Chem. Res.* **2019**, *52*, 2506−2515.
(36) Aslam, U.; Chavez, S.; Linic, S. Controlling Energy Flow in Multimetallic Nanostructures for Plasmonic Catalysis. *Nat. Nanotechnol.* **2017**, *12*, 1000−1005.
(37) Kamat, P. V.; Hartland, G. V. Plasmons for Energy Conversion. *ACS Energy Lett.* **2018**, *3*, 1467−1469.
(38) Kherbouche, I.; Luo, Y.; Félidj, N.; Mangeney, C. Plasmon-Mediated Surface Functionalization: New Horizons for the Control of Surface Chemistry on the Nanoscale. *Chem. Mater.* **2020**, *32*, 5442−5454.
(39) Gelle, A.; Jin, T.; de la Garza, L.; Price, G. D.; Besteiro, L. V.; Moores, A. Applications of Plasmon-Enhanced Nanocatalysis to Organic Transformations. *Chem. Rev.* **2020**, *120*, 986−1041.
(40) Kamat, P. V. Meeting the Clean Energy Demand: Nanostructure Architectures for Solar Energy Conversion. *J. Phys. Chem. C* **2007**, *111*, 2834−2860.
(41) Macia, N.; Bresoli-Obach, R.; Nonell, S.; Heyne, B. Hybrid Silver Nanocubes for Improved Plasmon-Enhanced Singlet Oxygen Production and Inactivation of Bacteria. *J. Am. Chem. Soc.* **2019**, *141*, 684−692.
(42) Ma, J. Y.; Tan, X. J.; Zhang, Q. Q.; Wang, Y.; Zhang, J. L.; Wang, L. Z. Exploring the Size Effect of Pt Nanoparticles on the Photocatalytic Nonoxidative Coupling of Methane. *ACS Catal.* **2021**, *11*, 3352−3360.
(43) Choi, S. I.; Herron, J. A.; Scaranto, J.; Huang, H. W.; Wang, Y.; Xia, X. H.; Lv, T.; Park, J. H.; Peng, H. C.; Mavrikakis, M.; et al. A Comprehensive Study of Formic Acid Oxidation on Palladium Nanocrystals with Different Types of Facets and Twin Defects. *ChemCatChem.* **2015**, *7*, 2077−2084.
(44) Qian, W.; Xu, S.; Zhang, X.; Li, C.; Yang, W.; Bowen, C. R.; Yang, Y. Differences and Similarities of Photocatalysis and Electrocatalysis in Two-Dimensional Nanomaterials: Strategies, Traps, Applications and Challenges. *Nano-Micro Lett.* **2021**, *13*, 156.
(45) Jin, R.; Li, G.; Sharma, S.; Li, Y.; Du, X. Toward Active-Site Tailoring in Heterogeneous Catalysis by Atomically Precise Metal Nanoclusters with Crystallographic Structures. *Chem. Rev.* **2021**, *121*, 567−648.
(46) Santana, J. S.; Skrabalak, S. E. Continuous Flow Routes toward Designer Metal Nanocatalysts. *Adv. Energy Mater.* **2020**, *10*, 1902051.
(47) Wang, H.; Gu, X. K.; Zheng, X.; Pan, H.; Zhu, J.; Chen, S.; Cao, L.; Li, W. X.; Lu, J. Disentangling the Size-Dependent Geometric and Electronic Effects of Palladium Nanocatalysts Beyond Selectivity. *Sci. Adv.* **2019**, *5*, eaat6413.
(48) Higaki, T.; Li, Y.; Zhao, S.; Li, Q.; Li, S.; Du, X. S.; Yang, S.; Chai, J.; Jin, R. Atomically Tailored Gold Nanoclusters for Catalytic Application. *Angew. Chem., Int. Ed. Engl.* **2019**, *58*, 8291−8302.
(49) Akbar, S.; Anwar, A.; Noon, M. Z.; Elliott, J. M.; Squires, A. M. Platinum as an Electrocatalyst: Effect of Morphological Aspects of Pt/Pt-Based Materials. *Mater. Sci. Technol.* **2019**, *35*, 1−11.
(50) Xiao, B.; Niu, Z.; Wang, Y. G.; Jia, W.; Shang, J.; Zhang, L.; Wang, D.; Fu, Y.; Zeng, J.; He, W.; et al. Copper Nanocrystal Plane

https://doi.org/10.1021/acs.chemrev.2c00831
Chem. Rev. XXXX, XXX, XXX−XXX

Effect on Stereoselectivity of Catalytic Deoxygenation of Aromatic Epoxides. *J. Am. Chem. Soc.* **2015**, *137*, 3791−3794.
(51) Zhou, K.; Li, Y. Catalysis Based on Nanocrystals with Well-Defined Facets. *Angew. Chem., Int. Ed. Engl.* **2012**, *51*, 602−613.
(52) Xiao, L.; Zhuang, L.; Liu, Y.; Lu, J.; Abruna, H. D. Activating Pd by Morphology Tailoring for Oxygen Reduction. *J. Am. Chem. Soc.* **2009**, *131*, 602−608.
(53) Lee, I.; Delbecq, F.; Morales, R.; Albiter, M. A.; Zaera, F. Tuning Selectivity in Catalysis by Controlling Particle Shape. *Nat. Mater.* **2009**, *8*, 132−138.
(54) Ueno, K.; Oshikiri, T.; Sun, Q.; Shi, X.; Misawa, H. Solid-State Plasmonic Solar Cells. *Chem. Rev.* **2018**, *118*, 2955−2993.
(55) Gaponenko, S. V.; Guzatov, D. V. Colloidal Plasmonics for Active Nanophotonics. *Proc. IEEE* **2020**, *108*, 704−720.
(56) Volokh, M.; Mokari, T. Metal/Semiconductor Interfaces in Nanoscale Objects: Synthesis, Emerging Properties and Applications of Hybrid Nanostructures. *Nanoscale Adv.* **2020**, *2*, 930−961.
(57) Kholmicheva, N.; Royo Romero, L.; Cassidy, J.; Zamkov, M. Prospects and Applications of Plasmon-Exciton Interactions in the near-Field Regime. *Nanophotonics* **2018**, *8*, 613−628.
(58) Atwater, H. A.; Polman, A. Plasmonics for Improved Photovoltaic Devices. *Nat. Mater.* **2010**, *9*, 205−213.
(59) Ali, A.; El-Mellouhi, F.; Mitra, A.; Aissa, B. Research Progress of Plasmonic Nanostructure-Enhanced Photovoltaic Solar Cells. *Nanomaterials (Basel)* **2022**, *12*, 788.
(60) Juan, F. Y.; Wu, Y. Q.; Shi, B. B.; Wang, M. X.; Wang, M.; Xu, F.; Jia, J. B. A.; Wei, H. M.; Yang, T. Z.; Cao, B. Q. Plasmonic Au Nanooctahedrons Enhance Light Harvesting and Photocarrier Extraction in Perovskite Solar Cell. *ACS Appl. Energy Mater.* **2021**, *4*, 3201−3209.
(61) Qin, F.; Chen, Z.; Chen, X.; Yi, Z.; Yao, W.; Duan, T.; Wu, P.; Yang, H.; Li, G.; Yi, Y. A Tunable Triple-Band near-Infrared Metamaterial Absorber Based on Au Nano-Cuboids Array. *Nanomaterials (Basel)* **2020**, *10*, 207.
(62) Ye, W.; Long, R.; Huang, H.; Xiong, Y. Plasmonic Nanostructures in Solar Energy Conversion. *J. Mater. Chem. C* **2017**, *5*, 1008−1021.
(63) Jang, Y. H.; Jang, Y. J.; Kim, S.; Quan, L. N.; Chung, K.; Kim, D. H. Plasmonic Solar Cells: From Rational Design to Mechanism Overview. *Chem. Rev.* **2016**, *116*, 14982−15034.
(64) Chow, T. H.; Li, N.; Bai, X.; Zhuo, X.; Shao, L.; Wang, J. Gold Nanobipyramids: An Emerging and Versatile Type of Plasmonic Nanoparticles. *Acc. Chem. Res.* **2019**, *52*, 2136−2146.
(65) Ye, S.; Rathmell, A. R.; Chen, Z.; Stewart, I. E.; Wiley, B. J. Metal Nanowire Networks: The Next Generation of Transparent Conductors. *Adv. Mater.* **2014**, *26*, 6670−6687.
(66) Wang, J.; Liu, S.; Ban, C.; Jia, Z.; He, X.; Ma, J.; Pu, X.; Li, W.; Zhi, L. Halbach Array Assisted Assembly of Orderly Aligned Nickel Nanowire Networks as Transparent Conductive Films. *Nanotechnology* **2019**, *30*, 355301.
(67) Choi, S.; Han, S. I.; Jung, D.; Hwang, H. J.; Lim, C.; Bae, S.; Park, O. K.; Tschabrunn, C. M.; Lee, M.; Bae, S. Y.; et al. Highly Conductive, Stretchable and Biocompatible Ag-Au Core-Sheath Nanowire Composite for Wearable and Implantable Bioelectronics. *Nat. Nanotechnol.* **2018**, *13*, 1048−1056.
(68) Chee, S.-S.; Kim, H.; Son, M.; Ham, M.-H. Aspect Ratio Control of Copper Nanowire Via Solution Process and Its Flexible Transparent Conductive Electrode Applications. *Electron. Mater. Lett.* **2020**, *16*, 404−410.
(69) Zhu, Y. W.; Deng, Y. J.; Yi, P. Y.; Peng, L. F.; Lai, X. M.; Lin, Z. Q. Flexible Transparent Electrodes Based on Silver Nanowires: Material Synthesis, Fabrication, Performance, and Applications. *Adv. Mater. Technol.* **2019**, *4*, 1900413.
(70) Ye, S.; Rathmell, A. R.; Stewart, I. E.; Ha, Y. C.; Wilson, A. R.; Chen, Z.; Wiley, B. J. A Rapid Synthesis of High Aspect Ratio Copper Nanowires for High-Performance Transparent Conducting Films. *Chem. Commun. (Camb)* **2014**, *50*, 2562−2564.
(71) Zhang, D.; Wang, R.; Wen, M.; Weng, D.; Cui, X.; Sun, J.; Li, H.; Lu, Y. Synthesis of Ultralong Copper Nanowires for High-Performance Transparent Electrodes. *J. Am. Chem. Soc.* **2012**, *134*, 14283−14286.
(72) Rathmell, A. R.; Wiley, B. J. The Synthesis and Coating of Long, Thin Copper Nanowires to Make Flexible, Transparent Conducting Films on Plastic Substrates. *Adv. Mater.* **2011**, *23*, 4798−4803.
(73) Wu, C.; Kim, T. W.; Li, F.; Guo, T. Wearable Electricity Generators Fabricated Utilizing Transparent Electronic Textiles Based on Polyester/Ag Nanowires/Graphene Core-Shell Nanocomposites. *ACS Nano* **2016**, *10*, 6449−6457.
(74) Liman, M. L. R.; Islam, M. T.; Hossain, M. M. Mapping the Progress in Flexible Electrodes for Wearable Electronic Textiles: Materials, Durability, and Applications. *Adv. Electron. Mater.* **2022**, *8*, 2100578.
(75) Jung, J.; Cho, H.; Yuksel, R.; Kim, D.; Lee, H.; Kwon, J.; Lee, P.; Yeo, J.; Hong, S.; Unalan, H. E.; et al. Stretchable/Flexible Silver Nanowire Electrodes for Energy Device Applications. *Nanoscale* **2019**, *11*, 20356−20378.
(76) Zhang, Q.; Liang, Q. J.; Zhang, Z.; Kang, Z.; Liao, Q. L.; Ding, Y.; Ma, M. Y.; Gao, F. F.; Zhao, X.; Zhang, Y. Electromagnetic Shielding Hybrid Nanogenerator for Health Monitoring and Protection. *Adv. Funct. Mater.* **2018**, *28*, 1703801.
(77) Zhou, N. N.; Ao, H. R.; Chen, X. M.; Jiang, H. Y. A Wearable Piezoelectro-Triboelectric Sensor with Nanocomposite Electrodes for Human Physiological Detection. *Nano Energy* **2022**, *96*, 107127.
(78) Jin, I. S.; Choi, J.; Jung, J. W. Silver-Nanowire-Embedded Photopolymer Films for Transparent Film Heaters with Ultra-Flexibility, Quick Thermal Response, and Mechanical Reliability. *Adv. Electron. Mater.* **2021**, *7*, 2000698.
(79) Guo, Z. G.; Sun, C.; Zhao, J.; Cai, Z. S.; Ge, F. Y. Low-Voltage Electrical Heater Based on One-Step Fabrication of Conductive Cu Nanowire Networks for Application in Wearable Devices. *Adv. Mater. Interfaces* **2021**, *8*, 2001695.
(80) Papanastasiou, D. T.; Schultheiss, A.; Munoz-Rojas, D.; Celle, C.; Carella, A.; Simonato, J. P.; Bellet, D. Transparent Heaters: A Review. *Adv. Funct. Mater.* **2020**, *30*, 1910225.
(81) Hong, S.; Lee, H.; Lee, J.; Kwon, J.; Han, S.; Suh, Y. D.; Cho, H.; Shin, J.; Yeo, J.; Ko, S. H. Highly Stretchable and Transparent Metal Nanowire Heater for Wearable Electronics Applications. *Adv. Mater.* **2015**, *27*, 4744−4751.
(82) Jia, H.; Yang, X.; Kong, Q. Q.; Xie, L. J.; Guo, Q. G.; Song, G.; Liang, L. L.; Chen, J. P.; Li, Y.; Chen, C. M. Free-Standing, Anti-Corrosion, Super Flexible Graphene Oxide/Silver Nanowire Thin Films for Ultra-Wideband Electromagnetic Interference Shielding. *J. Mater. Chem. A* **2021**, *9*, 1180−1191.
(83) Jung, J.; Lee, H.; Ha, I.; Cho, H.; Kim, K. K.; Kwon, J.; Won, P.; Hong, S.; Ko, S. H. Highly Stretchable and Transparent Electromagnetic Interference Shielding Film Based on Silver Nanowire Percolation Network for Wearable Electronics Applications. *ACS Appl. Mater. Interfaces* **2017**, *9*, 44609−44616.
(84) Qin, F.; Yan, Z. Y.; Fan, J. F.; Cai, J. L.; Zhu, X. Z.; Zhang, X. G. Highly Uniform and Stable Transparent Electromagnetic Interference Shielding Film Based on Silver Nanowire-Pedot:Pss Composite for High Power Microwave Shielding. *Macromol. Mater. Eng.* **2021**, *306*, 2000607.
(85) Lin, S.; Wang, H. Y.; Wu, F.; Wang, Q. M.; Bai, X. P.; Zu, D.; Song, J. N.; Wang, D.; Liu, Z. L.; Li, Z. W. Room-Temperature Production of Silver-Nanofiber Film for Large-Area, Transparent and Flexible Surface Electromagnetic Interference Shielding. *npj Flex. Electron.* **2019**, *3*, 6.
(86) Won, P.; Park, J. J.; Lee, T.; Ha, I.; Han, S.; Choi, M.; Lee, J.; Hong, S.; Cho, K. J.; Ko, S. H. Stretchable and Transparent Kirigami Conductor of Nanowire Percolation Network for Electronic Skin Applications. *Nano Lett.* **2019**, *19*, 6087−6096.
(87) Ding, S.; Jiu, J.; Gao, Y.; Tian, Y.; Araki, T.; Sugahara, T.; Nagao, S.; Nogi, M.; Koga, H.; Suganuma, K.; et al. One-Step Fabrication of Stretchable Copper Nanowire Conductors by a Fast Photonic Sintering Technique and Its Application in Wearable Devices. *ACS Appl. Mater. Interfaces* **2016**, *8*, 6190−6199.

https://doi.org/10.1021/acs.chemrev.2c00831
Chem. Rev. XXXX, XXX, XXX−XXX

(88) Lin, S.; Bai, X.; Wang, H.; Wang, H.; Song, J.; Huang, K.; Wang, C.; Wang, N.; Li, B.; Lei, M.; Wu, H. Roll-to-Roll Production of Transparent Silver-Nanofiber-Network Electrodes for Flexible Electrochromic Smart Windows. *Adv. Mater.* **2017**, *29*, 1703238.
(89) Madaria, A. R.; Kumar, A.; Zhou, C. Large Scale, Highly Conductive and Patterned Transparent Films of Silver Nanowires on Arbitrary Substrates and Their Application in Touch Screens. *Nanotechnology* **2011**, *22*, 245201.
(90) Mutiso, R. M.; Sherrott, M. C.; Rathmell, A. R.; Wiley, B. J.; Winey, K. I. Integrating Simulations and Experiments to Predict Sheet Resistance and Optical Transmittance in Nanowire Films for Transparent Conductors. *ACS Nano* **2013**, *7*, 7654−7663.
(91) Zhang, P. P.; Liao, Q. H.; Yao, H. Z.; Huang, Y. X.; Cheng, H. H.; Qu, L. T. Direct Solar Steam Generation System for Clean Water Production. *Energy Storage Mater.* **2019**, *18*, 429−446.
(92) Zhang, C.; Liang, H. Q.; Xu, Z. K.; Wang, Z. Harnessing Solar-Driven Photothermal Effect toward the Water-Energy Nexus. *Adv. Sci.* **2019**, *6*, 1900883.
(93) Li, Z.; Xu, X.; Sheng, X.; Lin, P.; Tang, J.; Pan, L.; Kaneti, Y. V.; Yang, T.; Yamauchi, Y. Solar-Powered Sustainable Water Production: State-of-the-Art Technologies for Sunlight-Energy-Water Nexus. *ACS Nano* **2021**, *15*, 12535.
(94) Zhou, L.; Tan, Y.; Wang, J.; Xu, W.; Yuan, Y.; Cai, W.; Zhu, S.; Zhu, J. 3d Self-Assembly of Aluminium Nanoparticles for Plasmon-Enhanced Solar Desalination. *Nat. Photonics* **2016**, *10*, 393−398.
(95) Gao, M.; Connor, P. K. N.; Ho, G. W. Plasmonic Photothermic Directed Broadband Sunlight Harnessing for Seawater Catalysis and Desalination. *Energy Environ. Sci.* **2016**, *9*, 3151−3160.
(96) Gong, H.; Liu, X.; Liu, G. L.; Lin, Z. H.; Yu, X. Q.; Zhou, L. Non-Noble Metal Based Broadband Photothermal Absorbers for Cost Effective Interfacial Solar Thermal Conversion. *Nanophotonics* **2020**, *9*, 1539−1546.
(97) Sheng, C. M.; Yang, N.; Yan, Y. T.; Shen, X. P.; Jin, C. D.; Wang, Z.; Sun, Q. F. Bamboo Decorated with Plasmonic Nanoparticles for Efficient Solar Steam Generation. *Appl. Therm. Eng.* **2020**, *167*, 114712.
(98) Chen, C. R.; Qin, H.; Cong, H. P.; Yu, S. H. A Highly Stretchable and Real-Time Healable Supercapacitor. *Adv. Mater.* **2019**, *31*, e1900573.
(99) Nayak, L.; Mohanty, S.; Nayak, S. K.; Ramadoss, A. A Review on Inkjet Printing of Nanoparticle Inks for Flexible Electronics. *J. Mater. Chem. C* **2019**, *7*, 8771−8795.
(100) Cheng, T.; Zhang, Y. Z.; Yi, J. P.; Yang, L.; Zhang, J. D.; Lai, W. Y.; Huang, W. Inkjet-Printed Flexible, Transparent and Aesthetic Energy Storage Devices Based on Pedot: Pss/Ag Grid Electrodes. *J. Mater. Chem. A* **2016**, *4*, 13754−13763.
(101) Mallikarjuna, K.; Kim, H. Highly Transparent Conductive Reduced Graphene Oxide/Silver Nanowires/Silver Grid Electrodes for Low-Voltage Electrochromic Smart Windows. *ACS Appl. Mater. Interfaces* **2019**, *11*, 1969−1978.
(102) Shinde, M. A.; Kim, H. Flexible Electrochromic Device with Simple Solution Processed Stable Silver Nanowire Based Transparent Conductive Electrodes. *Synth. Met.* **2019**, *254*, 97−105.
(103) Grzybowski, B. A.; Huck, W. T. The Nanotechnology of Life-Inspired Systems. *Nat. Nanotechnol.* **2016**, *11*, 585−592.
(104) Ragazzon, G.; Prins, L. J. Energy Consumption in Chemical Fuel-Driven Self-Assembly. *Nat. Nanotechnol.* **2018**, *13*, 882−889.
(105) Zhang, H.; Jin, M.; Xia, Y. Noble-Metal Nanocrystals with Concave Surfaces: Synthesis and Applications. *Angew. Chem., Int. Ed.* **2012**, *51*, 7656−7673.
(106) Quan, Z.; Wang, Y.; Fang, J. High-Index Faceted Noble Metal Nanocrystals. *Acc. Chem. Res.* **2013**, *46*, 191−202.
(107) Xiao, C.; Lu, B.-A.; Xue, P.; Tian, N.; Zhou, Z.-Y.; Lin, X.; Lin, W.-F.; Sun, S.-G. High-Index-Facet- and High-Surface-Energy Nanocrystals of Metals and Metal Oxides as Highly Efficient Catalysts. *Joule* **2020**, *4*, 2562−2598.
(108) Wang, Y.; Jiang, X.; Fu, G.; Li, Y.; Tang, Y.; Lee, J. M.; Tang, Y. Cu(5)Pt Dodecahedra with Low-Pt Content: Facile Synthesis and Outstanding Formic Acid Electrooxidation. *ACS Appl. Mater. Interfaces* **2019**, *11*, 34869−34877.
(109) Zhang, J.; Dong, Y.; Liu, Q.; Zhou, M.; Mi, G.; Du, X. Hierarchically Alloyed Pd−Cu Microarchitecture with Tunable Shapes: Morphological Engineering, and Catalysis for Hydrogen Evolution Reaction of Ammonia Borane. *Int. J. Hydrogen Energy* **2019**, *44*, 30226−30236.
(110) Wu, F.; Lai, J.; Zhang, L.; Niu, W.; Lou, B.; Luque, R.; Xu, G. Hierarchical Concave Layered Triangular Ptcu Alloy Nanostructures: Rational Integration of Dendritic Nanostructures for Efficient Formic Acid Electrooxidation. *Nanoscale* **2018**, *10*, 9369−9375.
(111) Thota, S.; Wang, Y.; Zhao, J. Colloidal Au−Cu Alloy Nanoparticles: Synthesis, Optical Properties and Applications. *Mater. Chem. Front.* **2018**, *2*, 1074−1089.
(112) Jung, H.; King, M. E.; Personick, M. L. Strategic Synergy: Advances in the Shape Control of Bimetallic Nanoparticles with Dilute Alloyed Surfaces. *Curr. Opin. Colloid Interface Sci.* **2019**, *40*, 104−117.
(113) Skrabalak, S. E. Symmetry in Seeded Metal Nanocrystal Growth. *Acc. Mater. Res.* **2021**, *2*, 621−629.
(114) Wu, J.; Chen, X.; Fan, J.; Guo, Y.; Fang, W. Control of Reduction Kinetics to Form Palladium Nanocubes Enables Tunable Concavity. *Chem. Mater.* **2020**, *32*, 4591−4599.
(115) Du, G.; Chen, Q.; Jin, H.; Xie, S.; Kuang, Q.; Xie, Z. Concave Nano-Octahedral Alloys: Wet Chemical Synthesis of Bimetallic Pt−Pd Nanocrystals with High-Index {Hhl} Facets. *Dalton Trans.* **2021**, *50*, 12083−12087.
(116) Wang, H. L.; Zhou, S.; Gilroy, K. D.; Cai, Z. S.; Xia, Y. N. Icosahedral Nanocrystals of Noble Metals: Synthesis and Applications. *Nano Today* **2017**, *15*, 121−144.
(117) Zhou, S.; Zhao, M.; Yang, T. H.; Xia, Y. N. Decahedral Nanocrystals of Noble Metals: Synthesis, Characterization, and Applications. *Mater. Today* **2019**, *22*, 108−131.
(118) Qin, D. Framing Silver Nanocrystals with a Second Metal to Enhance Shape Stability and Expand Functionality. *Acc. Mater. Res.* **2022**, *3*, 391−402.
(119) Baletto, F. Structural Properties of Sub-Nanometer Metallic Clusters. *J. Phys.: Condens. Matter* **2019**, *31*, 113001.
(120) Fichthorn, K. A.; Yan, T. Shapes and Shape Transformations of Solution-Phase Metal Particles in the Sub-Nanometer to Nanometer Size Range: Progress and Challenges. *J. Phys. Chem. C* **2021**, *125*, 3668−3679.
(121) Marks, L. D.; Peng, L. Nanoparticle Shape, Thermodynamics and Kinetics. *J. Phys.: Condens. Matter* **2016**, *28*, No. 053001.
(122) Li, D.; Chen, Q.; Chun, J.; Fichthorn, K.; De Yoreo, J.; Zheng, H. Nanoparticle Assembly and Oriented Attachment: Correlating Controlling Factors to the Resulting Structures. *Chem. Rev.* **2023**. DOI: 10.1021/acs.chemrev.2c00700
(123) Han, Y.; Duan, X.; Zhu, B.; Gao, Y. Insights into Structure of Metal Nanomaterials in Reactive Environments. *WIREs Comput. Mol. Sci.* **2022**, *12*, e1587.
(124) Xia, Y.; Xiong, Y.; Lim, B.; Skrabalak, S. E. Shape-Controlled Synthesis of Metal Nanocrystals: Simple Chemistry Meets Complex Physics? *Angew. Chem., Int. Ed. Engl.* **2009**, *48*, 60−103.
(125) Gilroy, K. D.; Peng, H. C.; Yang, X.; Ruditskiy, A.; Xia, Y. Symmetry Breaking During Nanocrystal Growth. *Chem. Commun. (Camb)* **2017**, *53*, 4530−4541.
(126) Iijima, S.; Ichihashi, T. Structural Instability of Ultrafine Particles of Metals. *Phys. Rev. Lett.* **1986**, *56*, 616−619.
(127) Smith, D. J.; Petford-Long, A. K.; Wallenberg, L. R.; Bovin, J. O. Dynamic Atomic-Level Rearrangements in Small Gold Particles. *Science* **1986**, *233*, 872−875.
(128) Wang, Z. W.; Palmer, R. E. Determination of the Ground-State Atomic Structures of Size-Selected Au Nanoclusters by Electron-Beam-Induced Transformation. *Phys. Rev. Lett.* **2012**, *108*, 245502.
(129) Plant, S. R.; Cao, L.; Palmer, R. E. Atomic Structure Control of Size-Selected Gold Nanoclusters During Formation. *J. Am. Chem. Soc.* **2014**, *136*, 7559−7562.

https://doi.org/10.1021/acs.chemrev.2c00831
Chem. Rev. XXXX, XXX, XXX−XXX

(130) Wells, D. M.; Rossi, G.; Ferrando, R.; Palmer, R. E. Metastability of the Atomic Structures of Size-Selected Gold Nanoparticles. *Nanoscale* **2015**, *7*, 6498−6503.
(131) Foster, D. M.; Ferrando, R.; Palmer, R. E. Experimental Determination of the Energy Difference between Competing Isomers of Deposited, Size-Selected Gold Nanoclusters. *Nat. Commun.* **2018**, *9*, 1323.
(132) Lambie, S. G.; Weal, G. R.; Blackmore, C. E.; Palmer, R. E.; Garden, A. L. Contrasting Motif Preferences of Platinum and Gold Nanoclusters between 55 and 309 Atoms. *Nanoscale Adv.* **2019**, *1*, 2416−2425.
(133) Chan, C. H.; Poignant, F.; Beuve, M.; Dumont, E.; Loffreda, D. Effect of the Ligand Binding Strength on the Morphology of Functionalized Gold Nanoparticles. *J. Phys. Chem. Lett.* **2020**, *11*, 2717−2723.
(134) Lai, K. C.; Chen, M.; Yu, J.; Han, Y.; Huang, W.; Evans, J. W. Shape Stability of Truncated Octahedral Fcc Metal Nanocrystals. *ACS Appl. Mater. Interfaces* **2021**, *13*, 51954−51961.
(135) Northby, J. A.; Xie, J.; Freeman, D. L.; Doll, J. D. Binding-Energy of Large Icosahedral and Cuboctahedral Lennard-Jones Clusters. *Z. Phys. D Atom Mol. Cl.* **1989**, *12*, 69−71.
(136) Baletto, F.; Ferrando, R.; Fortunelli, A.; Montalenti, F.; Mottet, C. Crossover among Structural Motifs in Transition and Noble-Metal Clusters. *J. Chem. Phys.* **2002**, *116*, 3856−3863.
(137) Cleveland, C. L.; Landman, U. The Energetics and Structure of Nickel Clusters: Size Dependence. *J. Chem. Phys.* **1991**, *94*, 7376−7396.
(138) Doye, J. P. K.; Wales, D. J. Structural Consequences of the Range of the Interatomic Potential - a Menagerie of Clusters. *J. Chem. Soc. Faraday T* **1997**, *93*, 4233−4243.
(139) Ino, S. Stability of Multiply-Twinned Particles. *J. Phys. Soc. Jpn.* **1969**, *27*, 941−953.
(140) Marks, L. D. Surface-Structure and Energetics of Multiply Twinned Particles. *Philos. Mag. A* **1984**, *49*, 81−93.
(141) Rahm, J. M.; Erhart, P. Beyond Magic Numbers: Atomic Scale Equilibrium Nanoparticle Shapes for Any Size. *Nano Lett.* **2017**, *17*, 5775−5781.
(142) Herring, C. Some Theorems on the Free Energies of Crystal Surfaces. *Phys. Rev.* **1951**, *82*, 87−93.
(143) Kaatz, F. H.; Bultheel, A. Magic Mathematical Relationships for Nanoclusters. *Nanoscale Res. Lett.* **2019**, *14*, 150.
(144) Martin, T. P. Shells of Atoms. *Phys. Rep.* **1996**, *273*, 199−241.
(145) Mottet, C.; Tréglia, G.; Legrand, B. New Magic Numbers in Metallic Clusters: An Unexpected Metal Dependence. *Surf. Sci.* **1997**, *383*, L719−L727.
(146) Garden, A. L.; Pedersen, A.; Jonsson, H. Reassignment of 'Magic Numbers' for Au Clusters of Decahedral and Fcc Structural Motifs. *Nanoscale* **2018**, *10*, 5124−5132.
(147) Jindal, S.; Bulusu, S. S. Structural Evolution in Gold Nanoparticles Using Artificial Neural Network Based Interatomic Potentials. *J. Chem. Phys.* **2020**, *152*, 154302.
(148) Tsuji, M.; Ogino, M.; Matsuo, R.; Kumagae, H.; Hikino, S.; Kim, T.; Yoon, S.-H. Stepwise Growth of Decahedral and Icosahedral Silver Nanocrystals in Dmf. *Cryst. Growth Des.* **2010**, *10*, 296−301.
(149) Huang, H. W.; Wang, Y.; Ruditskiy, A.; Peng, H. C.; Zhao, X.; Zhang, L.; Liu, J. Y.; Ye, Z. Z.; Xia, Y. N. Polyol Syntheses of Palladium Decahedra and Icosahedra as Pure Samples by Maneuvering the Reaction Kinetics with Additives. *ACS Nano* **2014**, *8*, 7041−7050.
(150) Figueroa-Cosme, L.; Gilroy, K. D.; Yang, T. H.; Vara, M.; Park, J.; Bao, S.; da Silva, A. G. M.; Xia, Y. Synthesis of Palladium Nanoscale Octahedra through a One-Pot, Dual-Reductant Route and Kinetic Analysis. *Chem.—Eur. J.* **2018**, *24*, 6133−6139.
(151) Goebl, J.; Zhang, Q.; He, L.; Yin, Y. Monitoring the Shape Evolution of Silver Nanoplates: A Marker Study. *Angew. Chem., Int. Ed. Engl.* **2012**, *51*, 552−555.
(152) Kim, M. J.; Cruz, M. A.; Chen, Z. H.; Xu, H.; Brown, M.; Fichthorn, K. A.; Wiley, B. J. Isotropic Iodide Adsorption Causes Anisotropic Growth of Copper Microplates. *Chem. Mater.* **2021**, *33*, 881−891.
(153) Mai Ngoc, T. A.; Nguyen, D. T. D.; Ngo, V. K. T.; Nguyen Thi, P. P.; Nguyen, D. H.; Nguyen-Le, M.-T. A Systematic Study of the One-Pot Fabrication of Anisotropic Silver Nanoplates with Controllable Size and Shape for Sers Amplification. *Plasmonics* **2020**, *15*, 2185−2194.
(154) Li, Y.; Fan, Z. Y.; Yuan, X. M.; Yang, H. W.; Li, Y. X.; Wang, C. Dodecylamine-Mediated Synthesis and Growth Mechanism of Copper Nanowires with an Aspect Ratio of over 10000. *Mater. Lett.* **2020**, *274*, 128029.
(155) Kumar, A.; Mohammadi, M. M.; Swihart, M. T. Synthesis, Growth Mechanisms, and Applications of Palladium-Based Nanowires and Other One-Dimensional Nanostructures. *Nanoscale* **2019**, *11*, 19058−19085.
(156) Baletto, F.; Ferrando, R. Structural Properties of Nanoclusters: Energetic, Thermodynamic, and Kinetic Effects. *Rev. Mod. Phys.* **2005**, *77*, 371−423.
(157) Jennison, D. R.; Schultz, P. A.; Sears, M. P. Ab Initio Calculations of Ru, Pd, and Ag Cluster Structure with 55, 135, and 140 Atoms. *J. Chem. Phys.* **1997**, *106*, 1856−1862.
(158) Hohenberg, P.; Kohn, W. Inhomogeneous Electron Gas. *Phys. Rev. B* **1964**, *136*, B864.
(159) Wang, B. Y.; Liu, M. X.; Wang, Y. T.; Chen, X. S. Structures and Energetics of Silver and Gold Nanoparticles. *J. Phys. Chem. C* **2011**, *115*, 11374−11381.
(160) Jindal, S.; Chiriki, S.; Bulusu, S. S. Spherical Harmonics Based Descriptor for Neural Network Potentials: Structure and Dynamics of Au147 Nanocluster. *J. Chem. Phys.* **2017**, *146*, 204301.
(161) Piotrowski, M. J.; Ungureanu, C. G.; Tereshchuk, P.; Batista, K. E. A.; Chaves, A. S.; Guedes-Sobrinho, D.; Da Silva, J. L. F. Theoretical Study of the Structural, Energetic, and Electronic Properties of 55-Atom Metal Nanoclusters: A Dft Investigation within Van Der Waals Corrections, Spin−Orbit Coupling, and Pbe +Uof 42 Metal Systems. *J. Phys. Chem. C* **2016**, *120*, 28844−28856.
(162) Farkas, B.; de Leeuw, N. H. Towards a Morphology of Cobalt Nanoparticles: Size and Strain Effects. *Nanotechnology* **2020**, *31*, 195711.
(163) Loffreda, D.; Foster, D. M.; Palmer, R. E.; Tarrat, N. Importance of Defective and Nonsymmetric Structures in Silver Nanoparticles. *J. Phys. Chem. Lett.* **2021**, *12*, 3705−3711.
(164) Cleveland, C. L.; Luedtke, W. D.; Landman, U. Melting of Gold Clusters. *Phys. Rev. B* **1999**, *60*, 5065−5077.
(165) Li, H.; Li, L.; Pedersen, A.; Gao, Y.; Khetrapal, N.; Jonsson, H.; Zeng, X. C. Magic-Number Gold Nanoclusters with Diameters from 1 to 3.5 Nm: Relative Stability and Catalytic Activity for Co Oxidation. *Nano Lett.* **2015**, *15*, 682−688.
(166) Barnard, A. S.; Curtiss, L. A. Predicting the Shape and Structure of Face-Centered Cubic Gold Nanocrystals Smaller Than 3 Nm. *ChemPhysChem* **2006**, *7*, 1544−1553.
(167) Duan, Z. Y.; Li, Y. Y.; Timoshenko, J.; Chill, S. T.; Anderson, R. M.; Yancey, D. F.; Frenkel, A. I.; Crooks, R. M.; Henkelman, G. A Combined Theoretical and Experimental Exafs Study of the Structure and Dynamics of Au147 Nanoparticles. *Catalysis Science & Technology* **2016**, *6*, 6879−6885.
(168) Daw, M. S.; Baskes, M. I. Embedded-Atom Method: Derivation and Application to Impurities, Surfaces, and Other Defects in Metals. *Phys. Rev. B* **1984**, *29*, 6443−6453.
(169) Foiles, S. M.; Baskes, M. I.; Daw, M. S. Embedded-Atom-Method Functions for the Fcc Metals Cu, Ag, Au, Ni, Pd, Pt, and Their Alloys. *Phys. Rev. B* **1986**, *33*, 7983−7991.
(170) Rosato, V.; Guillope, M.; Legrand, B. Thermodynamical and Structural Properties of F.C.C. Transition Metals Using a Simple Tight-Binding Model. *Philos. Mag. A* **1989**, *59*, 321−336.
(171) Garzon, I. L.; Posada-Amarillas, A. Structural and Vibrational Analysis of Amorphous Au55 Clusters. *Phys. Rev. B* **1996**, *54*, 11796−11802.
(172) Garzón, I. L.; Michaelian, K.; Beltrán, M. R.; Posada-Amarillas, A.; Ordejón, P.; Artacho, E.; Sánchez-Portal, D.; Soler, J.

https://doi.org/10.1021/acs.chemrev.2c00831
Chem. Rev. XXXX, XXX, XXX−XXX

M. Lowest Energy Structures of Gold Nanoclusters. *Phys. Rev. Lett.* **1998**, *81*, 1600−1603.
(173) Soler, J. M.; Garzon, I. L.; Joannopoulos, J. D. Structural Patterns of Unsupported Gold Clusters. *Solid State Commun.* **2001**, *117*, 621−625.
(174) Bao, K.; Goedecker, S.; Koga, K.; Lançon, F.; Neelov, A. Structure of Large Gold Clusters Obtained by Global Optimization Using the Minima Hopping Method. *Phys. Rev. B* **2009**, *79*, 041405.
(175) Tarrat, N.; Rapacioli, M.; Cuny, J.; Morillo, J.; Heully, J. L.; Spiegelman, F. Global Optimization of Neutral and Charged 20-and 55-Atom Silver and Gold Clusters at the Dftb Level. *Computational and Theoretical Chemistry* **2017**, *1107*, 102−114.
(176) Häkkinen, H.; Moseler, M.; Kostko, O.; Morgner, N.; Hoffmann, M. A.; v Issendorff, B. Symmetry and Electronic Structure of Noble-Metal Nanoparticles and the Role of Relativity. *Phys. Rev. Lett.* **2004**, *93*, 093401.
(177) Thorn, A.; Rojas-Nunez, J.; Hajinazar, S.; Baltazar, S. E.; Kolmogorov, A. N. Toward Ab Initio Ground States of Gold Clusters Via Neural Network Modeling. *J. Phys. Chem. C* **2019**, *123*, 30088−30098.
(178) Gupta, R. P. Lattice Relaxation at a Metal Surface. *Phys. Rev. B* **1981**, *23*, 6265−6270.
(179) Wang, Z. W.; Palmer, R. E. Experimental Evidence for Fluctuating, Chiral-Type Au55 Clusters by Direct Atomic Imaging. *Nano Lett.* **2012**, *12*, 5510−5514.
(180) Schebarchov, D.; Baletto, F.; Wales, D. J. Structure, Thermodynamics, and Rearrangement Mechanisms in Gold Clusters—Insights from the Energy Landscapes Framework. *Nanoscale* **2018**, *10*, 2004−2016.
(181) Perdew, J. P.; Burke, K.; Ernzerhof, M. Generalized Gradient Approximation Made Simple. *Phys. Rev. Lett.* **1996**, *77*, 3865−3868.
(182) Doye, J. P. K.; Wales, D. J. Calculation of Thermodynamic Properties of Small Lennard-Jones Clusters Incorporating Anharmonicity. *J. Chem. Phys.* **1995**, *102*, 9659−9672.
(183) Settem, M.; Ferrando, R.; Giacomello, A. Tempering of Au Nanoclusters: Capturing the Temperature-Dependent Competition among Structural Motifs. *Nanoscale* **2022**, *14*, 939−952.
(184) Trygubenko, S. A.; Wales, D. J. A Doubly Nudged Elastic Band Method for Finding Transition States. *J. Chem. Phys.* **2004**, *120*, 2082−2094.
(185) Henkelman, G.; Uberuaga, B. P.; Jonsson, H. A Climbing Image Nudged Elastic Band Method for Finding Saddle Points and Minimum Energy Paths. *J. Chem. Phys.* **2000**, *113*, 9901−9904.
(186) Faken, D.; Jonsson, H. Systematic Analysis of Local Atomic Structure Combined with 3d Computer Graphics. *Comput. Mater. Sci.* **1994**, *2*, 279−286.
(187) Becker, O. M.; Karplus, M. The Topology of Multidimensional Potential Energy Surfaces: Theory and Application to Peptide Structure and Kinetics. *J. Chem. Phys.* **1997**, *106*, 1495−1517.
(188) Ouyang, R.; Xie, Y.; Jiang, D.-E. Global Minimization of Gold Clusters by Combining Neural Network Potentials and the Basin-Hopping Method. *Nanoscale* **2015**, *7*, 14817−14821.
(189) Dong, C. D.; Gong, X. G. Gold Cluster Beyond Hollow Cage: A Double Shell Structure of Au58. *J. Chem. Phys.* **2010**, *132*, 104301.
(190) Wang, J.; Jellinek, J.; Zhao, J.; Chen, Z.; King, R. B.; Von Ragué Schleyer, P. Hollow Cages Versus Space-Filling Structures for Medium-Sized Gold Clusters: The Spherical Aromaticity of the Au50 Cage. *J. Phys. Chem. A* **2005**, *109*, 9265−9269.
(191) Da Silva, J. L. F.; Kim, H. G.; Piotrowski, M. J.; Prieto, M. J.; Tremiliosi-Filho, G. Reconstruction of Core and Surface Nanoparticles: The Example of Pt55 and Au55. *Phys. Rev. B* **2010**, *82*, 205424.
(192) Bulusu, S.; Zeng, X. C. Structures and Relative Stability of Neutral Gold Clusters: Aun (N = 15−19). *J. Chem. Phys.* **2006**, *125*, 154303.
(193) Bulusu, S.; Li, X.; Wang, L. S.; Zeng, X. C. Evidence of Hollow Golden Cages. *Proceedings of the National Academy of Science U S A* **2006**, *103*, 8326−8330.
(194) Tarrat, N.; Rapacioli, M.; Spiegelman, F. Au(147) Nanoparticles: Ordered or Amorphous? *J. Chem. Phys.* **2018**, *148*, 204308.
(195) Duan, Z.; Li, Y.; Timoshenko, J.; Chill, S. T.; Anderson, R. M.; Yancey, D. F.; Frenkel, A. I.; Crooks, R. M.; Henkelman, G. A Combined Theoretical and Experimental Exafs Study of the Structure and Dynamics of Au147 Nanoparticles. *Catalysis Science & Technology* **2016**, *6*, 6879−6885.
(196) Tao, J.; Perdew, J. P.; Staroverov, V. N.; Scuseria, G. E. Climbing the Density Functional Ladder: Nonempirical Meta-Generalized Gradient Approximation Designed for Molecules and Solids. *Phys. Rev. Lett.* **2003**, *91*, 146401.
(197) Earl, D. J.; Deem, M. W. Parallel Tempering: Theory, Applications, and New Perspectives. *Phys. Chem. Chem. Phys.* **2005**, *7*, 3910.
(198) Zeni, C.; Rossi, K.; Pavloudis, T.; Kioseoglou, J.; de Gironcoli, S.; Palmer, R. E.; Baletto, F. Data-Driven Simulation and Characterisation of Gold Nanoparticle Melting. *Nat. Commun.* **2021**, *12*, 6056.
(199) Oliveira, L. F. L.; Tarrat, N.; Cuny, J.; Morillo, J.; Lemoine, D.; Spiegelman, F.; Rapacioli, M. Benchmarking Density Functional Based Tight-Binding for Silver and Gold Materials: From Small Clusters to Bulk. *J. Phys. Chem. A* **2016**, *120*, 8469−8483.
(200) Logsdail, A. J.; Li, Z. Y.; Johnston, R. L. Faceting Preferences for Au(N) and Pd(N) Nanoclusters with High-Symmetry Motifs. *Phys. Chem. Chem. Phys.* **2013**, *15*, 8392−8400.
(201) Curley, B. C.; Johnston, R. L.; Young, N. P.; Li, Z. Y.; Di Vece, M.; Palmer, R. E.; Bleloch, A. L. Combining Theory and Experiment to Characterize the Atomic Structures of Surface-Deposited Au309 Clusters. *J. Phys. Chem. C* **2007**, *111*, 17846−17851.
(202) Li, Z. Y.; Young, N. P.; Di Vece, M.; Palomba, S.; Palmer, R. E.; Bleloch, A. L.; Curley, B. C.; Johnston, R. L.; Jiang, J.; Yuan, J. Three-Dimensional Atomic-Scale Structure of Size-Selected Gold Nanoclusters. *Nature* **2008**, *451*, 46−48.
(203) Rogan, J.; Garcia, G.; Loyola, C.; Orellana, W.; Ramirez, R.; Kiwi, M. Alternative Search Strategy for Minimal Energy Nanocluster Structures: The Case of Rhodium, Palladium, and Silver. *J. Chem. Phys.* **2006**, *125*, 214708.
(204) Alamanova, D.; Grigoryan, V. G.; Springborg, M. Theoretical Study of the Structure and Energetics of Silver Clusters. *J. Phys. Chem. C* **2007**, *111*, 12577−12587.
(205) Yang, X.; Cai, W.; Shao, X. Structural Variation of Silver Clusters from Ag13 to Ag160. *J. Phys. Chem. A* **2007**, *111*, 5048−5056.
(206) Chepulskii, R. V.; Curtarolo, S. Ab Initio Insights on the Shapes of Platinum Nanocatalysts. *ACS Nano* **2011**, *5*, 247−254.
(207) Blazhynska, M. M.; Kyrychenko, A.; Kalugin, O. N. Molecular Dynamics Simulation of the Size-Dependent Morphological Stability of Cubic Shape Silver Nanoparticles. *Mol. Simul.* **2018**, *44*, 981−991.
(208) De Mendonça, J. P. A.; Calderan, F. V.; Lourenço, T. C.; Quiles, M. G.; Da Silva, J. L. F. Theoretical Framework Based on Molecular Dynamics and Data Mining Analyses for the Study of Potential Energy Surfaces of Finite-Size Particles. *J. Chem. Inf. Model.* **2022**, *62*, 5503−5512.
(209) Guedes-Sobrinho, D.; Chaves, A. S.; Piotrowski, M. J.; Da Silva, J. L. F. Density Functional Investigation of the Adsorption Effects of Ph3 and Sh2 on the Structure Stability of the Au55 and Pt55 Nanoclusters. *J. Chem. Phys.* **2017**, *146*, 164304.
(210) Chan, C. H.; Poignant, F.; Beuve, M.; Dumont, E.; Loffreda, D. A Water Solvation Shell Can Transform Gold Metastable Nanoparticles in the Fluxional Regime. *J. Phys. Chem. Lett.* **2019**, *10*, 1092−1098.
(211) Suleiman, I. A.; Radny, M. W.; Gladys, M. J.; Smith, P. V.; Mackie, J. C.; Kennedy, E. M.; Dlugogorski, B. Z. Chlorination of the Cu(110) Surface and Copper Nanoparticles: A Density Functional Theory Study. *J. Phys. Chem. C* **2011**, *115*, 13412−13419.
(212) Chen, Z.; Balankura, T.; Fichthorn, K. A.; Rioux, R. M. Revisiting the Polyol Synthesis of Silver Nanostructures: Role of Chloride in Nanocube Formation. *ACS Nano* **2019**, *13*, 1849−1860.
(213) Fichthorn, K. A.; Chen, Z. H. Surface Science of Shape-Selective Metal Nanocrystal Synthesis from First-Principles: Growth

https://doi.org/10.1021/acs.chemrev.2c00831
Chem. Rev. XXXX, XXX, XXX−XXX

of Cu Nanowires and Nanocubes. *J. Vac. Sci.Technol. A* **2020**, *38*, 023210.
(214) Fichthorn, K. A.; Chen, Z.; Chen, Z.; Rioux, R. M.; Kim, M. J.; Wiley, B. J. Understanding the Solution-Phase Growth of Cu and Ag Nanowires and Nanocubes from First Principles. *Langmuir* **2021**, *37*, 4419−4431.
(215) Liu, S. H.; Balankura, T.; Fichthorn, K. A. Self-Assembled Monolayer Structures of Hexadecylamine on Cu Surfaces: Density-Functional Theory. *Phys. Chem. Chem. Phys.* **2016**, *18*, 32753−32761.
(216) Löfgren, J.; Rahm, J. M.; Brorsson, J.; Erhart, P. Computational Assessment of the Efficacy of Halides as Shape-Directing Agents in Nanoparticle Growth. *Phys. Rev. Mater.* **2020**, *4*, 096001.
(217) Yoo, S. H.; Lee, J. H.; Delley, B.; Soon, A. Why Does Bromine Square Palladium Off? An Ab Initio Study of Brominated Palladium and Its Nanomorphology. *Phys. Chem. Chem. Phys.* **2014**, *16*, 18570−18577.
(218) Wulff, G. Zur Frage Der Geschwindigkeit Des Wachsthums Und Der Auflösung Der Krystallflächen. *Z. fur Krist. - Cryst. Mater.* **1901**, *34*, 449−530.
(219) Laue, M. V. Der Wulffsche Satz Für Die Gleichgewichtsform Von Kristallen. *Z. fur Krist. - Cryst. Mater.* **1943**, *105*, 124−133.
(220) Markov, I. V. *Crystal Growth for Beginners: Fundamentals of Nucleation, Crystal Growth and Epitaxy*; World Scientific, 2016.
(221) Pimpinelli, A.; Villain, J. *Physics of Crystal Growth*; Cambridge University Press; 1998.
(222) Barnard, A. S. A Thermodynamic Model for the Shape and Stability of Twinned Nanostructures. *J. Phys. Chem. B* **2006**, *110*, 24498−24504.
(223) Reuter, K.; Scheffler, M. Composition, Structure, and Stability of Ruo2(110) as a Function of Oxygen Pressure. *Phys. Rev. B* **2001**, *65*, 035406.
(224) Reuter, K.; Scheffler, M. First-Principles Atomistic Thermodynamics for Oxidation Catalysis: Surface Phase Diagrams and Catalytically Interesting Regions. *Phys. Rev. Lett.* **2003**, *90*, No. 046103.
(225) Kilin, D. S.; Prezhdo, O. V.; Xia, Y. Shape-Controlled Synthesis of Silver Nanoparticles: Ab Initio Study of Preferential Surface Coordination with Citric Acid. *Chem. Phys. Lett.* **2008**, *458*, 113−116.
(226) Liu, S. H.; Saidi, W. A.; Zhou, Y.; Fichthorn, K. A. Synthesis of {111}-Faceted Au Nanocrystals Mediated by Polyvinylpyrrolidone: Insights from Density-Functional Theory and Molecular Dynamics. *J. Phys. Chem. C* **2015**, *119*, 11982−11990.
(227) Saidi, W. A.; Feng, H. J.; Fichthorn, K. A. Binding of Polyvinylpyrrolidone to Ag Surfaces: Insight into a Structure-Directing Agent from Dispersion-Corrected Density Functional Theory. *J. Phys. Chem. C* **2013**, *117*, 1163−1171.
(228) Zhou, Y.; Saidi, W. A.; Fichthorn, K. A. Comparison of the Binding of Polyvinylpyrrolidone and Polyethylene Oxide to Ag Surfaces: Elements of a Successful Structure-Directing Agent. *J. Phys. Chem. C* **2013**, *117*, 11444−11448.
(229) Ye, J. Y.; Attard, G. A.; Brew, A.; Zhou, Z. Y.; Sun, S. G.; Morgan, D. J.; Willock, D. J. Explicit Detection of the Mechanism of Platinum Nanoparticle Shape Control by Polyvinylpyrrolidone. *J. Phys. Chem. C* **2016**, *120*, 7532−7542.
(230) Chen, Z.; Fichthorn, K. A. Adsorption of Ethylenediamine on Cu Surfaces: Attributes of a Successful Capping Molecule Using First-Principles Calculations. *Nanoscale* **2021**, *13*, 13529−13537.
(231) Chen, Z.; Fichthorn, K. A. Adsorption of Alkylamines on Cu Surfaces: Identifying Ideal Capping Molecules Using First-Principles Calculations. *Nanoscale* **2021**, *13*, 18536−18545.
(232) Al-Saidi, W. A.; Feng, H.; Fichthorn, K. A. Adsorption of Polyvinylpyrrolidone on Ag Surfaces: Insight into a Structure-Directing Agent. *Nano Lett.* **2012**, *12*, 997−1001.
(233) Chiu, C. Y.; Wu, H.; Yao, Z.; Zhou, F.; Zhang, H.; Ozolins, V.; Huang, Y. Facet-Selective Adsorption on Noble Metal Crystals Guided by Electrostatic Potential Surfaces of Aromatic Molecules. *J. Am. Chem. Soc.* **2013**, *135*, 15489−15500.
(234) Ringe, S.; Hormann, N. G.; Oberhofer, H.; Reuter, K. Implicit Solvation Methods for Catalysis at Electrified Interfaces. *Chem. Rev.* **2022**, *122*, 10777−10820.
(235) Qi, X.; Zhou, Y.; Fichthorn, K. A. Obtaining the Solid-Liquid Interfacial Free Energy Via Multi-Scheme Thermodynamic Integration: Ag-Ethylene Glycol Interfaces. *J. Chem. Phys.* **2016**, *145*, 194108.
(236) Broughton, J. Q.; Gilmer, G. H. Molecular Dynamics Investigation of the Crystal−Fluid Interface. Vi. Excess Surface Free Energies of Crystal−Liquid Systems. *J. Chem. Phys.* **1986**, *84*, 5759−5768.
(237) Davidchack, R. L.; Laird, B. B. Direct Calculation of the Crystal−Melt Interfacial Free Energies for Continuous Potentials: Application to the Lennard-Jones System. *J. Chem. Phys.* **2003**, *118*, 7651.
(238) Laird, B. B.; Davidchack, R. L. Direct Calculation of the Crystal-Melt Interfacial Free Energy Via Molecular Dynamics Computer Simulation. *J. Phys. Chem. B* **2005**, *109*, 17802−17812.
(239) Leroy, F.; Dos Santos, D. J.; Muller-Plathe, F. Interfacial Excess Free Energies of Solid-Liquid Interfaces by Molecular Dynamics Simulation and Thermodynamic Integration. *Macromol. Rapid Commun.* **2009**, *30*, 864−870.
(240) Leroy, F.; Muller-Plathe, F. Solid-Liquid Surface Free Energy of Lennard-Jones Liquid on Smooth and Rough Surfaces Computed by Molecular Dynamics Using the Phantom-Wall Method. *J. Chem. Phys.* **2010**, *133*, No. 044110.
(241) Liu, J.; Davidchack, R. L.; Dong, H. B. Molecular Dynamics Calculation of Solid-Liquid Interfacial Free Energy and Its Anisotropy During Iron Solidification. *Comput. Mater. Sci.* **2013**, *74*, 92−100.
(242) Benjamin, R.; Horbach, J. Crystal-Liquid Interfacial Free Energy Via Thermodynamic Integration. *J. Chem. Phys.* **2014**, *141*, No. 044715.
(243) Espinosa, J. R.; Vega, C.; Sanz, E. The Mold Integration Method for the Calculation of the Crystal-Fluid Interfacial Free Energy from Simulations. *J. Chem. Phys.* **2014**, *141*, 134709.
(244) Qi, X.; Fichthorn, K. A. Theory of the Thermodynamic Influence of Solution-Phase Additives in Shape-Controlled Nanocrystal Synthesis. *Nanoscale* **2017**, *9*, 15635−15642.
(245) Vorobyov, I.; Anisimov, V. M.; Greene, S.; Venable, R. M.; Moser, A.; Pastor, R. W.; MacKerell, A. D. Additive and Classical Drude Polarizable Force Fields for Linear and Cyclic Ethers. *J. Chem. Theory Comput.* **2007**, *3*, 1120−1133.
(246) Guvench, O.; Greene, S. N.; Kamath, G.; Brady, J. W.; Venable, R. M.; Pastor, R. W.; Mackerell, A. D., Jr. Additive Empirical Force Field for Hexopyranose Monosaccharides. *J. Comput. Chem.* **2008**, *29*, 2543−2564.
(247) Lee, H.; Venable, R. M.; Mackerell, A. D., Jr.; Pastor, R. W. Molecular Dynamics Studies of Polyethylene Oxide and Polyethylene Glycol: Hydrodynamic Radius and Shape Anisotropy. *Biophys. J.* **2008**, *95*, 1590−1599.
(248) Vanommeslaeghe, K.; Hatcher, E.; Acharya, C.; Kundu, S.; Zhong, S.; Shim, J.; Darian, E.; Guvench, O.; Lopes, P.; Vorobyov, I.; Mackerell, A. D. Charmm General Force Field: A Force Field for Drug-Like Molecules Compatible with the Charmm All-Atom Additive Biological Force Fields. *J. Comput. Chem.* **2009**, *31*, 671−690.
(249) Williams, P. L.; Mishin, Y.; Hamilton, J. C. An Embedded-Atom Potential for the Cu-Ag System. *Modell. Simul. Mater. Sci. Eng.* **2006**, *14*, 817−833.
(250) Zhou, Y.; Saidi, W. A.; Fichthorn, K. A. A Force Field for Describing the Polyvinylpyrrolidone-Mediated Solution-Phase Synthesis of Shape-Selective Ag Nanoparticles. *J. Phys. Chem. C* **2014**, *118*, 3366−3374.
(251) Sun, Y. G.; Xia, Y. N. Large-Scale Synthesis of Uniform Silver Nanowires through a Soft, Self-Seeding. *Polyol Process. Adv. Mater.* **2002**, *14*, 833−837.
(252) Sun, Y. G.; Xia, Y. N. Shape-Controlled Synthesis of Gold and Silver Nanoparticles. *Science* **2002**, *298*, 2176−2179.

https://doi.org/10.1021/acs.chemrev.2c00831
Chem. Rev. XXXX, XXX, XXX−XXX

(253) Sun, Y.; Mayers, B.; Herricks, T.; Xia, Y. Polyol Synthesis of Uniform Silver Nanowires: A Plausible Growth Mechanism and the Supporting Evidence. *Nano Lett.* **2003**, *3*, 955−960.
(254) Wiley, B.; Sun, Y.; Mayers, B.; Xia, Y. Shape-Controlled Synthesis of Metal Nanostructures: The Case of Silver. *Chem.—Eur. J.* **2005**, *11*, 454−463.
(255) Chen, Z.; Chang, J. W.; Balasanthiran, C.; Milner, S. T.; Rioux, R. M. Anisotropic Growth of Silver Nanoparticles Is Kinetically Controlled by Polyvinylpyrrolidone Binding. *J. Am. Chem. Soc.* **2019**, *141*, 4328−4337.
(256) Wang, Y.; Peng, H. C.; Liu, J.; Huang, C. Z.; Xia, Y. Use of Reduction Rate as a Quantitative Knob for Controlling the Twin Structure and Shape of Palladium Nanocrystals. *Nano Lett.* **2015**, *15*, 1445−1450.
(257) Wales, D. J.; Munro, L. J. Changes of Morphology and Capping of Model Transition Metal Clusters. *J. Phys. Chem.* **1996**, *100*, 2053−2061.
(258) Sutton, A. P.; Chen, J. Long-Range Finnis−Sinclair Potentials. *Philos. Mag. Lett.* **1990**, *61*, 139−146.
(259) Murrell, J. N.; Mottram, R. E. Potential Energy Functions for Atomic Solids. *Mol. Phys.* **1990**, *69*, 571−585.
(260) Lipscomb, W. N. Framework Rearrangement in Boranes and Carboranes. *Science* **1966**, *153*, 373−378.
(261) Lan, Y. K.; Su, C. H.; Sun, W. H.; Su, A. C. Nucleation of Decahedral Ag Nanocrystals. *RSC Adv.* **2014**, *4*, 13768−13773.
(262) Tal, A. A.; Munger, E. P.; Abrikosov, I. A. Morphology Transition Mechanism from Icosahedral to Decahedral Phase During Growth of Cu Nanoclusters. *Phys. Rev. B* **2015**, *92*, 020102.
(263) Pavan, L.; Rossi, K.; Baletto, F. Metallic Nanoparticles Meet Metadynamics. *J. Chem. Phys.* **2015**, *143*, 184304.
(264) Rossi, K.; Pavan, L.; Soon, Y.; Baletto, F. The Effect of Size and Composition on Structural Transitions in Monometallic Nanoparticles. *Eur. Phys. J. B* **2018**, *91*, 33.
(265) Zhang, Z.; Hu, W.; Xiao, S. Melting, Melting Competition, and Structural Transitions between Shell-Closed Icosahedral and Octahedral Nickel Nanoclusters. *Phys. Rev. B* **2006**, *73*, 125443.
(266) Cheng, B.; Ngan, A. H. Thermally Induced Solid-Solid Structural Transition of Copper Nanoparticles through Direct Geometrical Conversion. *J. Chem. Phys.* **2013**, *138*, 164314.
(267) Laio, A.; Gervasio, F. L. Metadynamics: A Method to Simulate Rare Events and Reconstruct the Free Energy in Biophysics, Chemistry and Material Science. *Rep. Prog. Phys.* **2008**, *71*, 126601.
(268) Kastner, J.; Thiel, W. Bridging the Gap between Thermodynamic Integration and Umbrella Sampling Provides a Novel Analysis Method: "Umbrella Integration". *J. Chem. Phys.* **2005**, *123*, 144104.
(269) Perez, D.; Cubuk, E. D.; Waterland, A.; Kaxiras, E.; Voter, A. F. Long-Time Dynamics through Parallel Trajectory Splicing. *J. Chem. Theory Comput.* **2016**, *12*, 18−28.
(270) Voter, A. F. Parallel Replica Method for Dynamics of Infrequent Events. *Phys. Rev. B* **1998**, *57*, 13985.
(271) Mishin, Y.; Mehl, M. J.; Papaconstantopoulos, D. A.; Voter, A. F.; Kress, J. D. Structural Stability and Lattice Defects in Copper: Ab Initio, Tight-Binding, and Embedded-Atom Calculations. *Phys. Rev. B* **2001**, *63*, 224106.
(272) Grochola, G.; Russo, S. P.; Snook, I. K. On Fitting a Gold Embedded Atom Method Potential Using the Force Matching Method. *J. Chem. Phys.* **2005**, *123*, 204719.
(273) Huang, R.; Wen, Y. H.; Voter, A. F.; Perez, D. Direct Observations of Shape Fluctuation in Long-Time Atomistic Simulations of Metallic Nanoclusters. *Phys. Rev. Mater.* **2018**, *2*, 126002.
(274) Baletto, F.; Mottet, C.; Ferrando, R. Reentrant Morphology Transition in the Growth of Free Silver Nanoclusters. *Phys. Rev. Lett.* **2000**, *84*, 5544−5547.
(275) Baletto, F.; Mottet, C.; Ferrando, R. Molecular Dynamics Simulations of Surface Diffusion and Growth on Silver and Gold Clusters. *Surf. Sci.* **2000**, *446*, 31−45.
(276) Konuk, M.; Durukanoglu, S. Shape-Controlled Growth of Metal Nanoparticles: An Atomistic View. *Phys. Chem. Chem. Phys.* **2016**, *18*, 1876−1885.
(277) Barron, H.; Opletal, G.; Tilley, R.; Barnard, A. S. Predicting the Role of Seed Morphology in the Evolution of Anisotropic Nanocatalysts. *Nanoscale* **2017**, *9*, 1502−1510.
(278) Xia, Y.; Nelli, D.; Ferrando, R.; Yuan, J.; Li, Z. Y. Shape Control of Size-Selected Naked Platinum Nanocrystals. *Nat. Commun.* **2021**, *12*, 3019.
(279) Hall, B. D.; Flüeli, M.; Monot, R.; Borel, J.-P. Multiply Twinned Structures in Unsupported Ultrafine Silver Particles Observed by Electron Diffraction. *Phys. Rev. B* **1991**, *43*, 3906−3917.
(280) Reinhard, D.; Hall, B. D.; Ugarte, D.; Monot, R. Size-Independent Fcc-to-Icosahedral Structural Transition in Unsupported Silver Clusters: An Electron Diffraction Study of Clusters Produced by Inert-Gas Aggregation. *Phys. Rev. B* **1997**, *55*, 7868−7881.
(281) Reinhard, D.; Hall, B. D.; Berthoud, P.; Valkealahti, S.; Monot, R. Size-Dependent Icosahedral-to-Fcc Structure Change Confirmed in Unsupported Nanometer-Sized Copper Clusters. *Phys. Rev. Lett.* **1997**, *79*, 1459−1462.
(282) Grochola, G.; Snook, I. K.; Russo, S. P. Computational Modeling of Nanorod Growth. *J. Chem. Phys.* **2007**, *127*, 194707.
(283) Meena, S. K.; Sulpizi, M. From Gold Nanoseeds to Nanorods: The Microscopic Origin of the Anisotropic Growth. *Angew. Chem., Int. Ed. Engl.* **2016**, *55*, 11960−11964.
(284) Meena, S. K.; Sulpizi, M. Understanding the Microscopic Origin of Gold Nanoparticle Anisotropic Growth from Molecular Dynamics Simulations. *Langmuir* **2013**, *29*, 14954−14961.
(285) Meena, S. K.; Celiksoy, S.; Schafer, P.; Henkel, A.; Sonnichsen, C.; Sulpizi, M. The Role of Halide Ions in the Anisotropic Growth of Gold Nanoparticles: A Microscopic, Atomistic Perspective. *Phys. Chem. Chem. Phys.* **2016**, *18*, 13246−13254.
(286) Fichthorn, K. A.; Weinberg, W. H. Theoretical Foundations of Dynamical Monte Carlo Simulations. *J. Chem. Phys.* **1991**, *95*, 1090−1096.
(287) Turner, C. H.; Lei, Y.; Bao, Y. Modeling the Atomistic Growth Behavior of Gold Nanoparticles in Solution. *Nanoscale* **2016**, *8*, 9354−9365.
(288) He, X.; Cheng, F.; Chen, Z.-X. The Lattice Kinetic Monte Carlo Simulation of Atomic Diffusion and Structural Transition for Gold. *Sci. Rep.* **2016**, *6*, 33128.
(289) Li, X. Y.; Zhu, B.; Qi, R.; Gao, Y. Real-Time Simulation of Nonequilibrium Nanocrystal Transformations. *Adv. Theory Simul.* **2019**, *2*, 1800127.
(290) Galanakis, I.; Bihlmayer, G.; Bellini, V.; Papanikolaou, N.; Zeller, R.; Blugel, S.; Dederichs, P. H. Broken-Bond Rule for the Surface Energies of Noble Metals. *Europhys. Lett.* **2002**, *58*, 751−757.
(291) Lai, K. C.; Evans, J. W. Reshaping and Sintering of 3d Fcc Metal Nanoclusters: Stochastic Atomistic Modeling with Realistic Surface Diffusion Kinetics. *Phys. Rev. Mater.* **2019**, *3*, 026001.
(292) Lai, K. C.; Chen, M.; Williams, B.; Han, Y.; Tsung, C. K.; Huang, W.; Evans, J. W. Reshaping of Truncated Pd Nanocubes: Energetic and Kinetic Analysis Integrating Transmission Electron Microscopy with Atomistic-Level and Coarse-Grained Modeling. *ACS Nano* **2020**, *14*, 8551−8561.
(293) Fichthorn, K. A.; Weinberg, W. H. Influence of Time-Dependent Rates of Mass Transfer on the Kinetics of Domain Growth. *Phys. Rev. Lett.* **1992**, *68*, 604−607.
(294) Fichthorn, K. A.; Scheffler, M. Island Nucleation in Thin-Film Epitaxy: A First-Principles Investigation. *Phys. Rev. Lett.* **2000**, *84*, 5371−5374.
(295) Vineyard, G. H. Frequency Factors and Isotope Effects in Solid State Rate Processes. *J. Phys. Chem. Solids* **1957**, *3*, 121−127.
(296) Hauwiller, M. R.; Frechette, L. B.; Jones, M. R.; Ondry, J. C.; Rotskoff, G. M.; Geissler, P.; Alivisatos, A. P. Unraveling Kinetically-Driven Mechanisms of Gold Nanocrystal Shape Transformations Using Graphene Liquid Cell Electron Microscopy. *Nano Lett.* **2018**, *18*, 5731−5737.

https://doi.org/10.1021/acs.chemrev.2c00831
Chem. Rev. XXXX, XXX, XXX−XXX

(297) Chernov, A. A. The Kinetics of the Growth Forms of Crystals. *Sov. Phys. Crystallogr.* **1963**, *7*, 728.
(298) Gadewar, S. B.; Hofmann, H. M.; Doherty, M. F. Evolution of Crystal Shape. *Cryst. Growth Des.* **2004**, *4*, 109−112.
(299) Fichthorn, K. A.; Balankura, T.; Qi, X. Multi-Scale Theory and Simulation of Shape-Selective Nanocrystal Growth. *CrystEngComm* **2016**, *18*, 5410−5417.
(300) Qi, X.; Balankura, T.; Zhou, Y.; Fichthorn, K. A. How Structure-Directing Agents Control Nanocrystal Shape: Polyvinylpyrrolidone-Mediated Growth of Ag Nanocubes. *Nano Lett.* **2015**, *15*, 7711−7717.
(301) Balankura, T.; Qi, X.; Zhou, Y.; Fichthorn, K. A. Predicting Kinetic Nanocrystal Shapes through Multi-Scale Theory and Simulation: Polyvinylpyrrolidone-Mediated Growth of Ag Nanocrystals. *J. Chem. Phys.* **2016**, *145*, 144106.
(302) Torrie, G. M.; Valleau, J. P. Nonphysical Sampling Distributions in Monte Carlo Free-Energy Estimation: Umbrella Sampling. *J. Comput. Phys.* **1977**, *23*, 187−199.
(303) Hänggi, P.; Talkner, P.; Borkovec, M. Reaction-Rate Theory: Fifty Years after Kramers. *Rev. Mod. Phys.* **1990**, *62*, 251−341.
(304) Woolf, T. B.; Roux, B. Conformational Flexibility of O-Phosphorylcholine and O-Phosphorylethanolamine - a Molecular-Dynamics Study of Solvation Effects. *J. Am. Chem. Soc.* **1994**, *116*, 5916−5926.
(305) Hummer, G. Position-Dependent Diffusion Coefficients and Free Energies from Bayesian Analysis of Equilibrium and Replica Molecular Dynamics Simulations. *New J. Phys.* **2005**, *7*, 34.
(306) Xia, X.; Zeng, J.; Oetjen, L. K.; Li, Q.; Xia, Y. Quantitative Analysis of the Role Played by Poly(Vinylpyrrolidone) in Seed-Mediated Growth of Ag Nanocrystals. *J. Am. Chem. Soc.* **2012**, *134*, 1793−1801.
(307) Xia, X.; Zeng, J.; Zhang, Q.; Moran, C. H.; Xia, Y. Recent Developments in Shape-Controlled Synthesis of Silver Nanocrystals. *J. Phys. Chem. C* **2012**, *116*, 21647−21656.
(308) Qi, X.; Chen, Z.; Yan, T.; Fichthorn, K. A. Growth Mechanism of Five-Fold Twinned Ag Nanowires from Multiscale Theory and Simulations. *ACS Nano* **2019**, *13*, 4647−4656.
(309) Kim, J.; Cui, J.; Fichthorn, K. A. Solution-Phase Growth of Cu Nanowires with Aspect Ratios Greater Than 1000: Multiscale Theory. *ACS Nano* **2021**, *15*, 18279−18288.
(310) Kim, J.; Fichthorn, K. A. The Influence of Iodide on the Solution-Phase Growth of Cu Microplates: A Multi-Scale Theoretical Analysis from First Principles. *Faraday Discuss.* **2022**, *235*, 273−288.
(311) Mastronardi, V.; Kim, J.; Veronesi, M.; Pomili, T.; Berti, F.; Udayan, G.; Brescia, R.; Diercks, J. S.; Herranz, J.; Bandiera, T.; et al. Green Chemistry and First-Principles Theory Enhance Catalysis: Synthesis and 6-Fold Catalytic Activity Increase of Sub-5 Nm Pd and Pt@Pd Nanocubes. *Nanoscale* **2022**, *14*, 10155−10168.
(312) Kemeny, J. G.; Snell, J. L. *Finite Markov Chains*; Van Nostrand, 1976.
(313) Iosifescu, M. *Finite Markov Processes and Their Applications*; Dover Publications, 1980.
(314) Novotny, M. A. Monte Carlo Algorithms with Absorbing Markov Chains: Fast Local Algorithms for Slow Dynamics. *Phys. Rev. Lett.* **1995**, *74*, 1−5.
(315) Fichthorn, K. A.; Lin, Y. A Local Superbasin Kinetic Monte Carlo Method. *J. Chem. Phys.* **2013**, *138*, 164104.
(316) da Silva, R. R.; Yang, M.; Choi, S. I.; Chi, M.; Luo, M.; Zhang, C.; Li, Z. Y.; Camargo, P. H.; Ribeiro, S. J.; Xia, Y. Facile Synthesis of Sub-20 Nm Silver Nanowires through a Bromide-Mediated Polyol Method. *ACS Nano* **2016**, *10*, 7892−7900.
(317) Tan, T.; Zhang, S.; Wang, J.; Zheng, Y.; Lai, H.; Liu, J.; Qin, F.; Wang, C. Resolving the Stacking Fault Structure of Silver Nanoplates. *Nanoscale* **2021**, *13*, 195−205.
(318) Germain, V.; Li, J.; Ingert, D.; Wang, Z. L.; Pileni, M. P. Stacking Faults in Formation of Silver Nanodisks. *J. Phys. Chem. B* **2003**, *107*, 8717−8720.
(319) Elechiguerra, J. L.; Reyes-Gasga, J.; Yacaman, M. J. The Role of Twinning in Shape Evolution of Anisotropic Noble Metal Nanostructures. *J. Mater. Chem.* **2006**, *16*, 3906−3919.
(320) Liao, H. G.; Zherebetskyy, D.; Xin, H.; Czarnik, C.; Ercius, P.; Elmlund, H.; Pan, M.; Wang, L. W.; Zheng, H. Nanoparticle Growth. Facet Development During Platinum Nanocube Growth. *Science* **2014**, *345*, 916−919.
(321) Kim, M. J.; Alvarez, S.; Chen, Z.; Fichthorn, K. A.; Wiley, B. J. Single-Crystal Electrochemistry Reveals Why Metal Nanowires Grow. *J. Am. Chem. Soc.* **2018**, *140*, 14740−14746.
(322) Jin, M.; He, G.; Zhang, H.; Zeng, J.; Xie, Z.; Xia, Y. Shape-Controlled Synthesis of Copper Nanocrystals in an Aqueous Solution with Glucose as a Reducing Agent and Hexadecylamine as a Capping Agent. *Angew. Chem., Int. Ed. Engl.* **2011**, *50*, 10560−10564.
(323) Kim, M. J.; Alvarez, S.; Yan, T. Y.; Tadepalli, V.; Fichthorn, K. A.; Wiley, B. J. Modulating the Growth Rate, Aspect Ratio, and Yield of Copper Nanowires with Alkylamines. *Chem. Mater.* **2018**, *30*, 2809−2818.
(324) Luo, M.; Ruditskiy, A.; Peng, H. C.; Tao, J.; Figueroa-Cosme, L.; He, Z. K.; Xia, Y. N. Penta-Twinned Copper Nanorods: Facile Synthesis Via Seed-Mediated Growth and Their Tunable Plasmonic Properties. *Adv. Funct. Mater.* **2016**, *26*, 1209−1216.
(325) Wang, Y.; Chen, A. A.; Balto, K. P.; Xie, Y.; Figueroa, J. S.; Pascal, T. A.; Tao, A. R. Curvature-Selective Nanocrystal Surface Ligation Using Sterically-Encumbered Metal-Coordinating Ligands. *ACS Nano* **2022**, *16*, 12747−12754.
(326) Zeni, C.; Rossi, K.; Glielmo, A.; Baletto, F. On Machine Learning Force Fields for Metallic Nanoparticles. *Adv. Phys X* **2019**, *4*, 1654919.
(327) Ouyang, R.; Xie, Y.; Jiang, D. E. Global Minimization of Gold Clusters by Combining Neural Network Potentials and the Basin-Hopping Method. *Nanoscale* **2015**, *7*, 14817−14821.
(328) Zhang, Y. K.; Yang, W. T. Comment on "Generalized Gradient Approximation Made Simple". *Phys. Rev. Lett.* **1998**, *80*, 890−890.
(329) Fernandez, M.; Barnard, A. S. Identification of Nanoparticle Prototypes and Archetypes. *ACS Nano* **2015**, *9*, 11980−11992.
(330) Zhang, H.; Barnard, A. S. Impact of Atomistic or Crystallographic Descriptors for Classification of Gold Nanoparticles. *Nanoscale* **2021**, *13*, 11887−11898.
(331) Parker, A. J.; Motevalli, B.; Opletal, G.; Barnard, A. S. The Pure and Representative Types of Disordered Platinum Nanoparticles from Machine Learning. *Nanotechnology* **2021**, *32*, No. 095404.
(332) Parker, A. J.; Barnard, A. S. Selecting Appropriate Clustering Methods for Materials Science Applications of Machine Learning. *Adv. Theory Simul.* **2019**, *2*, 1900145.
(333) Parker, A. J.; Opletal, G.; Barnard, A. S. Classification of Platinum Nanoparticle Catalysts Using Machine Learning. *J. Appl. Phys.* **2020**, *128*, No. 014301.
(334) Voter, A. F. Hyperdynamics: Accelerated Molecular Dynamics of Infrequent Events. *Phys. Rev. Lett.* **1997**, *78*, 3908−3911.
(335) Voter, A. F. A Method for Accelerating the Molecular Dynamics Simulation of Infrequent Events. *J. Chem. Phys.* **1997**, *106*, 4665−4677.
(336) Miron, R. A.; Fichthorn, K. A. Accelerated Molecular Dynamics with the Bond-Boost Method. *J. Chem. Phys.* **2003**, *119*, 6210−6216.
(337) Kim, S. Y.; Perez, D.; Voter, A. F. Local Hyperdynamics. *J. Chem. Phys.* **2013**, *139*, 144110.
(338) Plimpton, S. J.; Perez, D.; Voter, A. F. Parallel Algorithms for Hyperdynamics and Local Hyperdynamics. *J. Chem. Phys.* **2020**, *153*, No. 054116.
(339) Cui, J.; Fichthorn, K. A. Optiboost: A Method for Choosing a Safe and Efficient Boost for the Bond-Boost Method in Accelerated Molecular Dynamics Simulations with Hyperdynamics. *J. Chem. Phys.* **2022**, *156*, 204107.
(340) Puchala, B.; Falk, M. L.; Garikipati, K. An Energy Basin Finding Algorithm for Kinetic Monte Carlo Acceleration. *J. Chem. Phys.* **2010**, *132*, 134104.

https://doi.org/10.1021/acs.chemrev.2c00831
Chem. Rev. XXXX, XXX, XXX−XXX